# OBSERVATIONS OF SUPERNOVA REMNANTS AT VERY HIGH ENERGIES WITH VERITAS

by

Patrick Dean Wilcox

A thesis submitted in partial fulfillment
of the requirements for
the Doctor of Philosophy degree in Physics
in the Graduate College of

The University of Iowa

August 2019

Thesis Supervisor: Professor Philip E. Kaaret

For Delaney and Declan.

"In the beginning the Universe was created. This has made a lot of people very angry and been widely regarded as a bad move."

Douglas Adams, *The Restaurant at the End of the Universe*

## ACKNOWLEDGEMENTS

I am sincerely appreciative for the patience and support that Professor Phil Kaaret has given me throughout my graduate studies. My time at UI would have been dramatically different without your knowledge and experience to guide me. I am also very grateful for the consistently available financial support provided by you. Lastly, thank you for the encouragement and understanding that you provided throughout the years. Even when I lost track of time, you didn't, and kept me moving forward until the end.

I am grateful for the support of my thesis committee members: Prof. Cornelia Lang, Prof. Ken Gayley, Prof. Steve Spangler and Prof. John Finley. Thank you, in particular, to John for making the trip from West Lafayette for my defense! I am also grateful for the support from Prof. Bob Mutel and (again) Prof. Gayley for finding time to serve as my teaching practicum mentor. Thank you all for finding the time to provide guidance. Your perspectives have provided an immeasurable amount of assistance, and I will always carry your contributions with me.

I am also thankful for the support from many individuals within the VERITAS collaboration: Nahee, Reshmi, Brian, Ben, Ralph, Qi, Wystan, Michael, Gareth, and many others that I have missed. Thank you for supporting my growth as a VERITAS member. This work would not have been possible without your contributions. I also want to thank Evan, Dominic, Stephanie, Daniel, and my other peers at UI. Your discussions and distractions helped to keep me grounded.

Lastly, I am indebted to my family. Thank you to my parents, grandparents, and in-laws for being supportive. Particularly, I am grateful for the backing of my wife Elizabeth, daughter Delaney, and son Declan. Your love and encouragement proved more necessary than I will often admit. Thank you, and I love you.

## ABSTRACT

The constant flux of cosmic rays that bombard Earth from within our own galaxy are understood to come from both shell-type supernova remnants and pulsar wind nebulae (PWNe). Multiwavelength study of these objects can help us to understand what types of particles are accelerated, and gamma-ray emission is key to understanding the highest energy cosmic rays. In this thesis, I analyze and interpret observations made with the Very Energetic Radiation Imaging Telescope Array System (VERITAS), a gamma-ray telescope located in Southern Arizona.

LS 5039 and HESS J1825-137 occupy the same field of view on the sky and were observed for about 8 hours with VERITAS. LS 5039 is a gamma-ray binary, and the observations supports theories that the compact object hosts a PWN which is continuously interacting with the nearby star. HESS J1825-137 is a very extended PWN with an extent of diameter of $> 1^{\circ}$ on the sky. Using the VERITAS observations, I am able to measure the radial profile and compare the gamma-ray luminosity to other PWN.

DA 495, a "Crab-like" PWN with unusually strong magnetic fields, was observed for about 70 hours with VERITAS. In this study, results are combined with radio and X-ray spectral information to allow for detailed astrophysical modeling of the region. This broadband spectral modeling places constraints on the properties of the particle population in this PWN and allows for both leptonic and hadronic emission scenarios to be evaluated. Hadronic scenarios instil doubt on the pure PWN interpretation and favor a previously undetected shell-type remnant being present.

## PUBLIC ABSTRACT

Supernova occur when a star, with a mass several times of our sun, explodes. This event signifies the end of the star's life and the explosion sends particles and light into the surrounding region of space. Over tens of thousands of years the ejected material spreads out, creating a nebula visible to observers called a supernova remnant. In many cases, the central core of the star is crushed into a quickly spinning pulsar which illuminates its own nebula at the location of the dead star. The pulsar creates a disk-shaped wind and this central remnant is called a pulsar wind nebula.

The extreme nature of supernova remnants allows studies of physical systems that we cannot perform on Earth. Even long after the explosion, supernova remnants generate cosmic rays, which are particles bombarding Earth constantly and travel nearly at the speed of light. By studying the light that supernova remnants emit across the entire electromagnetic spectrum, we can gain understanding about the physical processes that accelerate cosmic rays to extreme velocities.

Using a ground-based gamma-ray telescope called the Very Energetic Radiation Imaging Telescope Array System (VERITAS) I observed several supernova remnants. Gamma-rays are the highest energy light and by comparing the light measured by VERITAS with other observatories, we can understand better the processes that accelerate energetic particles that fill our galaxy.

## TABLE OF CONTENTS

## LIST OF TABLES

## LIST OF FIGURES

# CHAPTER 1

# GAMMA-RAY ASTRONOMY

## 1.1 Introduction

The visible light that we perceive with our eyes is only a fraction of what traverses the universe. As such, in order to gain a complete picture of any particular celestial object, we must observe the light from across the electromagnetic spectrum. This may seem obvious to astronomers now, but non-visible light was not detected until infrared radiation was discovered by William Herschel in 1800 while experimenting with a way to detect sunspots. Over the next 110 years, pioneers in physics Heinrich Hertz and Ernest Rutherford probed the extremes of the electromagnetic spectrum, radio waves and gamma rays, and these phenomena were quickly identified as being fundamentally the same as visible light. Astronomers later harnessed this expansion of understanding and have been using this knowledge of the unified and broadband electromagnetic spectrum to look skyward and gain more information than possible with optical telescopes alone.

The classifications of various bands of light is mostly historical due to the initial detection usually being associated with a particular phenomena - like the gamma-rays ($\sim$ MeV photons) associated with photons emitted with nuclear decay. Before being merged into a single understanding, each waveband required a slightly different apparatus, and a different observational method, to detect that light. Modern astronomical observatories are still classified, necessarily, by their waveband because their (optimal) detection methods vary by wavelength. Most of these instruments are designed to focus light in a manner to maximize the signal

that is received by the appropriate detector. However, there is not currently a practical telescope to focus gamma-ray photons. Laue lenses to focus ∼MeV photons are just now being developed, and the implications for astronomical observatories are still being explored (Camattari, 2016).

Observations of gamma rays are done in space and on the ground with the space telescopes being more sensitive to gamma-rays in the MeV-GeV range and the ground-based telescopes being sensitive to very high energy (VHE) gamma rays in the TeV range. There are 5098 gamma-ray sources in the fourth catalog of sources detected by the Large Area Telescope on the *Fermi Gamma-ray Space Telescope* (*Fermi*-LAT) (The Fermi-LAT collaboration, 2019). However, there are only 223 VHE sources listed in TeVCat, a resource which compiles information on known TeV-emitting sources (Wakely and Horan, 2008) and the first VHE source, the Crab Nebula (Messier 1), was first detected in 1989 by the Whipple 10m Observatory (Weekes et al., 1989). Figure 1.1 shows the number of known TeV sources over time and the operating time frame of a few key ground-based TeV gamma ray observatories. Maps of the gamma-ray sky are shown in Figure 1.2.

With only a few hundred detected VHE sources it must follow that the phenomena that generates this emission must be equally rare.[1] VHE gamma-ray astronomy and astrophysics is of particular importance due to the unique association with acceleration of cosmic rays (see Section 1.2.1 and Chapter 3). Sources that are known to emit TeV gamma rays include: gamma-ray binaries - compact-objects interacting with a star, supernova remnants (SNR) - shockwaves from supernovae still propagating through the interstellar medium, pulsar wind nebulae (PWN) - fast-spinning neutron stars that are generating relativistic winds, and active-galactic nuclei (AGN) - powerful jets powered by supermassive black holes

[1]Just for comparison: the Gaia mission now has details on over 1.3 billion stars (Gaia Collaboration et al., 2018) - VHE sources are exceptionally rare indeed!

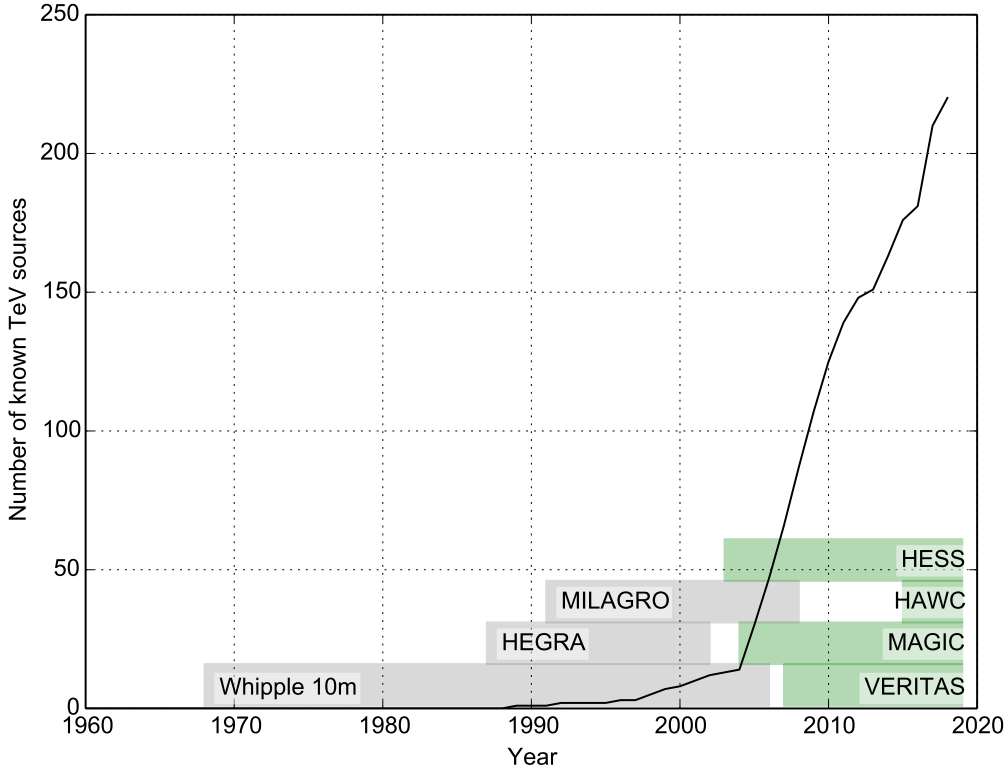


Figure 1.1 Number of known TeV sources versus time is plotted. The years when major ground-based TeV observatories were/are active is indicated. The gray boxes indicate former experiments, and the current experiments are in green. The data is from TeVCat (Wakely and Horan, 2008).

which push material far into the intergalactic medium. These are all thought to accelerate particles to very high energies, and the VHE gamma-ray emission is evidence of that.

## 1.2 Cosmic-ray Observations

In 1912, Victor Hess made the discovery that ambient radiation was more intense at higher altitudes and that it was caused by high energy particles impacting the atmosphere (he won the 1936 Nobel Prize for this work). He was also able to first prove the incoming particles' extra-terrestrial origin, and later he was able to prove

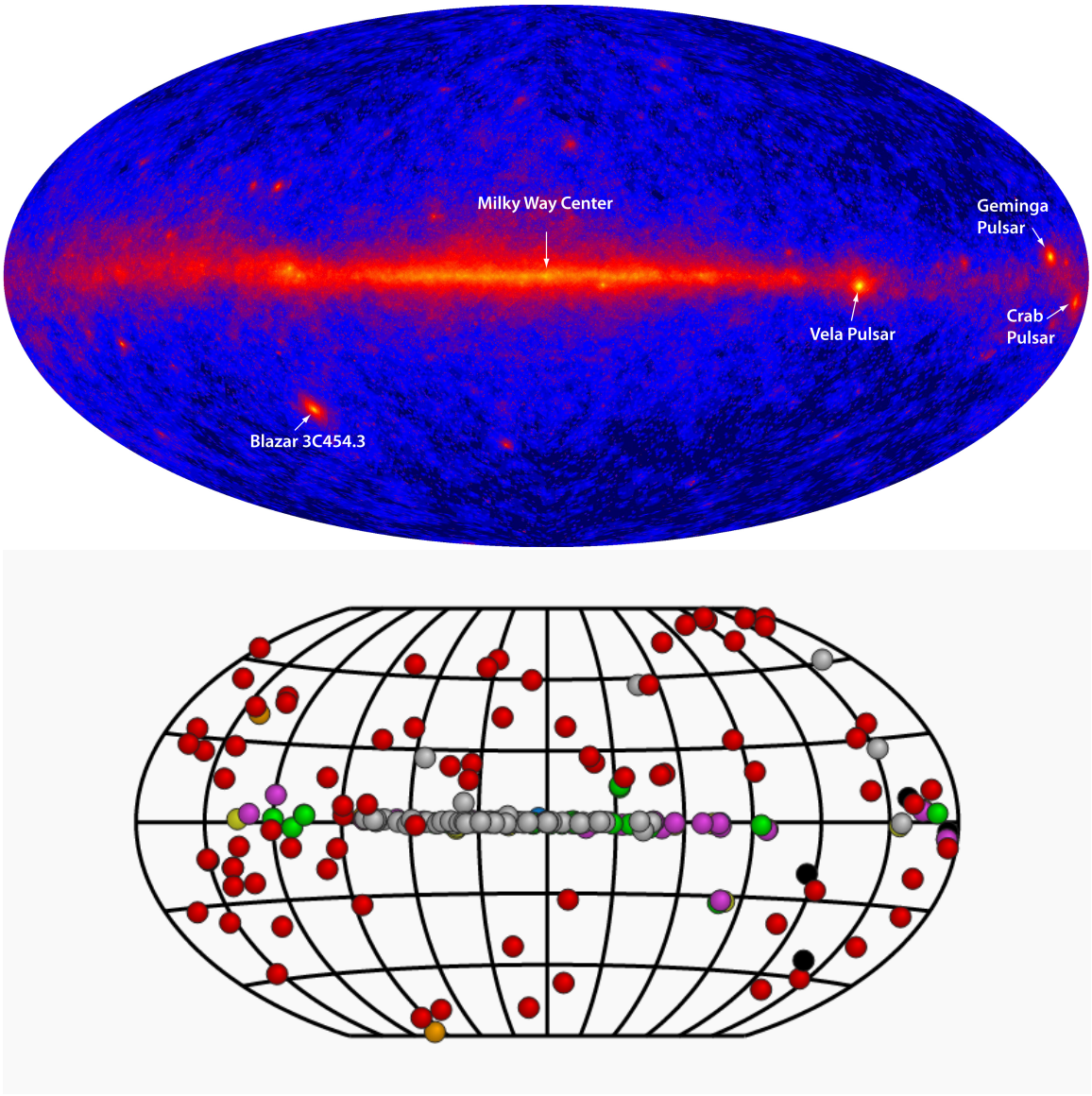


Figure 1.2 Top: An all sky image of the MeV-GeV gamma-ray sky by *Fermi* with some notable sources labeled. The galactic plane is clearly visible as a band across the middle. Image credit: NASA/DOE/International LAT Team, Bottom: VHE gamma-ray (TeV) sources from TeVCat (Wakely and Horan, 2008). Red and black dots are AGN, grey are unidentified sources, green are SNR, pink are PWN, yellow are binaries, and orange are super-bubbles.

their extra-solar origin (Hess, 1931). Astronomers have since been attempting to determine the source of these very high energy cosmic rays.

Modern measurements of the cosmic-ray spectrum are able to detect ultra high energy particles that reach up to 40 EeV. The spectrum that is detected of cosmic rays (shown in Figure 1.3) has a few features based on the acceleration mechanism and composition (Antoni et al., 2005). At the highest energies, the "Ankle" is a feature just above 1 EeV ($10^9$ GeV) where anisotropy strongly suggests that these cosmic rays are virtually all extra-galactic (Pierre Auger Collaboration et al., 2017; Aab et al., 2018). Below that energy, starting at around 1 PeV ($10^6$ GeV), is the "Knee" where supernova remnants become less efficient at accelerating particles (Hillas, 2005).

### 1.2.1 Astrophysical motivation: cosmic ray acceleration

Baade and Zwicky (1934) argued that the energy release from supernovae could easily account for the intensity of cosmic rays detected on Earth. A supernova, the explosion created by a massive star ($> 8\ M_\odot$) at the end of their life, sends a large amount of extremely energetic material into the interstellar medium and dissipating into the galaxy. For thousands of years after the explosion, a SNR continues to expand, radiate, and generate a shock front when it interacts with the local medium. Protons and other nuclei caught in the expanding shock experience first-order Fermi acceleration as they bounce back and forth across the shock and are thought to reach very high energies by this process. Only recently, in 2013, was it proven that this was in fact the case (Ackermann et al., 2013). Observations of SNRs W44 and IC443 by *Fermi*-LAT and others were used to show that relativistic protons were present.

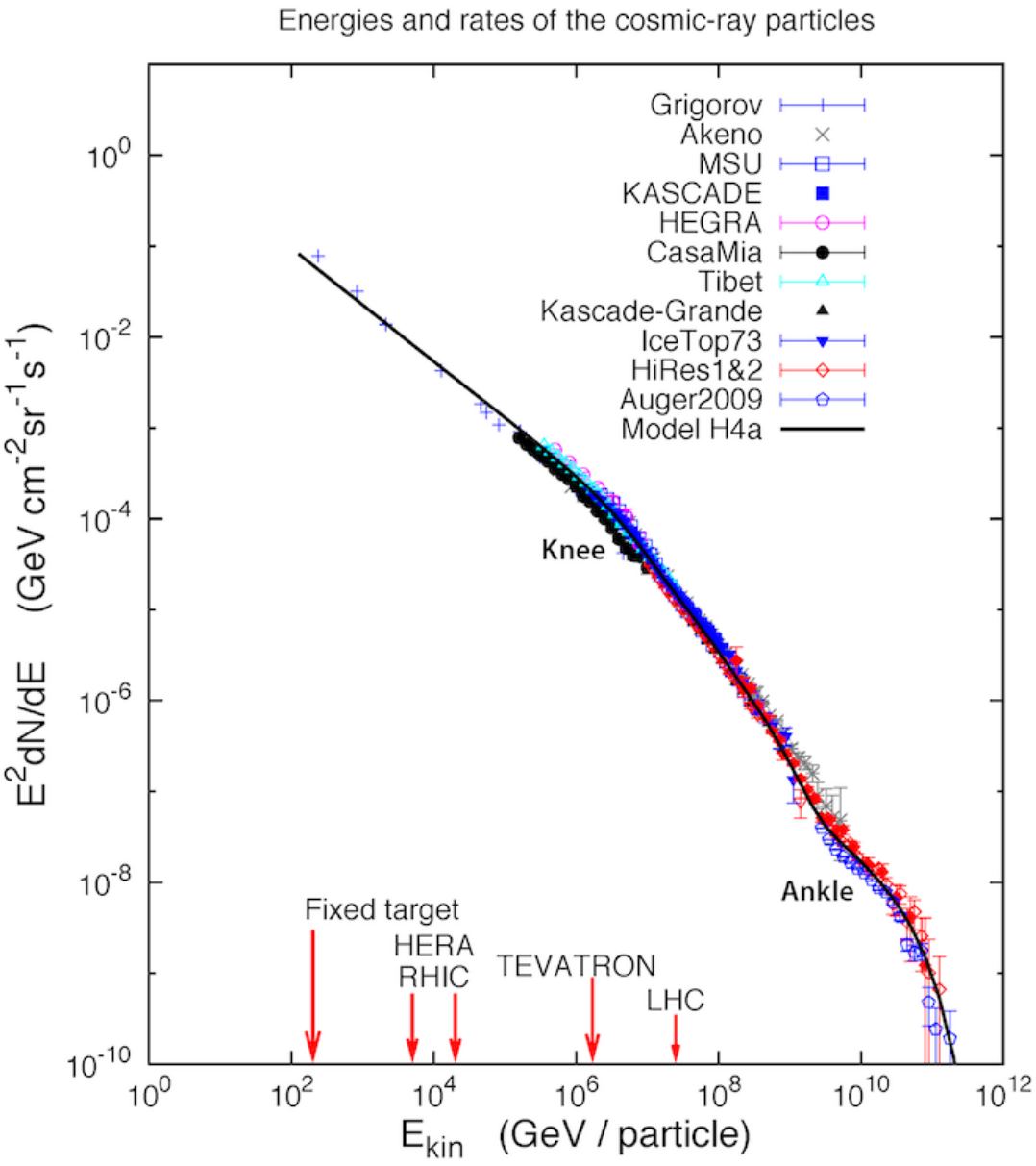


Figure 1.3 Cosmic-ray spectra from various observatories. Energies producible by terrestrial particle colliders are indicated at the bottom. Image credit: Icecube/IceTop

The origin of charged particles that are accelerated to relativistic energies become scrambled due to intervening magnetic fields. In contrast, gamma-ray astrophysics allows for the measurement of energies and densities of cosmic rays at the source, since the cosmic rays will often interact with material in or near their environment of origin. The interaction of a cosmic ray with the environment will create signature gamma-rays. Since photons do not noticeably deflect from their origin, these gamma rays can be used as a measuring stick for what is happening at the source.

The objects that produce cosmic rays are of special interest since they allow for the study of natural mechanisms which create some of the most energetic processes in the Milky Way. The natural mechanisms allow us to continue to test the supernova-origin theory of cosmic rays presented by Baade and Zwicky (1934).

### 1.2.2 Galactic sources of cosmic-rays

The gamma-ray emission from the shell of a SNR can be explained by $\pi^0$ decay. When very high energy nuclei interact with other nuclei, a $\pi^0$ can be created which rapidly decays into two 67.5 MeV photons that create a distinctive bump in the spectrum. The surrounding, cooler medium of a SNR gives a ready supply of slow nuclei for the escaping protons to interact with which feeds the decay chain. *Fermi*-LAT analysis (Ackermann et al., 2013) was able to compare the observed spectral energy distribution from 60 MeV to 200 GeV to models including a physically sensible proton energy distribution to demonstrate $\pi^0$-decay is present. Observing SNR at higher energies help to further constrain these models (VERITAS is sensitive above 100 GeV) and provide additional information regarding the cause of the *knee* in the cosmic-ray spectrum.

In addition, the *Fermi*-LAT analysis was limited to treating these SNRs as single point sources, so gamma-ray morphology is not available. The process leading to $\pi^0$ decay would only occur on the exterior of a remnant (as the outward shock interacts with cool medium), so an inability to resolve spatial details about the source begs the question: how does the emission differ interior of the SNR? The complication due to an unknown gamma-ray morphology is presented in another analysis of SNR IC443 (Abdo et al., 2010) and an analysis of SNR Cas-A (Acciari et al., 2010). For these objects there is still confusion about the emission mechanism based on the spectral energy distribution, alone, and part of the gamma-ray emission is thought to be caused by inverse-Compton scattering of electrons and not just $\pi^0$ decay.

Another source of galactic cosmic-rays, besides the shell-type SNR previously described, are pulsar wind nebulae (PWNe). When a massive star explodes in a core collapse supernova, much of its angular momentum remains with the newly created neutron star (pulsar). This pulsar can produce an expanding bubble of highly relativistic wind, called the pulsar wind nebula (PWN), and forms a termination shock. The observation of synchrotron and inverse Compton emission within the PWN suggest the acceleration of particles. The pulsar continues to feed the PWN with its rotational energy and expand the boundary of the nebula (Gaensler and Slane, 2006). Gamma-ray emission in these objects, which are more numerous than shell-type remnants at very high energies, is due to inverse-Compton scattering as the relativistic electrons boost photons to TeV energies in the strong shock at the termination of the pulsar wind (Atoyan and Aharonian, 1996).

Understanding the morphology of composite PWN/SNR help to isolate the emission as inverse-Compton emission would be mainly from the area interior to the shell, and the $\pi^0$-decay would occur only on the shell since it requires a cool

medium to interact with. DA 495, studied in Chapter 5, is currently thought to be a PWN, though this work will present evidence suggesting that the gamma-ray emission may come from hadronic emission similar to a SNR. Studying this object incorporates knowledge of PWN and SNR to test the understanding of each.

## 1.3 Thesis Overview

The goal of this thesis is to investigate the sources of cosmic rays from within our galaxy to demonstrate that the constant flux of cosmic rays detected on Earth, at least in part, come from shell-type supernova remnants (SNR) and pulsar wind nebulae (PWNe). Very high energy gamma rays emitted in the vicinity of supernova remnants indicate that particles are accelerated in that region since we cannot determine the origin of cosmic rays due to deflection by intervening magnetic fields.

Background about the detection of gamma rays, and the link to particle acceleration are found in the next chapters. Chapter 2 discusses gamma-ray observatories and the analysis required for VHE ground-based astronomy of the Very Energetic Radiation Imaging Telescope Array System (VERITAS), an imaging air Cherenkov telescope (IACT). Chapter 3 explains the processes by which SNR and PWN generate cosmic rays and emit VHE gamma rays.

The study of VHE sources should allow us to pinpoint objects within our galaxy that are contributing to the flux of cosmic rays detected on Earth. A single VERITAS field of view containing the gamma-ray binary LS 5039 and the PWN HESS J1825-137 is analyzed in Chapter 4 and the PWN DA 495 is discussed in Chapter 5. Final thoughts and conclusion are in Chapter 6.

# CHAPTER 2

## GAMMA-RAY OBSERVATORIES

Most gamma-ray observatories sensitive at energies above about 10 MeV rely on the detection of electrons ($e^-$) and positrons ($e^+$) created as the result of pair-production.[1] Starting at energies of $2m_e c^2 = 1.022\text{MeV}$, where $m_e$ is the mass of an electron and c is the speed of light, a photon has enough energy to pair-produce.

$$\gamma \rightarrow e^- + e^+ \tag{2.1}$$

However, for the $e^-$ and $e^+$ to be generated while conserving both energy and momentum, an additional interacting particle (typically an atomic nucleus) needs to participate and balance the recoil. The probability cross section of this interaction is proportional to $Z^2$, where Z is the atomic number, and the particles involved in the pair-production also retain the remaining fraction of the photon energy (Hubbell, 2006).

The pair-production of high energy photons is exploited in different ways by various observatories to detect gamma rays. These same gamma-ray observatories also detect hadronic cosmic rays since a product of $p^+p^+$-interaction (or cosmic-ray-nuclei) is also gamma rays, and all gamma-ray observatories must be able to differentiate between the incoming photons that pair-produce and the pairs that are created by cosmic rays. There is a certain irony in VHE gamma-ray astronomy also detecting the large flux of cosmic rays, particularly since the number of cosmic rays detected far exceeds the number of detected gamma rays and they are

[1] Not discussed: Compton scattering telescopes, sensitive to lower-energy gamma rays, such as the Imaging Compton Telescope (COMPTEL) on the *Compton Gamma Ray Observatory*.

an intense background noise that must be filtered out through some method of gamma-hadron separation (Hillas, 1996).

This chapter discusses several currently operating gamma-ray observatories and the particular method of detecting gamma rays and gamma-hadron separation implemented by each. VERITAS analysis is also described in the second half of this chapter.

## 2.1 Gamma-ray Observatories

The Large Area Telescope on the Fermi Gamma-Ray Space Telescope (*Fermi*-LAT) uses high-Z foils, with higher interaction cross sections, to induce pair-production of incident photons. The LAT detects the pair of particles generated by gamma rays in two ways. First, the gamma ray enters a tracker unit - which is 16 layers of Tungsten foil interwoven with orthogonal pairs of strip detectors. The gamma ray interacts with one of the Tungsten sheets and the positions of the resulting $e^-$ and $e^+$ are tracked as they pass through the layers of strip detectors. Second, the $e^-$ and $e^+$ pass through a Calorimeter made of an array of CsI(Tl) crystals to measure their energy (Atwood et al., 2007). This method allows for *Fermi*-LAT to have a large field of view and it covers the entire sky over several months as a survey instrument. While there is theoretically no upper limit on the gamma rays that can be detected, it is most sensitive between 20 MeV - 300 GeV (Atwood et al., 2009).

To differentiate cosmic rays from gamma rays, *Fermi*-LAT has an anti- coincidence detector which is used to veto events that originate from incoming charged particles. This is necessary because any non-local charged particle incident on the telescope would interact with the detectors in the same way as a pair-produced $e^-$ and $e^+$. Plastic scintillator tiles surround the tracker and Calorimeter to indicate the presence of high-energy charged particles that penetrate the outer layer of the

spacecraft. This method of rejection has greater than a 0.9997 success rate (Moiseev et al., 2007). *Fermi*'s survey of the GeV sky can be seen in Figure 1.2.

Instead of using foil to catalyze pair-production, ground-based observatories rely on atomic nuclei in Earth's atmosphere to interact with the incoming gamma-ray and typically create the initial pair-production. The first interaction typically occurs at several 10s of km elevation in the atmosphere, and the particles undergo additional interactions in the atmosphere creating an extensive air shower (EAS). Dozens of $e^-$, $e^+$, and secondary gamma rays (which pair produce again...) are typically generated in an EAS before it is exhausted in the atmosphere or reaches the ground. Cosmic rays generate similar showers which additionally consist of pions, muons and other massive particles. This also increases the particle count to the hundreds or thousands (Sinnis, 2009). A schematic view of both gamma ray and cosmic ray air showers are in Figures 2.1 and 2.2, respectively. Take note that the cosmic-ray air shower generates multiple particles from the first nucleus-nucleus interaction.

The High Altitude Water Cherenkov Observatory (HAWC) detects particles in air showers at relatively high elevation. The 300+ water Cherenkov detectors are located at 4200m elevation (Abeysekara et al., 2017b), and this results in about 60% of the radiation lengths compared to sea level in an effort to minimize the shower's expansion through the atmosphere and have fewer particles to track. The particles from the EAS are detected in tanks filled with 190,000L of purified water and several photo multiplier tubes (PMT). Cherenkov light is emitted as the massive, charged components of the EAS pass through the water due to the energetic, super-luminal nature of the particles (Čerenkov, 1937). The rate of energy loss per unit bandwidth, $u(\omega)$, is given as (Longair, 2011)

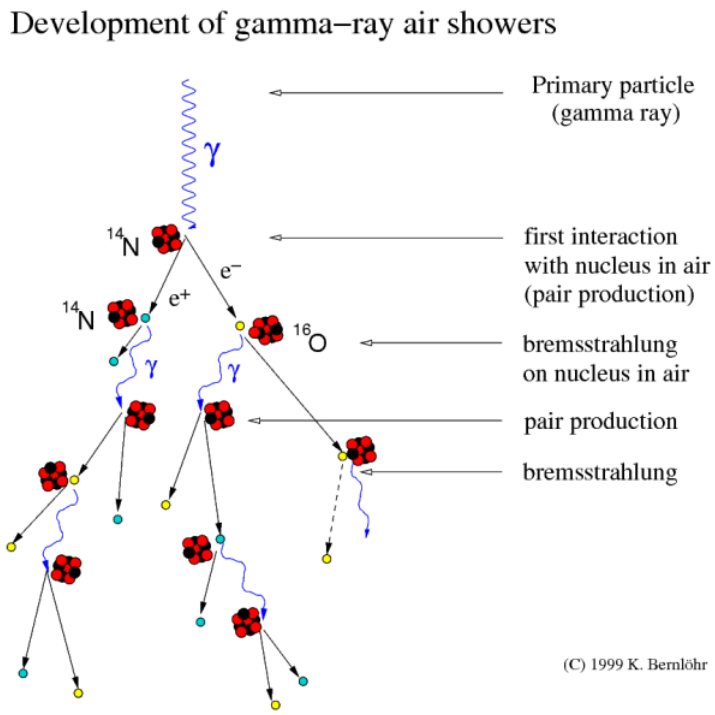


Figure 2.1 A schematic of an air shower generated by a gamma ray that interacts in the atmosphere. Image from https://www.mpi-hd.mpg.de/hfm/CosmicRay/Showers.html.

$$\frac{\mathrm{d}u(\omega)}{\mathrm{d}t} = \frac{\omega e^2 v}{4\pi\epsilon_0 c^3}\left(1 - \frac{c^2}{n(\omega)^2 v^2}\right) \tag{2.2}$$

where $\omega$ is the emitted photon frequency, $v$ is the velocity of the charged particle, and $n(\omega)$ is the frequency dependent index of refraction. The very brief flashes of Cherenkov light are detected by the PMTs in the tanks, where the intensity of the light increases with a larger velocity of the incident particle.

HAWC compares the signature of the EAS's particles to simulations of photonic and hadronic showers in an effort to reconstruct the gamma-ray's trajectory and energy. The number of particles detected can also give an indication as to the shower's original composition (a "bigger" shower typically indicating a cosmic ray instead of a gamma ray). Through this method using 507 days of observations,

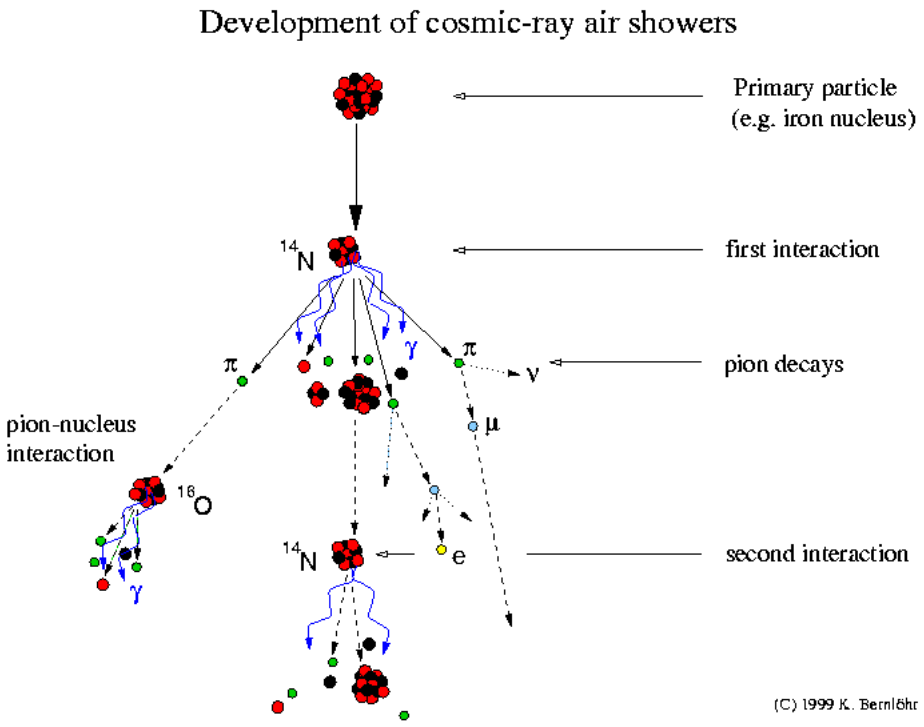


Figure 2.2 A schematic of an air shower generated by a cosmic ray that interacts in the atmosphere. Image from https://www.mpi-hd.mpg.de/hfm/CosmicRay/Showers.html.

HAWC was able to detect 39 TeV gamma-ray sources, 19 of them new (Abeysekara et al., 2017b).

Source detection from either *Fermi*'s or HAWC's surveys often trigger detailed followup by more sensitive, targeted instruments on the ground. The Very Energetic Radiation Imaging Telescope Array System (VERITAS) is one such instrument, located in Southern Arizona at the Fred Lawrence Whipple Observatory. VERITAS is an array of four 12m telescopes and exploits the imaging air Chereknov technique (described more in Section 2.2). Rather than requiring the pair-production particles from the EAS to interact with water, VERITAS detects the super-luminal charged particles produced by the gamma-ray as they are propagating through the atmosphere by the Cherenkov radiation that they emit. The

four telescopes give VERITAS a quadrascopic view of the air shower which allows for more precision in reconstructing the characteristics, such as sky position and energy, of the parent gamma-ray.

Unlike *Fermi* and HAWC, VERITAS has a narrower field of view, but it has sensitive position and energy reconstruction near 1 TeV. The predecessor to VERITAS, the 10m Whipple Observatory on Mount Hopkins, detected the first and most studied gamma-ray source: the Crab nebula (Weekes et al., 1989).

There are two other major IACTs currently in operation. The Major Atmospheric Gamma Imaging Cherenkov Telescope (MAGIC) is a pair of 17m telescopes in the Canary islands. High Energy Spectroscopic System (HESS) is an array of five telescopes in Namibia: four 12m telescopes and one 28m telescope. MAGIC and HESS both operate using the same technique as VERITAS. Details about VERITAS data analysis are in Section 2.2 and the characteristics of *Fermi*-LAT, HAWC and VERITAS are summarized in Table 2.1.

Looking forward, the next generation of ground-based gamma-ray observatory is the Cherenkov Telescope Array (CTA). There is a northern site under construction in the Canary islands and a southern site on the Atacama plateau. CTA will consist of hundreds of telescopes using the imaging air Cherenkov method to extend the effective energy range between 50 GeV - 200 TeV with almost an order of magnitude better flux sensitivity than existing IACTs (CTA Consortium, 2019). The angular resolution is also expected to become better by a factor of two.

## 2.2 Imaging Air Cherenkov Telescopes

Ground-based gamma-ray observatories must use indirect detection methods to pinpoint the sky location of an incoming gamma ray. VERITAS detects Cherenkov flashes to track the relativistic particles' paths and reconstruct the shower gener-

| | *Fermi*-LAT | VERITAS | HAWC |
|---|---|---|---|
| Energy Range | 20 MeV - 300 GeV | 100 GeV - >30 TeV | >100 GeV |
| Effective Area | 9500 $cm^2$ | $>3 \times 10^4$ $m^2$ | $10^5$ $m^2$ @ 1 TeV |
| Angular Resolution | 0.15° - 3.5° | 0.1° | 0.2° - 1.0° |
| Field of view | 2.4 sr | 3° | >1.5sr |
| Location | low Earth orbit | Southern Arizona | Central Mexico |

Table 2.1 Information about some current gamma-ray observatories that are referred to in this thesis (Atwood et al., 2009; Park and VERITAS Collaboration, 2015; Abeysekara et al., 2017b).

ated by the parent gamma-ray. Particle showers that create appropriate images in more than one telescope simultaneously are recorded as events by the array at a nominal rate of about 300 Hz with rates varying slightly based on weather and sky brightness. The recorded output from the telescopes is the result of a live correlation and trigger system that manages the event selection processes at the pixel, telescope and array level. To maximize the area of the telescopes that are under the shower (and to help eliminate camera and optical inconsistencies) observations are made using a wobble where the array as a whole is pointed 0.5° (or more) away from the target. This wobble is rotated through the four cardinal directions on the sky for each 30 minute observation to create an equal exposure on each side of the target.

Hadronic cosmic rays, detected at a rate of about 100 times more than gamma rays, produce a similar shower of particles and are a very loud background, though this particle background can be differentiated and reduced. Each detected shower (hadronic and gamma-ray) produces images on the telescopes that indicate the direction and ground-distance to the shower core. Energy and sky location reconstruction is done by comparing parameterized camera images with simulated observations of showers. The elliptical images generated by the shower vary in width and length based on the shower's progenitor and can be differentiated by a set of geometric parameters established by Hillas (Hillas, 1985). Gamma-ray

showers tend to propagate through the atmosphere for a few generations and only pair-produce throughout whereas showers of hadronic origin create more particles than $e^- - e^+$ pairs and generate a shower that diverges into a wider light pool on the ground. In the cameras, this larger divergent lightpool is manifested by a wider elliptical image as measured by the Hillas parameters. A diagram with the parameters is shown in Figure 2.6 with the parameters briefly described in Table 2.2.

Showers at the lowest energies detectable by VERITAS ($\sim$ 85 GeV) are less easily distinguishable from hadronic showers using Hillas parameters, and higher energy gamma-rays (greater than 1 TeV) are generally easily distinguishable. A key parameter used to differentiate between the types of observed air showers is mean scaled width (mscw), which is the span of the minor axis of the image. The mscw parameter is first scaled based on simulations of air showers, and averaged using the image detected in multiple telescopes. Hadronic cosmic rays tend to have very extended EAS, leading to larger mscw values, and photons tend to have smaller mscw values. The distributions of the mean scaled width between gamma rays and cosmic rays is shown in Figure 2.3. Example images of how the air showers appear in VERITAS's camera are in Figure 2.4.

Choosing appropriate cuts based on the image parameters can affect the sensitivity of the analysis to harder or softer gamma-rays within VERITAS's energy range based on the needs of the analysis. The exact parameter values of the described cuts (hard, medium, soft, etc) are determined using simulations and analysis of known sources. A simple method of gamma-hadron separation using Hillas parameters is called "box cuts" where mscw and other parameters are simply constrained to create the most efficient gamma-hadron separation. In addition to the Hillas parameters shown in Table 2.2, there are derived parameters that can also

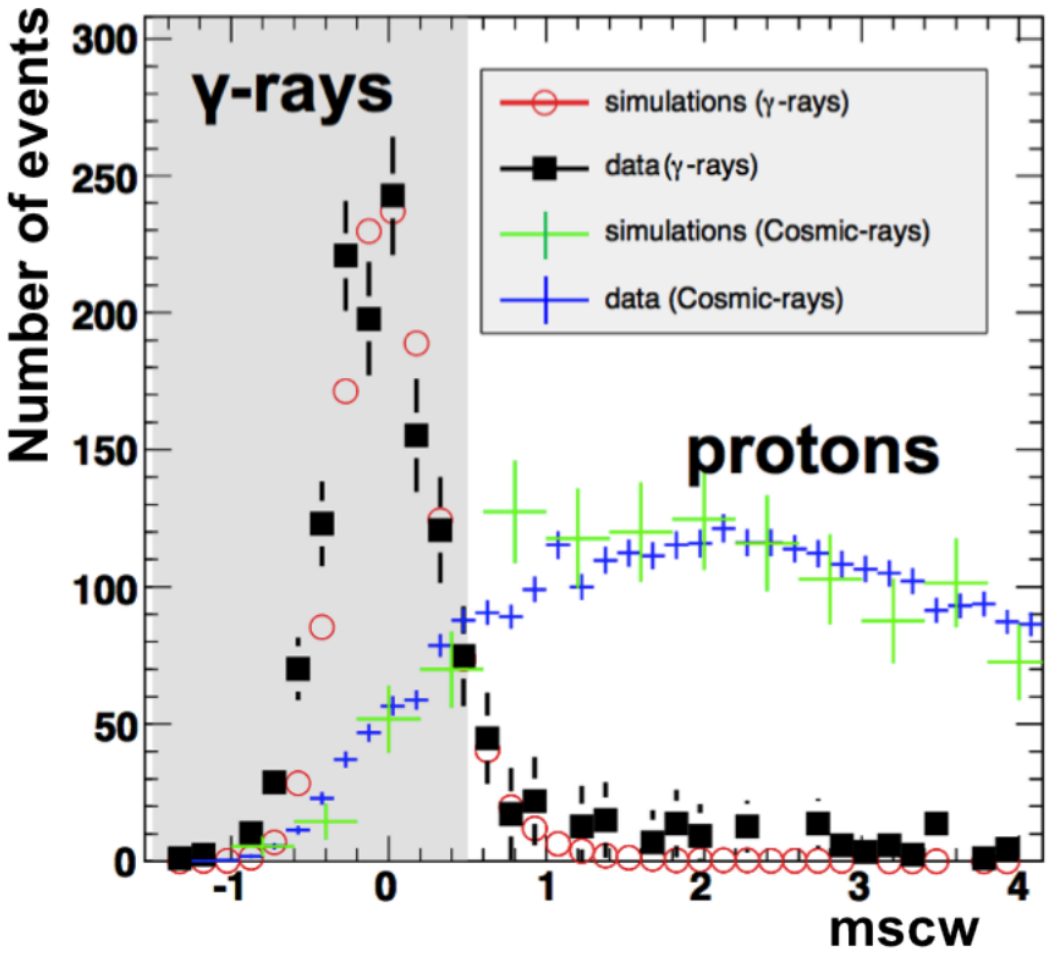


Figure 2.3 The distribution of gamma-ray events and hadronic cosmic-ray events by mean scaled width. The distributions are scaled to similar fluxes for comparison. The shaded region illustrates a selection regime that would best identify gamma rays from this collection of events. Plot from Holder (2015).

provide some quality control such as the distance to the shower core from the center of the array.

Refinement of the gamma-hadron separation process can also be done using machine learning techniques where the image parameters are divided up more finely. VERITAS makes use of boosted decision trees (BDT), trained by simulations with known gamma-ray and hadronic showers, to perform the differentiation (Krause, Pueschel, and Maier, 2017). Decision trees are a data structure that

asks a series of questions using known parameters to determine an unknown parameter. In the case of gamma-hadron separation, the questions asked are based on the known Hillas parameters with the unknown parameter being the EAS progenitor (gamma ray or cosmic ray). The decision tree is trained with simulations where all of the information is known, and training involves optimizing the decision tree to have a certain level of purity with a somewhat efficient level of questioning. Using the distribution in Figure 2.3 as an example, perhaps cosmic rays are ubiquitous with mscw > 1.8, so no other granulation would need to be made. However, additional questions would be needed to discern the origin of a shower image detected at mscw = 1.0.

A disadvantage of decision trees is that they may be susceptible to statistical fluctuations of the training data set. The *boosted* part of BDT means that decision trees are iterated on from a forest of possible combinations to minimize miscategorized events. Miscategorized events are re-weighted as they are sorted within the decision tree again, with an emphasis on placing them correctly. The effectiveness of BDTs compared to traditional box cuts varies by analysis. When comparing results from the Crab nebula, BDTs offered nearly a 25% increase in signal, and only a few tested sources (3 of 23) showing reduced signal. BDTs are particularly effective when evaluating extended sources (Krause, Pueschel, and Maier, 2017).

Directional reconstruction of a gamma-ray event is done by using the camera images and estimating the ground impact of the shower core using the projected major axis of the shower image. With a single telescope image, this can be done by using the ratio of minor and major shower axis to find the distance (like a long or short shadow indicating the elevation of the sun). With multiple telescopes, there are multiple perspectives on the shower, so a stereoscopic reconstruction is possible by finding the common point of displacement from each of the shower images. This is done by projecting the major axis of the shower image from each

telescope in the plane of the sky and finding the common point between them. This is illustrated in Figure 2.5.

After a photon map of the sky has been generated with the remaining gamma rays and reduced hadronic background, the sky map is correlated using an element based on the expected feature size of the target object. For point-like objects this element has an area of $\theta^2 = 0.008$ deg$^2$ which corresponds to a $0.089^\circ$ diameter circle and VERITAS's PSF. For resolvable sources this value can vary.

Since gamma-ray astronomy is dealing with small number statistics, manipulation of the data and selection of the analysis parameters must be done in a purposeful and consistent manner. Most sources are detected at rates of less than 1 $\gamma$ -photon/min, so detections are often based on a total of only a few hundred excess photons in the source region. For each source being tested for a possible detection, the $\theta^2$ and size (energy) cuts are defined *a priori* based on the information gained from the other observatories. Any change in these parameters on the same data set results in a statistical penalty (trial) which can effect the impact of the analysis.

To estimate the statistical significance of a potential source detection, one compares an ON region with an OFF region and follows the process established by Li and Ma (Li and Ma, 1983). The ON region is the region of interest and OFF region is a background region. Equation 2.3 is the equation of most interest. N is the number of counts in the ON and OFF regions, S is the significance, and $\alpha$ is the normalization factor between the sizes of the ON and OFF regions. All significance maps generated by VERITAS use this or a closely related derivation to establish the likely presence of a source compared to the background.

$$S = \frac{N_{on} - \alpha N_{off}}{\sqrt{N_{on} + \alpha^2 N_{off}}} \tag{2.3}$$

Background (OFF) regions are chosen in one of several ways. The most direct approach is to take a dedicated OFF run to compare to the ON observation with the putative source at the same horizon position (ON-OFF method). This has particular advantages for large or unknown morphologies where one wants to make sure that part of the source does not contaminate the OFF counts. Further, this method accounts for a lot of instrumental characteristics such as radial PSF-degradation, which can be modeled, but introduces some additional error. A great disadvantage is that the ON-OFF method may get infiltration by an unknown source in the OFF run. This method is rarely used by VERITAS mostly because of the observational time required.

The reflected region (RE) method takes advantage of a single observation which can be used for both ON and OFF counts by wobbling the source away from the center of the camera. The RE method extracts OFF counts from a region with the same radial distance from the camera center as the source, which is not possible if the source is centered, accounting for many instrumental peculiarities. Further, the OFF region can be larger than the ON region, allowing for the background to be (hopefully) more accurate and less likely to be influenced by statistical fluctuations. The RE method is used primarily for the analysis of point sources as extended sources would quickly crowd the area.

A more familiar method of background extraction (to astronomers) is the ring background (RB) method which takes OFF counts from an annulus around the source from the same observation. This has the advantage that it can be used on moderately extended sources, but not sources that are so big that they fill the field of view. However, one then must take into account the vignetting that occurs with the detection of gamma rays; the rate of detection decreases as the air shower is detected further from the center of the camera. This is due to the optical properties of the telescope, which has a PSF that worsens off-axis, and that showers that appear

near the edge of the camera are missing information and thus are not reconstructed as accurately. The flat fielding calculated as a function of radial acceptance corrects for this in part, but this correction is very dependent on the telescopes position relative to the horizon, and cannot always be applied generally.

The analysis choices in Chapter 4 and Chapter 5 each can be described basically by: the gamma-hadron separation threshold used (Soft, Medium, Hard cuts), the method used for gamma-hadron separation (BDT, box cuts), the integration region ($\theta^2$) used, and the background method used (ON-OFF, RE, RB). These parameters are chosen before any analysis is performed as they will all provide slightly different results, and preference should not be given to the "most significant" result.

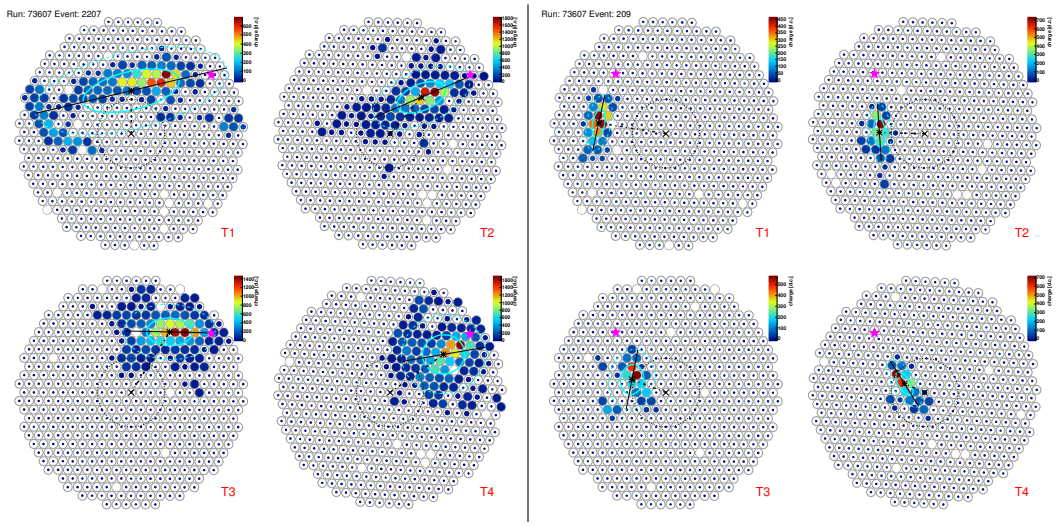


Figure 2.4 VERITAS camera images with the color scale representing the charge accumulated in each photo multiplier tube over a window of 12ns. The light is Cherenkov radiation emitted by super-luminal particles that are generated as part of the extensive air shower. Left: The raw camera images from a putative hadronic cosmic ray. Right: The raw camera images from a putative gamma ray. The image from the cosmic ray is larger and less contained due to the variety and number of particles generated by the hadron's interaction. The image from the gamma ray is narrow due to the presence of only electrons and positrons in a smaller number.

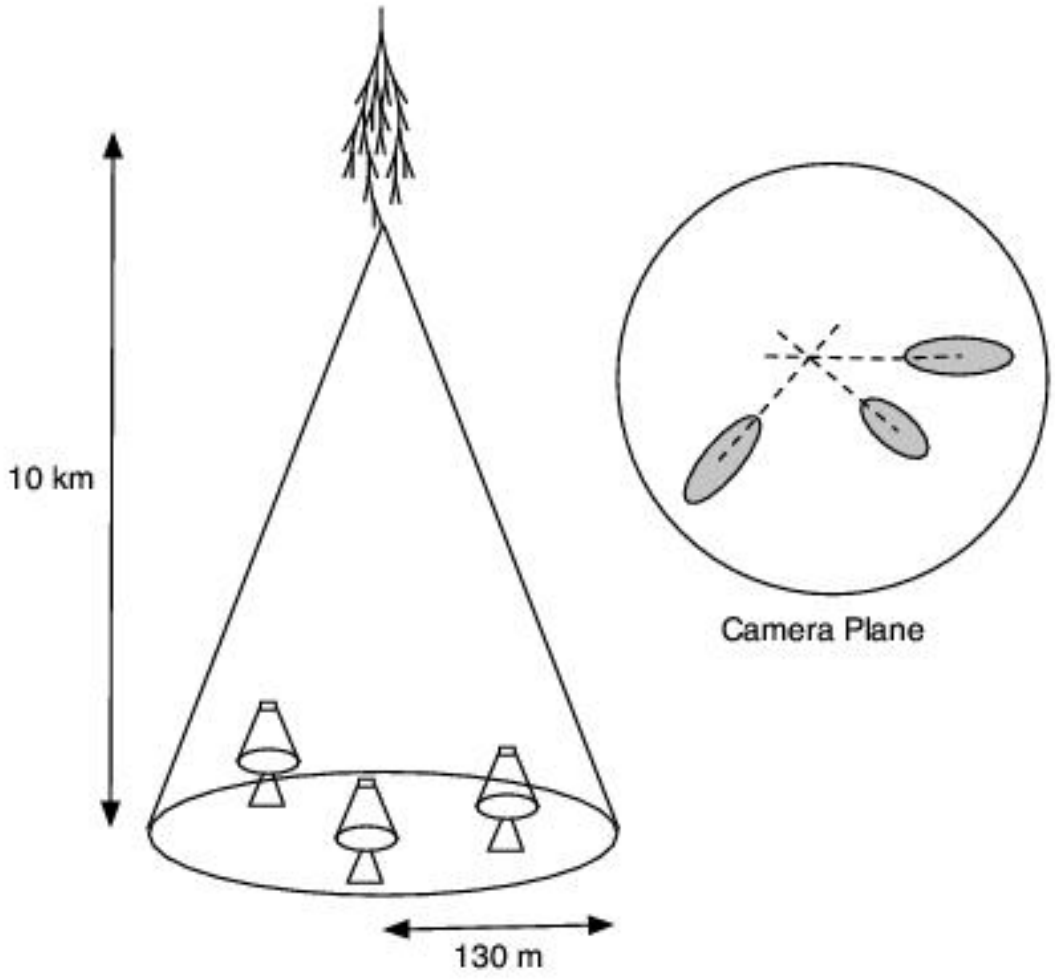


Figure 2.5 The light cone generated from an extensive air shower is shown relative to location of telescopes. The plane of the cameras is shown (each gray ellipse would be separately imaged in different cameras). The image is not to scale. Image from http://veritas.sao.arizona.edu.

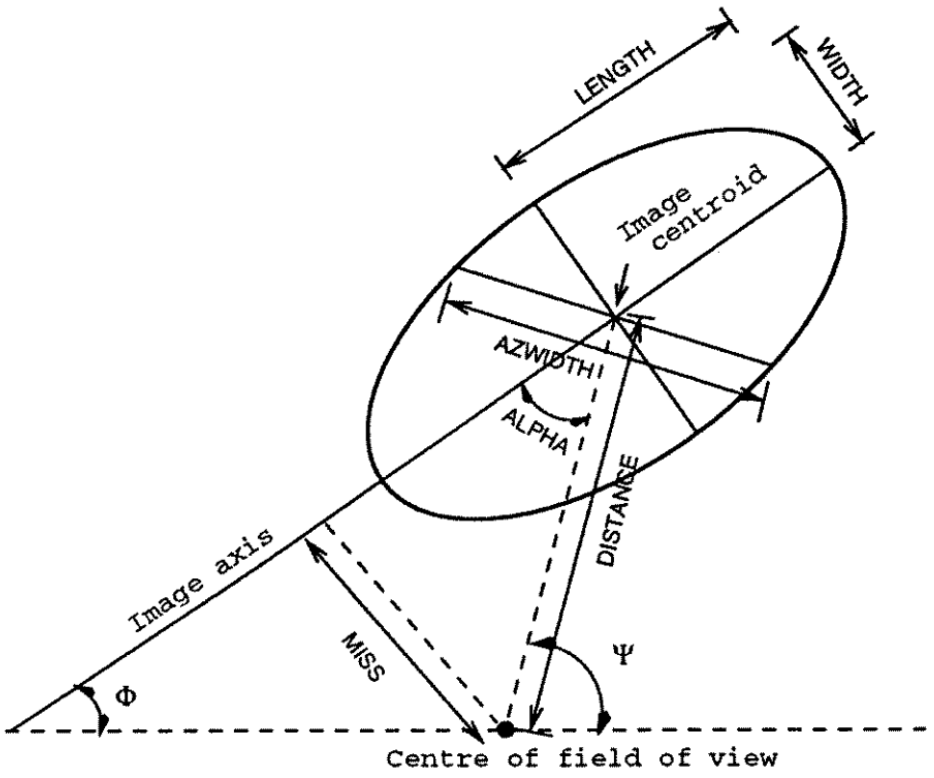


Figure 2.6 Hillas parameters outlined. The shower image is parameterized based on a moment analysis. The parameters are described in Table 2.2. Image from Fegan (1997).

| Name | Description |
|---|---|
| Size | total light in the image |
| Width | rms spread along the minor axis of the image |
| Length | rms spread along the major axis of the image |
| Miss | distance between the major axis of the image and the center of the camera |
| Distance | displacement between the centroid of the image to the center of the camera |
| Alpha | angle between the major axis of the image and a radius drawn from the center of the camera to the image centroid |

Table 2.2 Description of key Hillas parameters shown in Figure 2.6.

# CHAPTER 3

## PARTICLE ACCELERATION AND SUPERNOVA REMNANTS

The life of a star at least 8 times as massive as our Sun ($M_* > 8\ M_\odot$) ends with a core-collapse supernova explosion. During its life as a fusion-powered star, there is a constant balance achieved between the inward gravitational draw of the stellar material and the outward pressure from heat generated by nuclear fusion that is occurring within the core. As heavier elements are produced by fusion, they form concentric layers (often described simply to be like layers of an onion) with the heavier elements towards the center. The temperature and pressure at the center continues to increase, facilitating heavier fusion until the central core is made up of elements that are too heavy and unable to fuse in an energy productive manner (like iron or other near-iron elements). The stellar core becomes an energy sink as the heavy elements capture energetic electrons and the heat generated by the fusion of the lighter elements ceases to be enough to sustain the structure of the star against the ever present gravitational potential. This loss of equilibrium results in a very quick retraction of the surrounding stellar material, whose in falling pressure further compresses against the central core. Some of the material remains with the core and forms a degenerate mass while other material is energetically ejected after rebounding, or bouncing, off of the core.

In the months following a successful supernova, it can be detected and further characterized by the light curve and spectrum. The cooling of super-heated ejecta and nuclear decay are the dominant processes causing detectable emission at this time (Filippenko, 1997). The categorization of supernova is outlined in Table 3.1.

The kinetic energy released into the ejecta is typically about $10^{51}$ ergs with almost 100 times that energy released in neutrinos that escape during the crunch. Depending on mass and other conditions (e.g.: metallicity), the supernova crushes the core into either a neutron star or black hole within a second of the bounce (Steiner, Hempel, and Fischer, 2013). Most of the star's mass is ejected when a neutron star is created, including a significant amount of heavy elements, with less mass and less heavier elements ejected when a black hole is created (Woosley and Weaver, 1995; Sukhbold et al., 2016). This lack of ejecta from a blackhole-creating supernova is supported with observational studies, as no Type II supernova have been found with progenitors of $M_* > 18\ M_\odot$ (Smartt, 2015). This means that the conditions to create a black hole quench the supernova, in part due to material fall back that helps form the black hole, and we do not expect to observe a remnant. It is worth noting that not all very high mass stars create black holes, as the most massive stars ($M_* > 30 M_\odot$) typically become Wolf-Rayet (WR) stars as part of their evolution, and shed their outer hydrogen atmosphere prior to going supernova. WR stars explode as super luminous Type 1b/c supernovae with exceptionally large fractions of their mass ejected during the supernova ($M_{ej} > 10\ M_\odot$). They are likely to leave a magnetar, a pulsar with exceptionally strong magnetic fields (Nicholl et al., 2015).

This chapter will explore the particle acceleration and subsequent electromagnetic emission mechanisms of supernova remnants and the pulsar wind nebulae that often are found after a core-collapse supernova.

## 3.1 Neutron Stars

The most dense part of the stellar core, nearly all iron, is crushed during a supernova into a neutron star (presuming it does not further collapse into a black

| | Type | Feature | Cause |
|---|---|---|---|
| Type I No H Emission | Type Ia | Si II emission | T |
| | Type Ib | He I lines | CC |
| | Type Ic | No He I or Si II feature | CC |
| Type II H Emission | Type IIP | Lightcurve plateaus | CC |
| | Type IIL | Lightcurve decreases linearly | CC |
| | Type IIb | Hydrogen emission present initially, but fades to Type Ib | CC |

Table 3.1 The classification of supernova explosions by their spectrum and light curve. The broad classification is the presence of neutral hydrogen emission. In the last column, CC indicates core-collapse as the cause, and T indicates thermonuclear runaway as the cause.

hole). At creation, nearly all neutron stars have a mass and radius, $M_* \approx 1.4_\odot$ and $r \approx 10$km (Lattimer, 2012). When a neutron star is created, it retains much of the angular momentum and magnetic flux of the parent star which results in a very fast rotating neutron star, called a pulsar, with exceptionally strong magnetic fields of $B > 10^{12}$ G (Lattimer and Prakash, 2004). The magnetic and rotational axis are often misaligned causing a pulsing beacon of emission from the pole of the retained dipole magnetic field. This is often visualized as a lighthouse with a directed cone of light that traverses our line of sight as the pulsar spins. The fastest rotating pulsar, PSR J1748-2446ad, was found to be spinning at 716 Hz (period $P = 0.0014$ s) (Hessels et al., 2006), but not all pulsars are as extreme as PSR J1748-2446ad, with most pulsars having spin periods closer to 1 s. The pulsar contributes its rotational energy to the environment beyond the initial supernova explosion, and drags the magnetic field through the local region which causes charge separation and an electric flux.

The pulsar has an exceptionally strong dipole magnetic field due to conserving the magnetic flux of the original star. The original treatment of rotating magnetic neutron stars was done by Goldreich and Julian (1969), and they demonstrated the necessity of strong external magnetic fields due to the conductive na-

ture of the star. The magnetic field can be thought to be following the rotation fairly rigidly, so the magnetic field lines are only able to reconnect within radius $r < cP/2\pi$ ($r \approx 5 \times 10^4$ km in our typical pulsar case) while maintaining causality. The region within this radius is called the light cylinder and the magnetic field structure inside this region is still well defined as a dipole. Outside of the light cylinder the open magnetic field lines allow some charged particles to escape the pulsar creating a charge imbalance on the surface which results in a potential difference with the surrounding medium. A schematic of a pulsar and its magnetic field in shown in Figure 3.1. The potential difference generated by the rotating dipole is (Goldreich and Julian, 1969; Gaensler and Slane, 2006):

$$\Delta\Phi \approx \frac{B_p \Omega^2 R_{NS}^3}{2c} \approx 6 \times 10^{12} \Big(\frac{B_p}{10^{12}\ \mathrm{G}}\Big)\Big(\frac{R_{NS}}{10\ \mathrm{km}}\Big)^3\Big(\frac{P}{1\ \mathrm{s}}\Big)^{-2}\mathrm{V} \tag{3.1}$$

where $B_p$ and $R_{NS}$ are the magnetic field and radius of the neutron star. So, for a typical pulsar with $B_p = 10^{12}$ G, $R_{NS} = 10$ km, and $P = 1$ s - electrons leaving the light cylinder will gain energy of up to 6 TeV. These relativistic electrons flow out in a wind and eventually generate a termination shock once they approach a region of low of enough density to be traveling subsonically.

To maintain the flow of particles, they must be created within the atmosphere of the NS. This is done by pair production that is a result from electromagnetic radiation that is given off due to the pulsar slowing. The energy injected into the environment in the form of electromagnetic radiation comes from the spin down of the pulsar over time and can be related to the current rotational rate of the pulsar

$$-\frac{\mathrm{d}E_{rot}}{\mathrm{d}t} = -\frac{4\pi^2 I \dot{P}}{P^3} \tag{3.2}$$

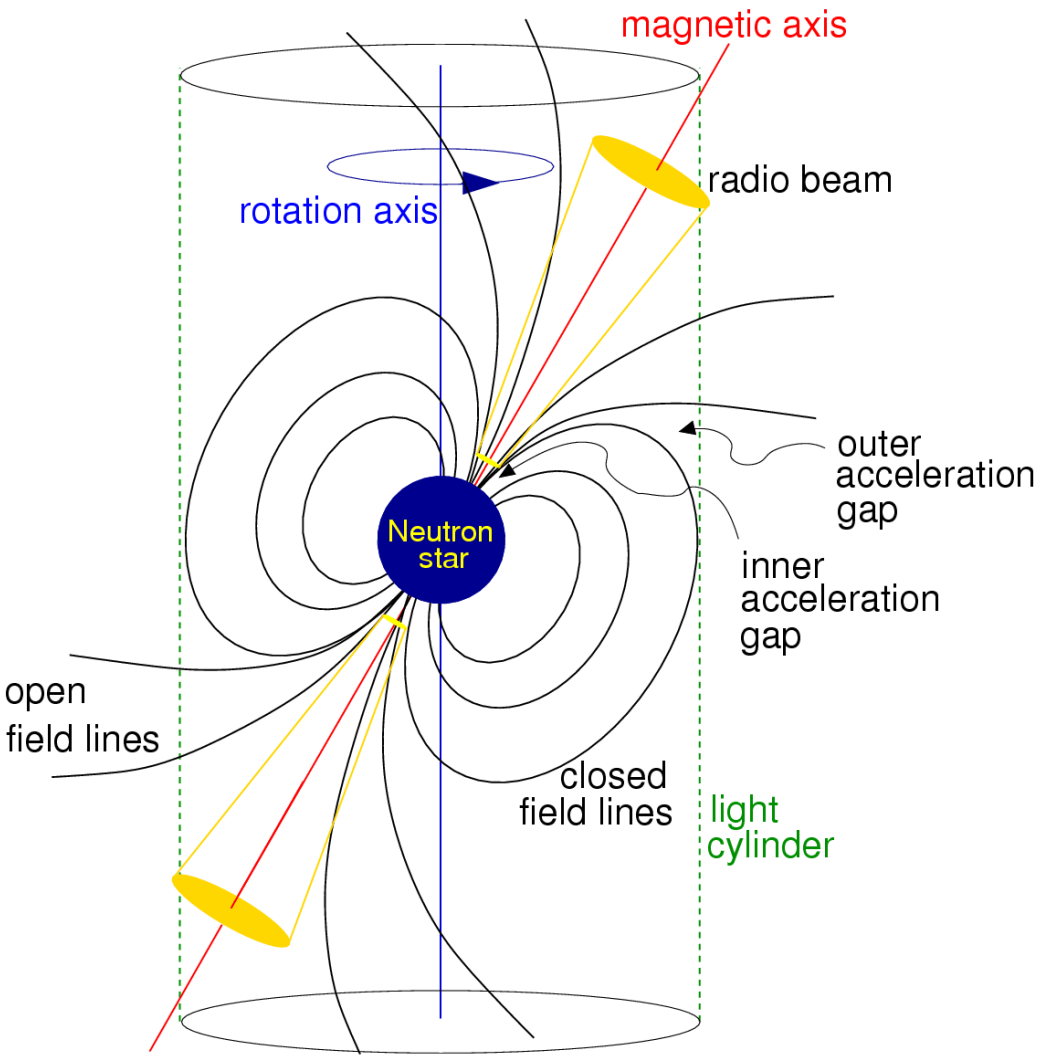


Figure 3.1 A sketch of a pulsar showing the rotation and magnetic axis. Magnetic field lines outside of the light cylinder are open since they are limited by causality in orbits that would require them to exceed the speed of light. Image from Lorimer and Kramer (2012).

where $I$ is the moment of inertia of the pulsar (Longair, 2011). The rotational energy stored in pulsars is tremendous and we can relate the rotational kinetic energy $E_{\text{rot}}$ to the moment of inertia by

$$E_{\text{rot}} = \frac{I\Omega^2}{2} = \frac{2\pi^2 I}{P^2} \tag{3.3}$$

So, a canonical pulsar with moment of inertia $I = 2MR^2/5 \approx 10^{45}$ g cm$^2$ would have an energy reservoir of $E \approx 2x10^{46}$ erg. If we presume a $\dot{P} = 10^{-15}$, which is a typical period derivative (Johnston and Karastergiou, 2017), then the Luminosity is $L \approx 2 \times 10^{33}$erg s$^{-1}$ or about $1L_{\odot}$. Our canonical scenario is a fairly mundane pulsar, and if we take the energetic Crab pulsar's $P = 0.033$ s and $\dot{P} = 10^{-12.4}$ (Lyne, Pritchard, and Graham-Smith, 1993) then we get about $4 \times 10^{38}$ erg s$^{-1}$ or $10^5 L_{\odot}$. Energetic pulsars, like the Crab need to expend that energy in other ways besides their lighthouse, and form bright pulsar wind nebulae (PWNe) powered by their particle outflow.

## 3.2 Pulsar Wind Nebula

A PWN starts its existence at the center of a supernova and its early evolution involves expansion of the relativistic particle wind into the supernova cavity. The pressure difference between the wind and the surrounding medium forms a wind termination shock at radius $R_w$

$$R_w = \sqrt{\dot{E}/(4\pi\omega c\mathcal{P}_{\text{PWN}})} \tag{3.4}$$

where $\omega$ is the equivalent filling factor for an isotropic wind and $\mathcal{P}_{\text{PWN}}$ is the total pressure in the shocked interior. This gives typical radii of tenths of parsecs (Gaensler and Slane, 2006). At this termination shock, ejecta is thermalized again

and is visible throughout the electromagnetic spectrum. Particles are also accelerated at the shock by first order Fermi acceleration.

In addition to the termination shock, PWN can have polar jets understood to be formed by the variation in the Poynting flux as a function of angle from the magnetic axis. Using a magnetiziation parameter $\sigma$ to define the ratio of magnetization and particle strength (Kennel and Coroniti, 1984)

$$\sigma \equiv \frac{F_{E\times B}}{F_{particle}} = \frac{B^2}{4\pi\rho\gamma c^2} \tag{3.5}$$

where $B$ is the magnetic field, $\rho$ is the mass density, and $\gamma$ is the Lorentz factor. $\sigma > 10^4$ is obtained near the magnetic poles, and $\sigma << 1$ are expected behind the termination shock to meet the boundary conditions (Arons, 2002). This can be explained by the equatorial flow of particles outside of the light cylinder not being dominated by the Poynting flux any longer and dependent on the already accelerated flux of particles. At the poles, likely emitted from within the light cylinder, jets are Poynting flux dominated.

Together, the equatorial wind forming a termination shock as a torus and the magnetically dominated jet form the typical PWN picture of a jet-torus morphology. This is best seen in the Crab nebula, which is pictured in Figure 3.2.

## 3.3 Supernova Evolution

Regardless of the stellar remnant created by the supernova, black hole or neutron star, there is a tremendous amount of energy released into the surrounding environment via the ejected material that was not compressed into the core. The approximately $10^{51}$ ergs worth of kinetic energy is released slowly into space and detection of this energy loss is referred to as the supernova remnant. To clearly differentiate this emission from a PWN, this type of emission is referred to as a

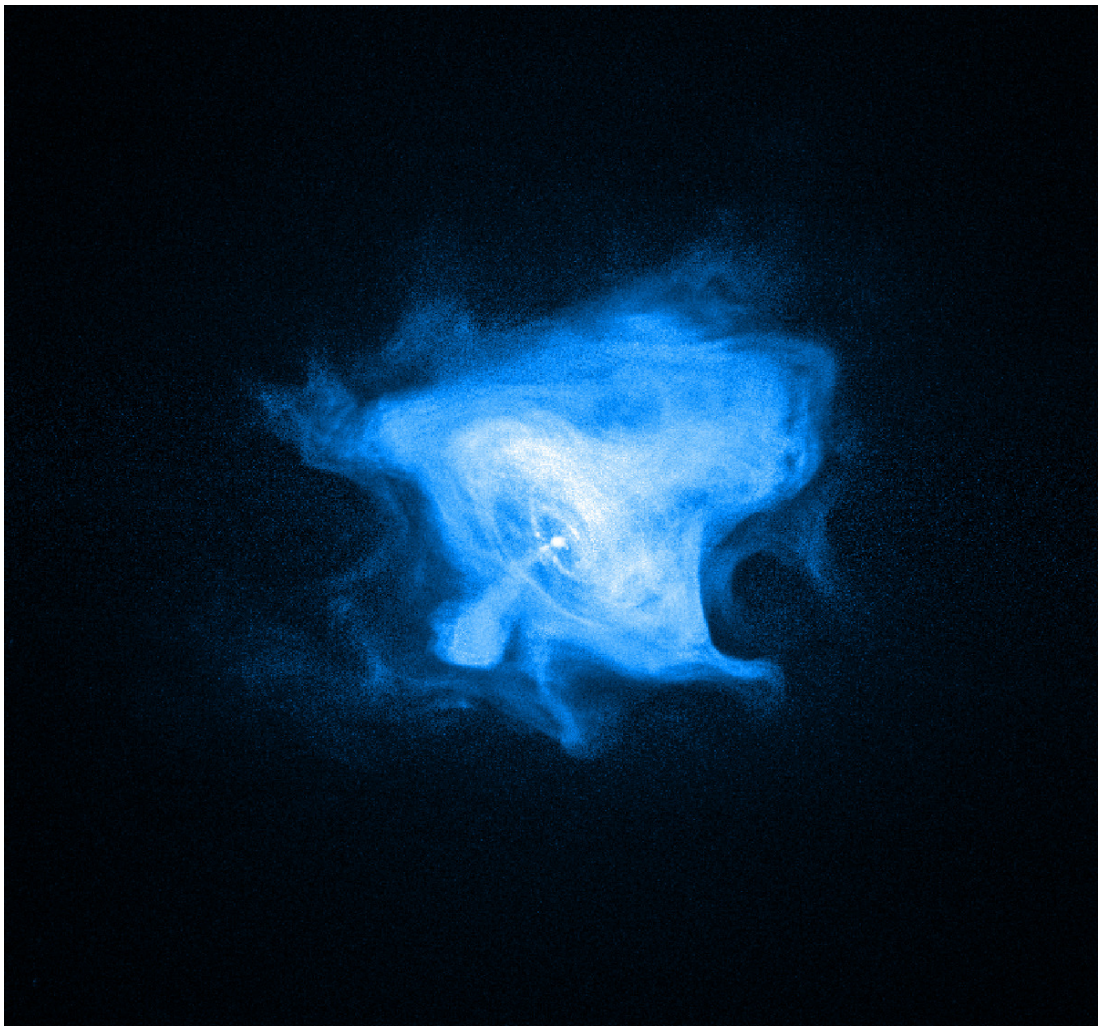

Figure 3.2 Crab nebula as seen by the Chandra X-ray observatory. The neutron star is in the center with jets being emitted from the poles. The inner most ring is downstream from the termination shock where freshly accelerated particles are seen emitting Synchrotron radiation. Image credit: NASA/CXC/SAO/F.Seward et al.

"shell-type" supernova remnant due to the emissive shell that is generally visible and in contrast to the central emission from the PWN.

The evolution of the supernova remnant can be broadly categorized by four phases, with the key phrase for each phase in **bold** (Reynolds, 2008):

1. Ejected material from a core-collapse supernova starts moving outward at velocities of $\sim 5000$ km s$^{-1}$, while slower ejecta cools very quickly behind it during a period of **free expansion**.

2. Once the outer shock interacts with circumstellar material (CSM) or interstellar medium (ISM) it slows quickly, depositing energy into the material, and causes a reverse shock which heats with the previously cooled ejecta and enters an **adiabatic (Sedov-Taylor)** evolution.

3. The outer shock continues outward to sweep material like a **snow plow** until it has gathered at least the initial ejecta mass. The supernova remnant gains density and shell thickness during this time.

4. Density starts to impede free expansion until **radiative** losses start to dominate and the supernova remnant fades into the ISM .

## 3.4 First Order Fermi Acceleration

The broadband spectra of SNRs and PWNe contain strong non-thermal emission components that cannot be produced by any thermal arrangement of particles. Instead, the typical particle energy spectrum in SNR and PWN is described as simple power laws with $N(E) \propto E^{-p}$, with $p \approx 2$. Most non-thermal acceleration in SNR is widely accepted to be from first-order shock acceleration first proposed by Fermi (1949) (with extensions in Bell (1978) and Bell (2013)). To derive the first-order Fermi acceleration we will follow the notation from Longair (2011).

When there is an adiabatic shock of an monoatomic ideal gas (with ratio of specific heats, $\gamma = \frac{5}{3}$) that is traveling at velocity $U$ (panel a in Figure 3.3), $\rho_1 v_1 = \rho_2 v_2$ must be true to conserve mass. Additionally, we can relate the density ratios

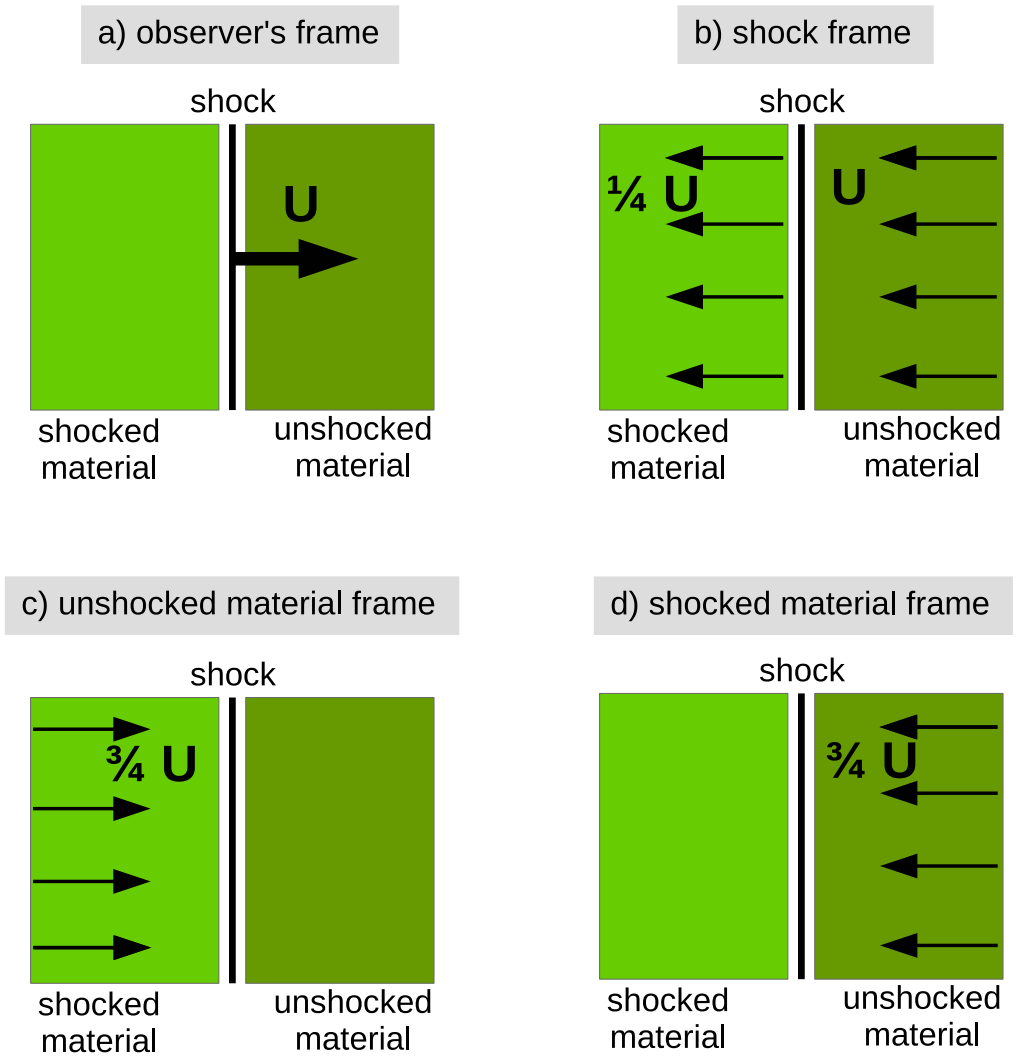


Figure 3.3 Illustration of the different frames of reference regarding Fermi first order acceleration.

to the specific heats in a strong shock as $\rho_2/\rho_1 = (\gamma+1)/(\gamma-1)$, which gives us the relationship

$$\frac{\rho_2}{\rho_1} = \frac{v_1}{v_2} = \frac{\gamma+1}{\gamma-1} = 4 \tag{3.6}$$

$\rho_1$ and $v_1$ are the density and velocity in the unshocked region (upstream). $\rho_2$ and $v_2$ are the density and velocity in the shocked region (downstream).

In the rest frame of the shock, it must follow then, $v_1 = U$ and $v_2 = \frac{1}{4}v_1 = \frac{1}{4}U$. Transforming between the shock's frame (panel b in Figure 3.3) and each side of the shock leads then to an interesting conclusion. The velocity of the shocked[unshocked] material in the unshocked[shocked] frame is always $V = \frac{3}{4}U$ towards the shock (panes c and d of Figure 3.3). This means that a particle that crosses the shock from either side will encounter particles head-on that are approaching at $V = \frac{3}{4}U$, allowing for a continual transfer of energy for a particular particle crossing the shock in either direction. With a Lorentz transformation, the particle's energy after it bounces back across the shock due to scattering is:

$$E' = \gamma_V(E + p_x V) \tag{3.7}$$

where $p_x$ is the particle's momentum perpendicular to the shock. We also presume that the shock is non-relativistic ($U << c$) and so $\gamma_V = 1$. However, the particles are relativistic so that for a particular particle $E = pc$ and $p_x = \frac{E}{c}\cos\theta$. The relative energy gain for a particle crossing the shock is

$$\frac{\Delta E}{E} = \frac{V}{c}\cos\theta \tag{3.8}$$

Averaging the probability of interacting with another particle as it crosses at angle $\theta$, and accounting for two crossings across the shock gives an average round-trip fractional energy increase of

$$\langle\frac{\Delta E}{E}\rangle = \frac{4}{3}\frac{V}{c} \tag{3.9}$$

To account for the loss of particles from the ping-pong match across the shock, we need to introduce $P$ as the probability that a particle stays in the region to continue to cross the shock, $\beta$ as the factor at which energy increases each pass, and

$k$ as the number of times a particle has crossed. So then, the number of particles is $N = N_0 P^k$ with energies $E = E_0 \beta^k$. To eliminate $k$ between the quantities

$$\frac{\ln(N/N_0)}{\ln(E/E_0)} = \frac{\ln P}{\ln \beta} \tag{3.10}$$

$$\frac{N}{N_0} = \left(\frac{E}{E_0}\right)^{\ln P/\ln \beta} \tag{3.11}$$

Equation 3.10 simplifies into 3.11. Then, noting that N particles with greater energy than E, we get ($A$ is a constant):

$$N(E)\mathrm{d}E = A \times E^{-1+(\ln P/\ln \beta)}\mathrm{d}E \tag{3.12}$$

Using Equation 3.9, we can then find that the average change in energy for each round trip is

$$\beta = 1 + \frac{4}{3}\frac{V}{c} \tag{3.13}$$

The probability of a particle actually leaving the shock per unit time is $\frac{U}{c}$, which means that $P = 1 - \frac{U}{c}$ and

$$\ln P = \ln\left(1 - \frac{U}{c}\right) \approx -\frac{U}{c} \tag{3.14}$$

Combining that with Equation 3.13 ($\ln\beta = \frac{4}{3}\frac{V}{c} = \frac{U}{c}$), we find that $\ln P/\ln \beta = -1$. So, using Equation 3.12, we get

$$N(E)\mathrm{d}E = A \times E^{-2}\mathrm{d}E \tag{3.15}$$

This shows that first order Fermi acceleration of particles can match the observed spectrum of a shocked region and in-fact forms the basis for the particle energy spectrum for SNR and PWN.

## 3.5 Bremsstrahlung Radiation

A charged particle approaching another charged particle must slow down (and loses some kinetic energy) as it is deflected. To balance the energy loss some radiation is emitted as Bremsstrahlung radiation (German for *braking*). This also sometimes called *free-free* emission to differentiate from atomic line emission which is caused by bound electrons and nuclei. The average energy loss of an electron due to relativistic Bremsstrahlung radiation is (Longair, 2011)

$$-\Big(\frac{\mathrm{d}E}{\mathrm{d}t}\Big) = \frac{Z(Z+1.3)e^6 N}{16\pi^3\epsilon_0 m_e^2 c^4 \hbar} E[\ln\Big(\frac{183}{Z^{1/3}}\Big) + \frac{1}{8}] \tag{3.16}$$

Where $Z$ is the atomic number of the nucleus that is being buzzed by the electron. The energy loss rate is proportional to $E$ of the electron leading to an exponential loss of energy by the electron, and a spectral power spectrum that is the same shape as the particle spectrum.

## 3.6 Synchrotron Radiation

When a charged particle moves through a magnetic field, it feels the Lorentz force: $\mathbf{F} = q(\mathbf{E} + \mathbf{v} \times \mathbf{B})$. The charged particle is deflected with a resulting force component that is perpendicular to both the velocity of the particle and the magnetic field. This motion creates a continual deflection in a circular (cyclotron) motion as the charged particle continues to move. The constant (de)acceleration of the charged particle causes it to radiate and when a relativistic particle does this due to cyclotron motion in a magnetic field we call it synchrotron radiation.

The total synchrotron energy loss rate for a single electron is given as (Longair, 2011)

$$-\left(\frac{\mathrm{d}E}{\mathrm{d}t}\right) = \frac{4}{3}\sigma_T c U_{mag}\gamma^2\left(\frac{v}{c}\right)^2 \tag{3.17}$$

Where $\sigma_T$ is the Thompson cross section and $U_{mag}$ is the magnetic field energy density. For a distribution of particles, it is expected that the pitch angle is isotropic for high energy electrons, so this formula includes the averaged pitch angle. The variables of interest in this case are $U_{mag}$ and $\gamma^2$ which are both proportional to the energy loss rate and depend on the object of interest. For relativistic electrons, the $\frac{v}{c}$ factor quickly approaches unity and the Lorentz factor takes over.

For a population of electrons defined by a power-law spectrum ($\frac{dN}{dE} \propto E^{-p}$) Equation 3.17 leads to the following form for the specrum of radiation emitted by the population,

$$J(\nu) \propto B^{(p+1)/2}\nu^{-(p-1)/2} \tag{3.18}$$

Where $J(\nu)$ is the frequency dependent emissivity and $p$ is the electron spectral index.

The synchrotron cooling drains higher energy particles far more quickly and this turnover can additionally give some information about the lifetime of the involved particles. As was used in Kothes et al. (2008) when studying DA 495 (further discussed in Chapter 5), the characteristic age of a PWN can be given by the apparent cutoff frequency $\nu_c$ in the synchrotron spectrum,

$$\nu_c = 1.187B^{-3}t^{-2} \tag{3.19}$$

where $B$ is the magnetic field strength in Gauss, $t$ is the age of the PWN in years, and $v_c$ is the cutoff frequency in GHz. This contains some additional information based on the expected energy and particle injection history of the pulsar, but the fundamental synchrotron cooling relationship is still evident where over time -

the higher energy electrons will cool off faster than the lower energy electrons indicated by a spectral break and strongly dependent on magnetic field strength.

## 3.7 Inverse-Compton Scattering

In addition to Synchrotron radiation, ultra-relativistic electrons can transfer their energy directly to incident photons. Whereas Compton scattering is the process in which a photon imparts energy to lower energy electrons, inverse-Compton scattering (IC) is the process that allows the opposite - a high energy electron imparting energy to a lower energy photon. The average energy loss of a single electron, where $U_{rad}$ is the strength of the radiation field, can be given by (Longair, 2011)

$$-\left(\frac{\mathrm{d}E}{\mathrm{d}t}\right) = \frac{4}{3}\sigma_T c U_{rad} \gamma^2 \left(\frac{v}{c}\right)^2 \tag{3.20}$$

Similar to Synchrotron radiation (and virtually identical in form), the energy loss is proportional to $\gamma^2$ which makes it highly efficient at very high energies. However, instead of varying based on the magnetic field, it is dependent on the incident photon spectrum. The incident photon spectrum is often made up of a combination of the 2.7K cosmic microwave background (CMB) and the synchrotron component from the same electron population. A $\gamma = 1000$ electron (about 500 MeV) could singly boost a CMB photon to UV energies (incident photons with frequency $\nu_0$ get scattered to $\nu$ by $\nu \approx \gamma^2 \nu_0$). The optical synchrotron photons can get scattered to gamma-rays through Synchrotron self-Compton (SSC), and so on.

Since the energy loss rates of IC and Synchrotron have the same dependence on electron energy, it becomes very simple to get a comparison of the different features. The ratio of the Synchrotron and IC total power can be understood as the ratio of the magnetic and photon field strengths.

$$\frac{P_{sync}}{P_{IC}} = \frac{U_{mag}}{U_{rad}} \tag{3.21}$$

## 3.8 $\pi_0$ Decay

Virtually all of the emission from the previous described processes is the result of energy transfer from ultra relativistic electrons. Through diffusive shock acceleration, protons and other heavy nuclei can also obtain very high energies. Evidence for these particles being accelerated is due to the decay of neutral pions ($\pi^0$) that are created during the interaction of a pair of hadrons (most simply - a pair of protons).

$$p + H \rightarrow \pi^0 + (anything) \tag{3.22}$$

$$\pi^0 \rightarrow 2\gamma \tag{3.23}$$

The mass of a $\pi^0$ is 140MeV$/c^2$, so the decay in the rest frame of the particle creates a pair of 70 MeV photons. This manifests itself as a bump in the gamma-ray spectrum that stands out compared to the otherwise fairly smooth lepton-based emission mechanisms and cutoff below 70 MeV.

## 3.9 Observational Characteristics of SNR

Radio observations of supernova remnants were initially described as being center-filled or shell-type remnants. The morphology available allowed for this early distinction. The Crab nebula was the first to be distinctly considered as a plerion, meaning center-filled, instead of a "normal" (at the time) supernova remnant (Weiler and Panagia, 1978), and this was realized in part due to the presence of pulsars in most of the center-filled remnants. The pulsars provided an energy

reservoir that could continually accelerate particles in the interior of the SNR, as it was expected that any particles interior to the supernova shock and originally accelerated by the supernova would cool quickly and not demonstrate any emission.

A broadband spectrum of the Crab fit to emission processes in a PWN is shown in Figure 3.4. Each of the processes have a dominant regime, e.g.: radio is dominated by Synchrotron emission and TeV by inverse-Compton. This allows for some simplifications of the interpretation as one can just compare the total power in each waveband to determine the ratio of photon and magnetic energy densities (as in Equation 3.21). There is significant particle injection into the nebula still from the pulsar, so the synchrotron emission extends well into X-rays for the Crab nebula as well. If the pulsar were to turn off, a peak would become more pronounced as the X-ray emitting electrons cooled in the magnetic field as in Equation 3.19.

A shell-type SNR, whose emission is dominated by the expanding shock region caused by the supernova, is thought to accelerate particles in the expanding shock (after the initial explosion). Synchrotron emission is due to the free electrons interacting with the magnetic fields caused by the charges in motion. A dominant component of the gamma-ray emission is possibly from protons, as evidenced by $\pi^0$ decay resulting in a spectral feature compared to the otherwise smooth leptonic emission scenarios. An example broadband spectrum from a shell type SNR is shown in Figure 3.5. It should be emphasized that later analysis including *Fermi*-LAT observations helped to further constrain the spectrum and demonstrated that the gamma-ray emission was in fact leptonic and caused by IC (Abdo et al., 2011).

By modeling the emission from these SNR/PWN we can gain understanding into the history of the object. For example, the amount of ejecta can help to narrow down the progenitor star, and help to identify if the remnant is a result of a core-collapse of a massive star or thermonuclear event from an accreting white dwarf.

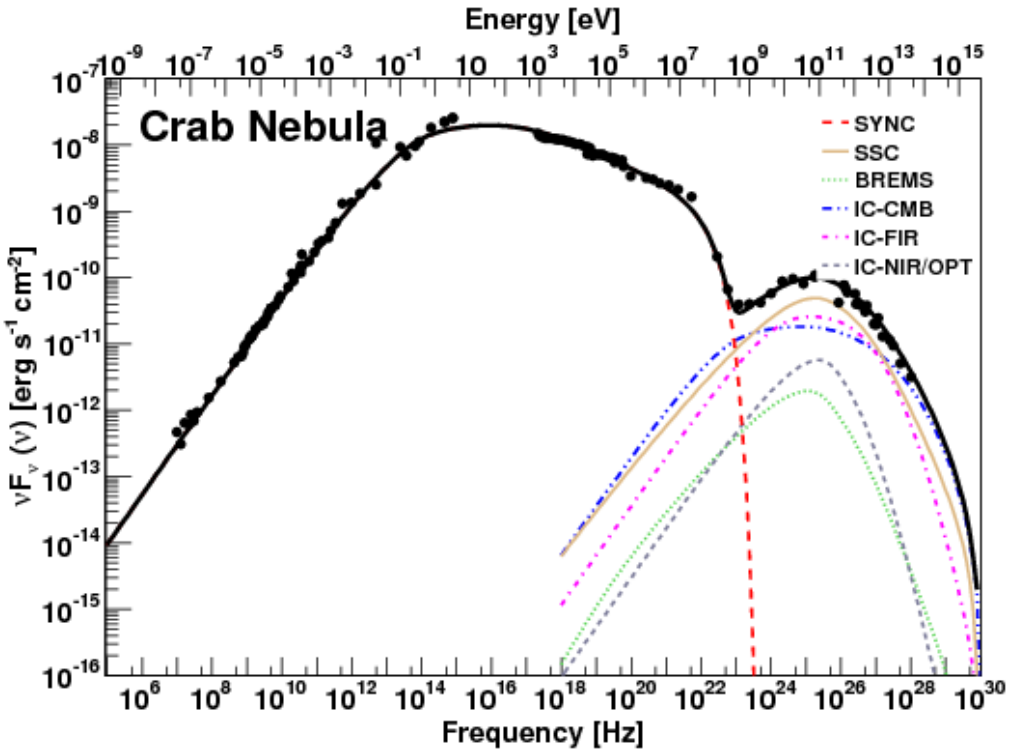


Figure 3.4 A fit spectra energy distribution of the Crab nebula, the prototypical PWN, which incorporates emission from Syncrotron between Radio and X-ray energies and inverse-Compton emission with several seed photon distributions at gamma-ray energies. There is also a weak relativistic Bremsstrahlung component in the gamma ray regime. In this case, the particle spectrum was evolved over time to find the best fit. Image from Torres et al. (2014).

The emission models incorporate parameters that are linked between the various emission mechanisms like density, pressure, magnetic field and total energy. If a pulsar is present, then the additional injection of particles needs to be accounted for as well. Using these tools and some additional physical constraints help to better understand the objects in Chapter 4 evaluate the nature of DA 495 in Chapter 5.

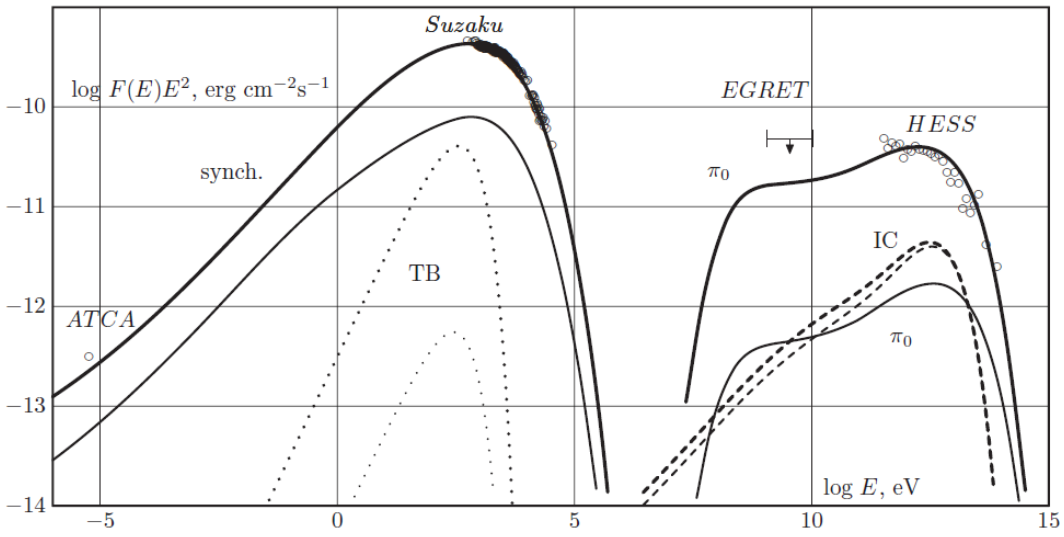


Figure 3.5 A fit spectra energy distribution of the SNR RX J1713.7-3946, the first SNR where TeV emission definitively came from the shell of the remnant. The thin lines represent the contribution from the reverse shock of the SNR, while the thick lines represent emission from the main forward shock. Spectral points from radio, X-ray, and gamma-ray observations are also included. RX J1713.7-3946, thought to be associated with a supernova that appeared as a guest star in 393AD, is about 1600 yr old and at a distance of D = 1.2 kpc. No associated pulsar is detected in any wavelength (Zirakashvili and Aharonian, 2010).

# CHAPTER 4

## LS 5039 AND HESS J1825-137

In this chapter I will explore two objects that are within the same field of view - one of which has measured variability on day time scales and one that is thought to be molasses in space. LS 5039 is a high-mass X-ray binary that may have a pulsar-wind nebula closely orbiting and interacting with a massive star. HESS J1825-137 is a large pulsar wind nebula that has extended its reach to span many parsecs of space. They are separated (center-to-center) by 1° on the sky, so they are within the same field of view for very high energy gamma-ray instruments like VERITAS. The most sensitive observations suggest some overlap on the sky, but they are not thought to be physically interacting. They may be very similar objects that can be explained by the same mechanisms, and likely had very similar origins, but the environment that each object was put into has dramatically changed their structure. The emission that we see provides insight to each object's unique evolution.

The key results of this chapter are submitted for publication in Astroparticle Physics in the article titled *VERITAS Detection of LS 5039 and HESS J1825-137*. The text has been expanded upon, since the paper was a short-format article, and some additional explanatory material has been added.

## 4.1 VERITAS Observations

The field containing LS 5039 and HESS J1825-137 was observed by VERITAS in late spring of 2013 and 2014. The observations were centered on LS 5039 and were taken with the standard 0.5° wobble, shifting in cardinal directions on the sky. Conditions were typically good with most 30 minute runs having minimal

| Date *yyyymmdd* | Run ID | Usable Time *min* | Wobble | Weather Grade | Elevation *degrees* |
|---|---|---|---|---|---|
| 20130608 | 69054 | 34 | N | A | 36 |
| 20130612 | 69123 | 30 | S | B | 42 |
| 20130616 | 69187 | 30 | E | D | 43 |
| 20130616 | 69188 | 30 | W | A | 42 |
| 20130617 | 69202 | 30 | N | B | 44 |
| 20130617 | 69203 | 30 | S | A | 41 |
| 20140428 | 73193 | 22 | W | A | 43 |
| 20140429 | 73213 | 35 | N | A | 44 |
| 20140430 | 73234 | 17 | S | A | 43 |
| 20140503 | 73300 | 25 | E | A | 43 |
| 20140504 | 73317 | 23 | W | A | 43 |
| 20140505 | 73335 | 25 | N | A | 44 |
| 20140506 | 73356 | 5 | S | A | 43 |
| 20140506 | 73357 | 24 | S | A | 43 |
| 20140507 | 73370 | 25 | E | B | 43 |
| 20140508 | 73390 | 25 | W | A | 43 |
| 20140509 | 73403 | 33 | N | A | 44 |
| 20140526 | 73607 | 28 | S | A | 39 |

Table 4.1 VERITAS observations of the LS 5039 region.

atmospheric variation and rated as "A" weather (as measured by the far-infrared sensors). The average elevation was 42.3° and all observations were made with all four telescopes. There were 7.9 hours of usable observations after quality cuts.

Standard reflected-region analysis was performed (Daniel, 2008) with background extracted from regions near the sources and from the same radial camera position. BDTs was used to perform medium cuts for gamma-hadron separation and a 0.35° radius region around LS 5039 and a 0.75° radius region around HESS J1825-137 were excluded from the background estimation. Two bright stars (m<7.0) were also excluded from the background estimation using 0.25° radius regions. The observations are outlined in Table 4.1 and a skymap of the region showing the significance in the entire region is in Figure 4.1. The distribution of significance in the non-source regions is consistent with a stochastic gamma-ray

background and the histogram of the significance distributions in the region is shown in Figure 4.2.

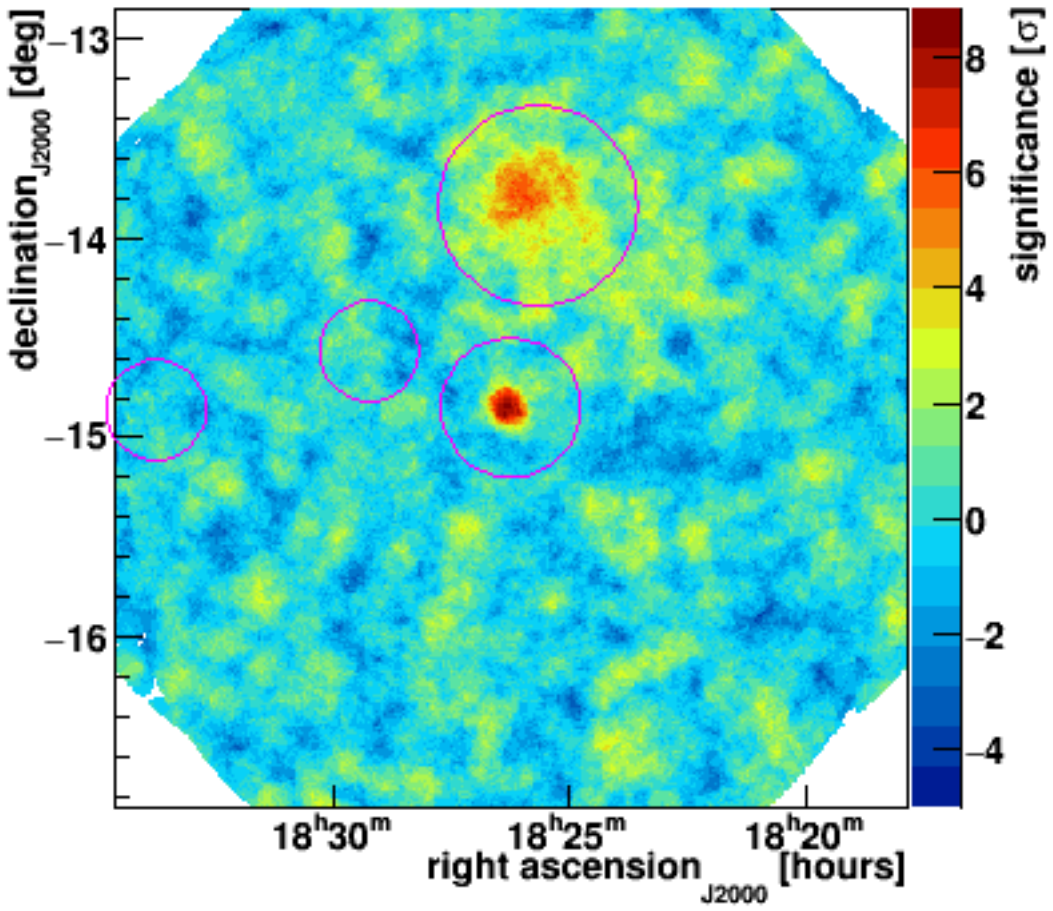


Figure 4.1 Significance map of the region around LS 5039. Significance is calculated using Li and Ma (1983). The red circles indicate background exclusion regions around the two sources of interest and two bright stars in the field of view. Significant excess is clearly visible as a point source at LS 5039 in the center of the image. The extended region of significant excess in the north is HESS J1825-137. The associated significance distribution of the source and background contributions is in Figure 4.2.

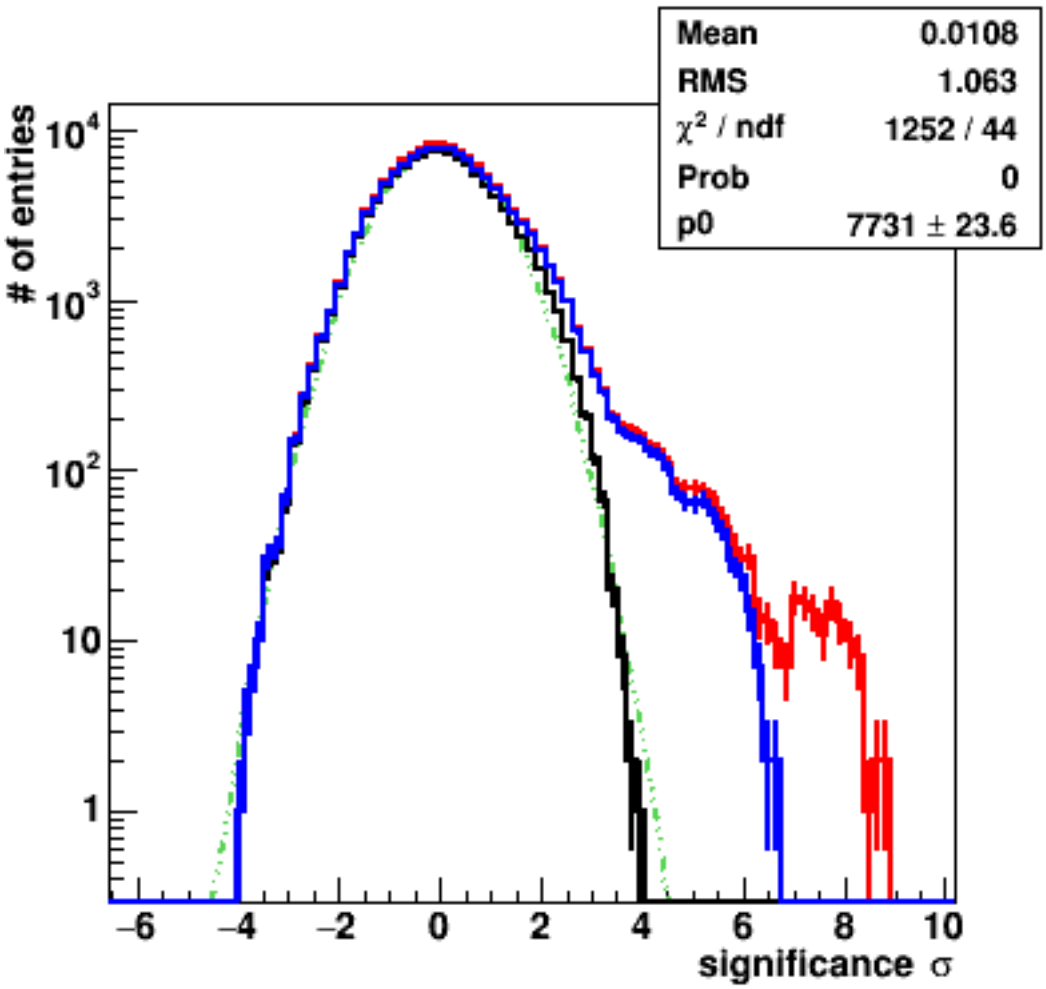


Figure 4.2 Significance distribution of the region around LS 5039. Each color line indicates a different significance distribution: red is from the entire map, blue excludes the central source exclusion region only (around LS 5039), black is the background regions, and green is a Gaussian distribution with the mean and rms in the legend (ideally, mean = 0 and rms = 1). The difference in area between the red and blue lines is the signal from LS 5039 and the difference between the blue and black lines is the signal from HESS J1825-137.

## 4.2 LS 5039

LS 5039 was identified as a high mass X-ray binary in the ROSAT Galactic plane survey (Motch et al., 1997) and radio emission was detected using the Very Large Array (Marti, Paredes, and Ribo, 1998). It was also detected as a gamma-ray binary with EGRET (Paredes et al., 2000). It was initially identified as the first gamma-ray

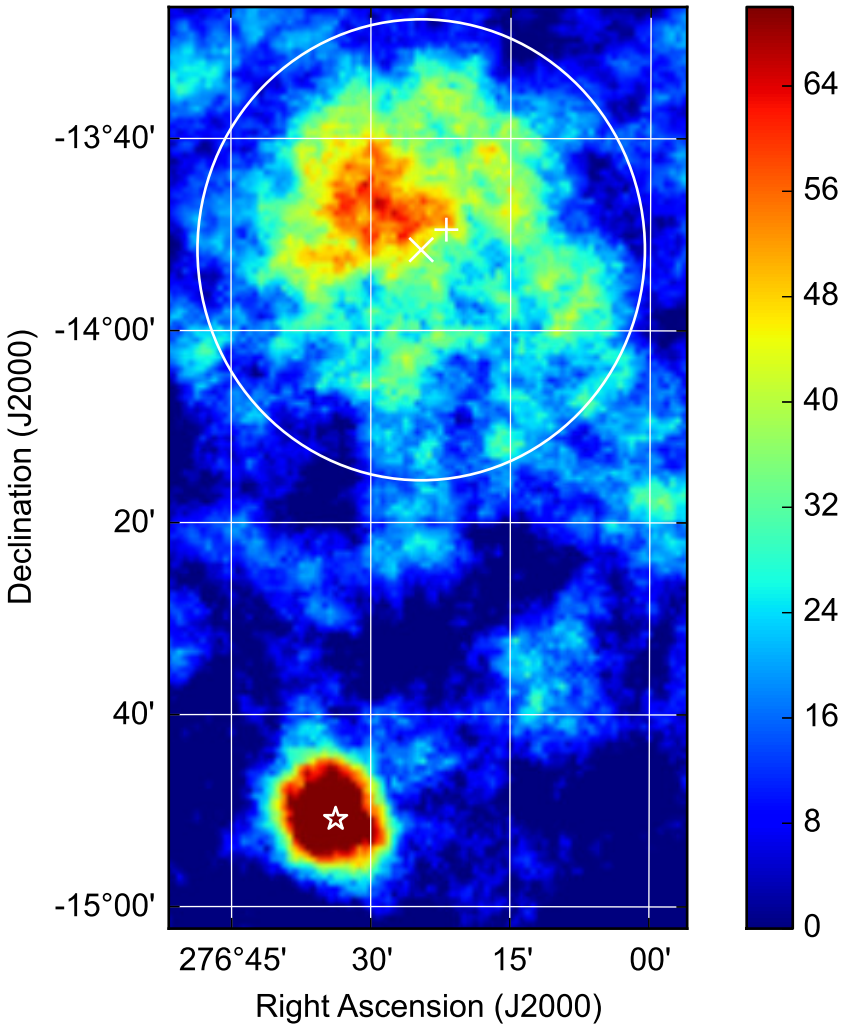


Figure 4.3 Excess map zoomed in on the region of LS 5039 and HESS J1825-137. The white star is the position of LS 5039 from Aharonian et al. (2006a) and the white circle is a radius of 0.4° around HESS J1825-137 from H. E. S. S. Collaboration et al. (2019). The white cross is the VERITAS centroid of HESS J1825-137.

emitting microquasar when initially detected by HESS (Aharonian et al., 2005a), but more recent analysis has cast significant doubt on this interpretation. The star is spectral type O6.5V (Clark et al., 2001), and the nature of the compact object is still considered to be undetermined without a detected pulsar and lack of orbital constraints to constrain the object's mass (Yamaguchi, Yano, and Gouda, 2018).

There is evidence of the high-energy emission being pulsar-powered based on the orbital phase difference between X-ray/TeV flux and the GeV flux. The spectral indicies and fluxes are almost entirely anti-phased (that is: GeV emission peaks opposite that of the X-ray and TeV emission). Further, the fairly low orbital eccentricity of the system ($e \sim 0.3$) provides some challenges to explaining the variation in emission by the change in accretion rate. Throughout the orbit, emission can be explained by a pulsar wind interacting with the star, but with some slight variations. Takata et al. (2014) are able to model the change in spectra by time averaging over two broad phases, roughly half-orbit each, defined by the orientation of the star-compact object system relative to the observer.

The model relies on two distinct shocks to accelerate particles: one between the pulsar and star and another caused by the motion of the pulsar which is oriented away from the star. The inner shock region is thought to be synchrotron dominated with a magnetic field strength modeled at about 15 G, while the outer shock is IC dominated with a magnetic field strength of about 0.5 G. The phase near inferior conjunction (INFC, where the compact object is in the foreground) is characterized by enhanced X-ray and TeV emission. The X-ray emission is mostly from the inner shock region due to synchrotron emission and the enhancement during INFC is from Doppler boosting in the stellar wind. At inferior conjunction the radial cometary tail from the stellar wind is at maximum relative to the observer which results in X-ray emission being amplified by a factor of 8 (Dubus, Cerutti, and Henri, 2010). The TeV emission is mostly from electrons that are accelerated in the shock away from the star, and the IC emission is enhanced when the observer is aligned with the electron wind. The interior shock contributes to the TeV emission, still, but the enhancement is from looking down the pipe (so to speak) of the outer pulsar wind. During superior conjunction (SUPC, where the star is in the foreground), enhanced GeV emission above that from the pulsar

magnetosphere is observed as the TeV gamma rays from the inner-shock interact with the material in the stellar atmosphere and produce a cascade of electrons and positrons which then IC scatter the ambient photons to GeV energies.

VERITAS detected LS 5039 at a significance of $8.8\sigma$ (Li and Ma, 1983) with 101 excess counts within a region of $\theta^2 = 0.008\,\mathrm{deg}^2$ centered at the known position from HESS $(\alpha, \delta) = (276.^\circ563, -14.^\circ848)$ (J2000) (Aharonian et al., 2006a). Each run is a single $\sim 20 - 30$ minute exposure, and consecutive exposures were separated by 1-2 nights. This provided approximately daily measurements of the already known 3.9 day orbital period (Aharonian et al., 2006a) for 8 days in 2013 and 12 days in 2014.

There is some evidence of variability from run to run in the VERITAS observations. To test for variability the run-wise data was fit to a constant rate. This was done by finding the n that minimizes equation 4.1 where $\bar{r}$ is the constant rate, $r_i$ is the run-wise rate, and $\sigma_i$ is the run-wise error on the rate.

$$\chi^2 = \Sigma \frac{(\bar{r} - r_i)^2}{\sigma_i^2} \tag{4.1}$$

The best fit of a constant rate is $n = 0.155\ \gamma\ /\mathrm{min}$ ($\chi^2/\mathrm{DoF} = 25.85/16$), excluding that hypothesis at a confidence of 0.055. The overall light curve best fit to a single rate is shown in figure 4.4. To determine the period of the object, ideally one would construct a periodogram with enough flux points. However, with limited data, and knowing the oscillation is roughly sinusoidal in nature, we can estimate the period by fitting a sine function. One season worth of data, with an fit to a sine function as an approximation, is shown in figure 4.5. The period of the functional fit in figure 4.5 is $T = 4.0 \pm 0.6$ days which is in agreement with the $3.9078 \pm 0.015$ day period determined by constructing a periodogram using gamma-ray flux (Aharonian et al., 2006a) and radial velocity measurements.

To provide more evidence of variability in the VERITAS data, the known orbital period can be used and difference in spectral parameters based on the phase can be constructed. Spectra separated by orbital phase, see Figure 4.6, agree with those measured with HESS (Aharonian et al., 2006a). The flux above 1 TeV is $(2.5 \pm 0.4_{stat} \pm 0.5_{sys}) \times 10^{-12}\,\mathrm{cm}^{-2}\,\mathrm{s}^{-1}$ near inferior conjunction (232 minutes exposure) and $(7.8 \pm 2.8_{stat} \pm 1.6_{sys}) \times 10^{-13}\,\mathrm{cm}^{-2}\,\mathrm{s}^{-1}$ near superior conjunction (230 minutes). This difference in flux demonstrates that the variability in the source is detected by VERITAS. Fitting a power-law to each orbital phase gives a photon index near inferior conjunction of $\Gamma = -2.1 \pm 0.2_{stat} \pm 0.2_{sys}$ with $\chi^2/\mathrm{DoF} = 0.19/1$ and $\Gamma = -2.4 \pm 0.5_{stat} \pm 0.2_{sys}$ with $\chi^2/\mathrm{DoF} = 0.57/1$ near superior conjunction. The VERITAS flux points match HESS with $\chi^2/\mathrm{DoF} = 2.78/2$ and $\chi^2/\mathrm{DoF} = 0.78/2$ for inferior and superior conjunction, respectively.

## 4.3 HESS J1825-137

The first indication of a pulsar wind nebula (PWN) in this field was detection using ROSAT observations of an extended ($\sim 5'$) X-ray nebula associated with the young (21 kyr) and energetic ($\dot{E} = 2.8 \times 10^{36}\,\mathrm{erg\,s}^{-1}$) pulsar PSR B1823-13 which is at a distance of 4.12 kpc (Finley, Srinivasan, and Park, 1996). HESS J1825-137 is larger than the X-ray nebula, but the larger extent is consistent with the longer lifetime of TeV emitting electrons (Aharonian et al., 2005b). There is a region of molecular gas with enhanced turbulence that indicates a possibly associated SNR at the correct distance, however, the nature of that turbulence has not been determined (Voisin et al., 2016)

Using the same observations and analysis described for LS 5039, VERITAS detected HESS J1825-137 at the center of the PWN reported by HESS $(\alpha, \delta)$ (J2000) $= (276.421^\circ, -13.839^\circ)$ (H. E. S. S. Collaboration et al., 2019) with a significance

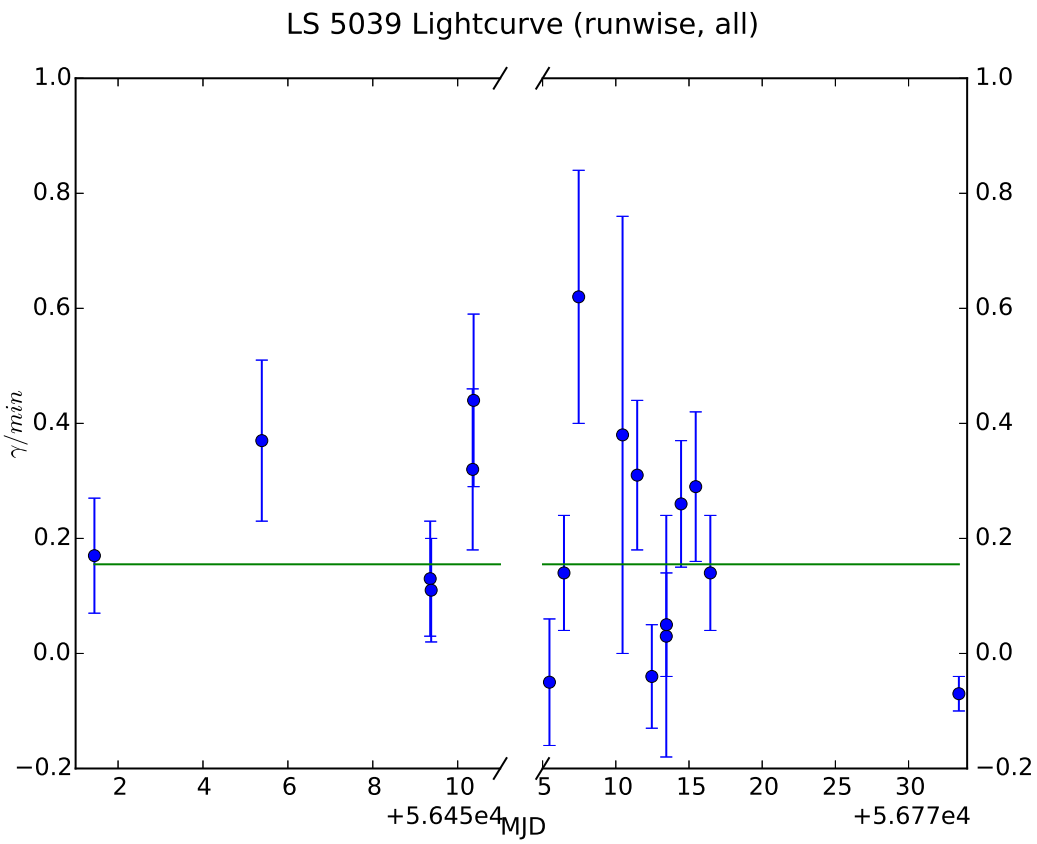


Figure 4.4 Light curve of all VERITAS observations. Green line is the best fit to a constant flux.

of $5.3\sigma$; the peak significance of $6.7\sigma$ is within $2'$ of this position. Fitting a spectrum extracted from a $0.4^\circ$ radius source region to a simple power law model gave a normalization at 1 TeV of $A = (5.0 \pm 0.7_{stat} \pm 1.0_{sys}) \times 10^{-12}\,\mathrm{cm}^{-2}\,\mathrm{s}^{-1}\,\mathrm{TeV}^{-1}$, a photon index $\Gamma = -2.28 \pm 0.15_{stat} \pm 0.2_{sys}$, and $\chi^2/\mathrm{DoF} = 2.27/1$ (flux above 1 TeV of $(3.9 \pm 0.8) \times 10^{-12}\,\mathrm{cm}^{-2}\,\mathrm{s}^{-1}$). We found the PWN to be centered at $(\alpha,\ \delta) = (276.37^\circ \pm 0.02^\circ_{stat} \pm 0.01^\circ_{sys}, -13.83^\circ \pm 0.02^\circ_{stat} \pm 0.01^\circ_{sys})$ (J2000). Summing in azimuth around the PWN, the radial profile is well modeled by by a Gaussian with $\sigma = 0.27^\circ$ $(1\sigma\ \mathrm{CI}:\ 0.22^\circ - 0.44^\circ)$ $(\chi^2/\mathrm{DoF} = 3.64/3)$. The radial profile and best fit are shown in Figure 4.7.

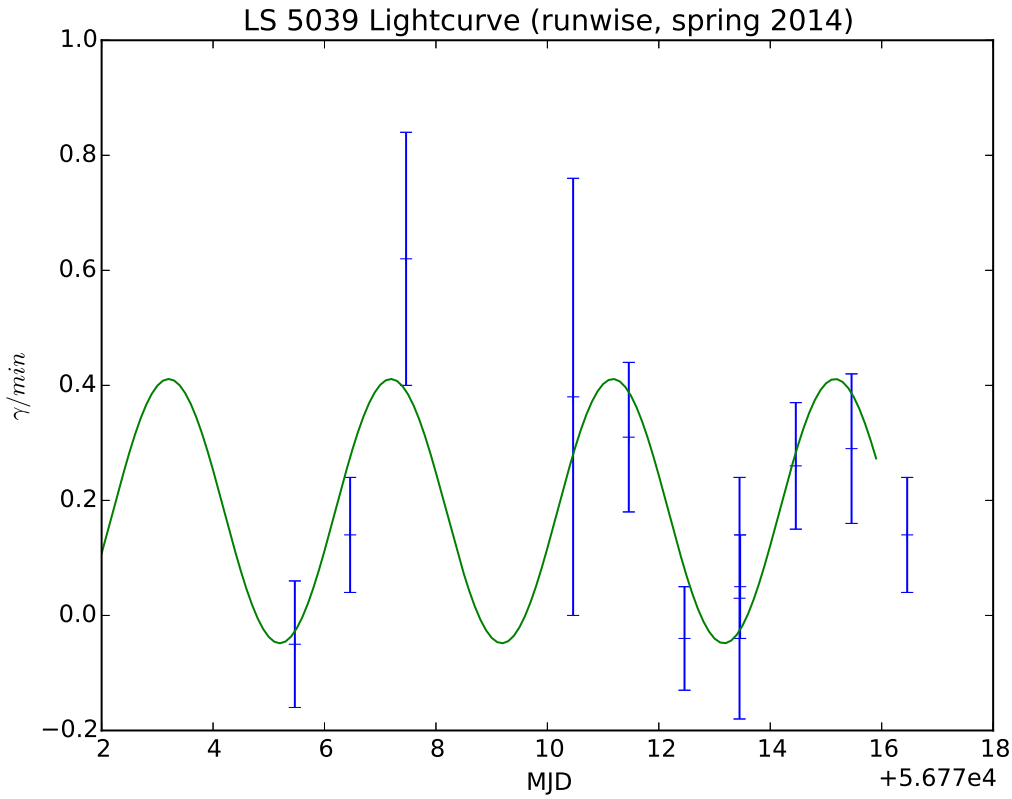


Figure 4.5 Light curve of one the 2014 VERITAS observations with a best fit sine function indicating the periodicity

Using a $0.4^\circ$ radius for the source, HESS reports a power-law fit of $A = (6.81 \pm 0.07_{stat} \pm 0.2_{sys}) \times 10^{-12}\,\mathrm{cm}^{-2}\,\mathrm{s}^{-1}\,\mathrm{TeV}^{-1}$ with a photon index $\Gamma = -2.28 \pm 0.01_{stat} \pm 0.02_{sys}$ (H. E. S. S. Collaboration et al., 2019). Including a 15-20% systematic error the VERITAS flux normalization brings the measurement in line statistically with HESS. Similarly, the position of the PWN measured with VERITAS is within $0.04^\circ$ of that detected by HESS, comparable to the $0.1^\circ$ PSF of each instrument. The radial extent of the nebula measured by VERITAS is consistent with the original HESS observations of $\sigma = 0.24^\circ \pm 0.02^\circ$ with a shorter 52hr exposure (Aharonian et al., 2006b), but the exceptionally deep observations from H. E. S. S. Collaboration

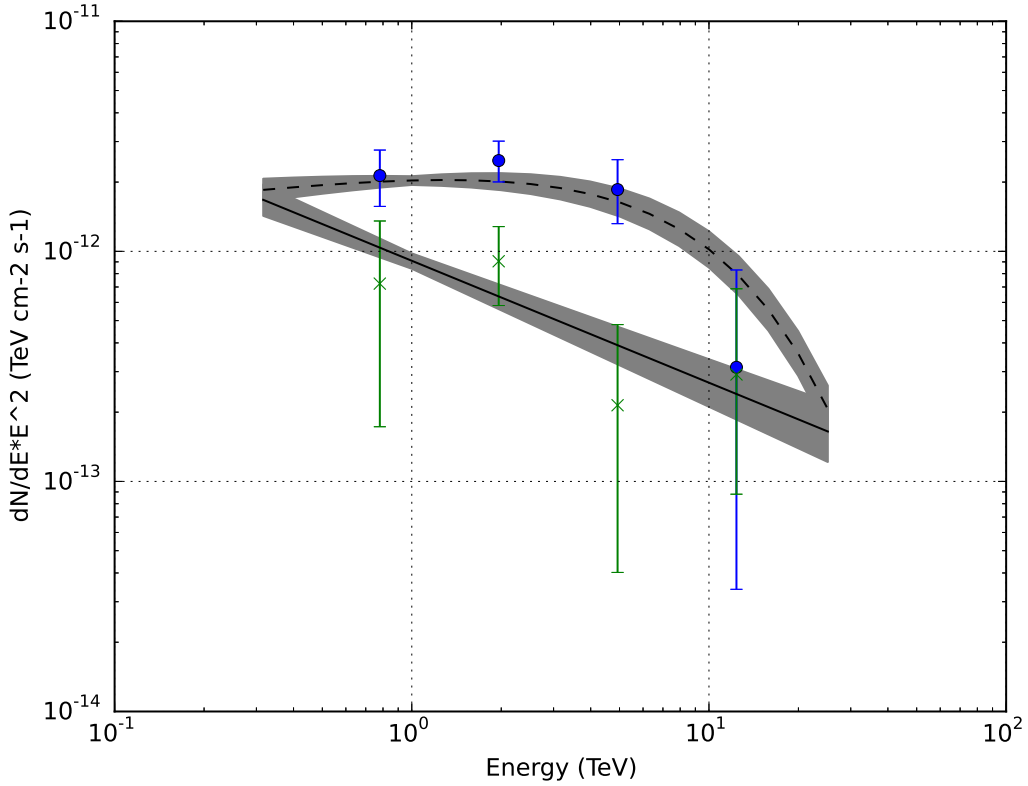


Figure 4.6 Energy distribution of the emission from LS 5039. Solid line and x are from the low state of LS 5039. Dashed line and circles are from the high state of LS 5039. The fit lines (and associated shaded errors) are from (Aharonian et al., 2006a).

et al. (2019) reports a different, generally larger, energy dependent extent ranging from $0.14^\circ \pm 0.1^\circ$ at E > 32 TeV to $0.76^\circ \pm 0.02^\circ$ between 250 GeV – 500 GeV.

Using the estimated distance to the pulsar of 4 kpc, the nebula is thought to be nearly 100 pc in diameter and the largest known TeV PWN (H. E. S. S. Collaboration et al., 2019). The nebula as a whole exhibits a typical inverse-Compton scattering spectral signature with significant photon seed populations from the cosmic microwave background and a far infrared (dust) component. Models using energy-dependent high resolution maps indicate that advection is the dominant energy transport in the nebula, indicating that the PWN still maintains pressure

against the ISM. Each component of this PWN is prototypical and it will certainly be studied with more detail in the next several years when CTA comes online.

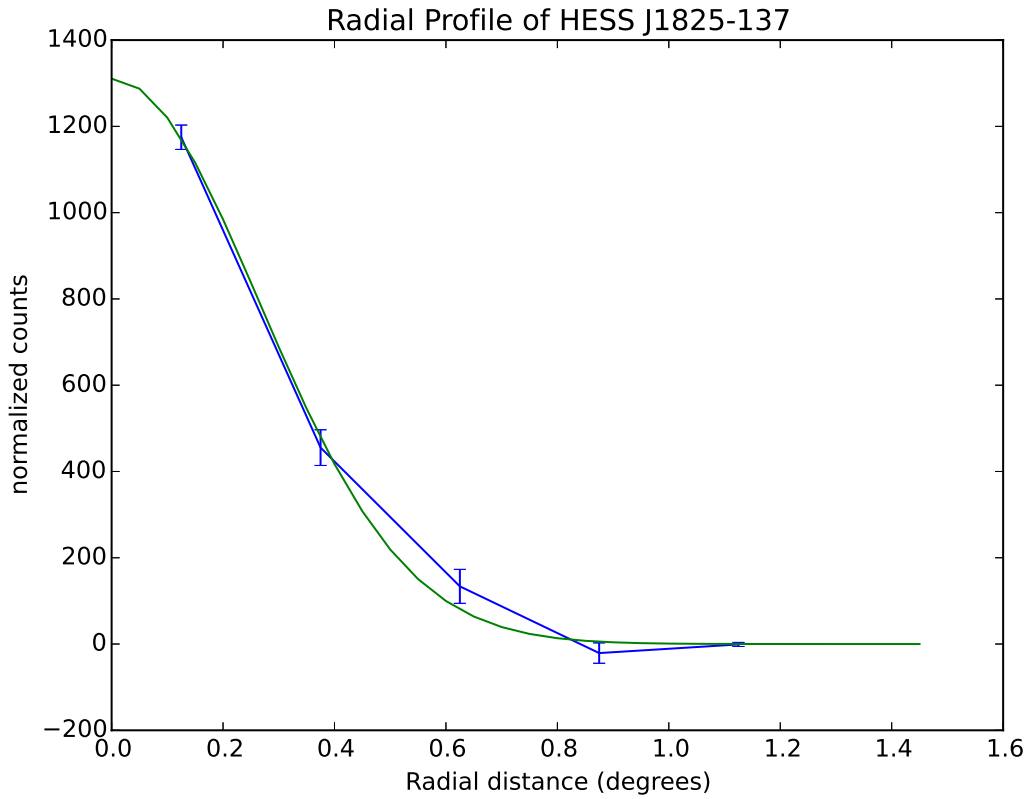


Figure 4.7 Radial profile of HESS J1825-137. The blue points are the samples from the skymap, and the green line is the best fit profile.

## 4.4 Discussion

At a distance of $d = 4.12$ kpc, the luminosity of HESS J1825-137 is $L_{1-10\ \mathrm{TeV}} = (7.9 \pm 2.2) \times 10^{33}$ erg s$^{-1}$. Using a baseline evolutionary model for PWN, where one expects TeV luminosity to decrease with age, it should be about about 22kyr old (H.E.S.S. Collaboration et al., 2018). There is also timing information about the pulsar, PSR B1823-13 which helps to isolate the power source with in the nebula: $P = 0.101\ s$, $\dot{P} = 7.5 \times 10^{-14}$, $\dot{E} = 2.8\ \times 10^{36}\,\mathrm{ergs\,s^{-1}}$, and $\tau_c = 21$ kyr (Manchester

et al., 2005). In this case, the estimated age and pulsar parameters from the TeV luminosity line up with the observed pulsar parameters - with one exception. The size of the nebula in the baseline model is only expected to be about $R_{\rm PWN} \approx 12$ pc, while HESS J1825-137 is measured at greater than $R_{\rm PWN} \approx 18$ pc using VERITAS's $1\sigma$ extent of 0.24°radius (and HESS's most sensitive measurements puts $R_{\rm PWN} \approx$ 50 pc). These differences can be simply explained by a thinner than typical ISM density which allows for the expansion of the PWN to progress without a typical outside pressure.

The distance to LS 5039 is $d = 2.9 \pm 0.8$ kpc (Yamaguchi, Yano, and Gouda, 2018) and at $d = 2.5$ kpc the gamma-ray luminosity measured by VERITAS is $L_{1-10\ \rm TeV} = (9.3 \pm 5.4) \times 10^{32}$ erg s$^{-1}$. LS 5039 is unresolved by VERITAS, however the variability of about 3.9 days constrains the nebula to having an emission region with radius no larger than 300 AU (compared to the 0.1-0.2 AU orbital distance). The TeV emission seems to be unexpectedly suppressed in LS 5039 compared to other pulsar-powered binary systems and the modeling done by Takata et al. (2014) over estimates very high energy gamma-ray emission when accounting for the star's presence (though, the scale of the modulations are close to that observed). Bednarek and Sitarek (2013) suggests that material from the star can act as a mediator in binaries like LS 5039 which lowers the IC scattering efficiency of the pulsar wind since some of the electron energy is transferred to ions in the mixed material and they have applied that model to other gamma-ray binaries. When compared the gamma-ray binaries with known pulsar properties PSR B1259-63/LS 2883 (Chen et al., 2019) and PSR J2032+4127 (Bednarek, Banasiński, and Sitarek, 2018; Abeysekara et al., 2018a), LS 5039 has a very short orbial period of 4 days (compared with about 4 years and 50 years for B1259 and J2032, respectively). This regular, relatively short, period makes it a regular source of interest to test pulsar-star interaction models, however it also makes it more com-

plex since neither object in the binary system are seen in isolation as they are in the long-period binaries.

Both of the objects in the field of view tell different stories of pulsar evolution and how the spindown of the pulsar injects power into its surroundings. LS 5039 has been constantly interacting with a companion star for its entire life and has not developed as bright of an extended nebula that it might have if the pulsar was isolated. The normal PWN evolutionary model does not apply in this case. This is in stark contrast to HESS J1825-137 where the nebula was likely allowed to more freely expand into a rarefied medium, and knowing the pulsar properties vindicates the baseline as a close match to the evolution of the extended PWN.

# CHAPTER 5

## PWN DA 495 (2HWC J1953+294)

This chapter is two parts related to the study of pulsar wind nebula DA 495. First, background of the discovery of DA 495 in TeV gamma rays and VERITAS analysis is detailed in Section 5.1. The results of this analysis were originally reported on in Abeysekara et al. (2018b) as part of a follow-up study on new TeV gamma-ray sources detected by HAWC, and the strong magnetic fields measured by study of the radio spectrum made the TeV detection unexpected (Kothes et al., 2008). Second, starting with Section 5.2, the entire text of a paper accepted for publication in the Astrophysical Journal, titled: "Multiwavelength Study of Pulsar Wind Nebula DA 495 with *NuSTAR*, *VERITAS* and *HAWC*," is included (Coerver et al., 2019).

## 5.1 Background

2HWC J1953+294 was discovered by HAWC as a point source as part of their 2HWC catalog published in 2017, which is the result of 507 days of observations (Abeysekara et al., 2017b). The source was detected at $\alpha, \delta$ (J2000) $= 298.26^\circ, 29.48^\circ$ ($l, b = 65.86^\circ, 1.07^\circ$) with a $1\sigma$ uncertainty of $0.24^\circ$. The 2HWC centroid is $0.2^\circ$ from the radio position of DA 495 (SNR G65.7+1.2). The larger than typical pointing uncertainty could have been due to the lower signal (statistical significance $\sigma$ can be related to HAWC's test statistic by $\sqrt{TS} = \sigma$, and J1953 was detected with a TS=30.1 or $\sigma = 5.5$) or some moderate extension that was not large enough to be detected by the extended source searches. This was one of the 2HWC sources near the Galactic plane that was furthest from any known TeV source at the time ($8.44^\circ$). The spectral index at 7 TeV is $\Gamma = 2.78 \pm 0.15$, similar to SNR G054.1+00.3 (2HWC

J1930+188, $\Gamma = 2.74 \pm 0.12$) - which is thought to host a young pulsar and bears some resemblance to DA 495 in other wavelengths.

Within about 1° of 2HWC J1953+294 is 2HWC J1955+285, another previously-unknown TeV source. It is possibly associated with the SNR G065.1+00.6 which has been detected in lower-energy gamma rays. In addition to these two sources, there is some diffuse emission in the sky region that bridges the two sources. The skymap of the region showing both sources is shown in Figure 5.1.

### 5.1.1 VERITAS Observations

VERITAS reported a confirmation of weak gamma-ray emission ($5.2\sigma$ pre-trials statistical significance) coincident with 2HWC J1953+294 after 37 hours of observation (Holder, 2017). The initial detection included about 14 hr of observations of PSR J1958+2846 from 2012-2014 that were centered within 1.5° of the HAWC position.

The weak signal prompted additional followup in 2016 and 2017. The average elevation was 71° and observations were made with a 0.7° wobble around the HAWC source given the position uncertainty and possible extension. VERITAS observed 2HWC J1953+294 for a total of 68.5 hours. A summary of the observations is shown in Table 5.1.

| Season | Target | Total Exposure *hrs* |
|---|---|---|
| 2012-2013 | FGL J1954+2836-FGL J1958+2846 Mid Point | 10.6 |
| 2013-2014 | PSR J1958+2846 | 18.0 |
| 2015-2016 | 2HWC J1953+294 | 33.5 |
| 2016-2017 | 2HWC J1953+294 | 35.0 |

Table 5.1 Summary of VERITAS observations near 2HWC J1953+294. The total exposure is before quality cuts.

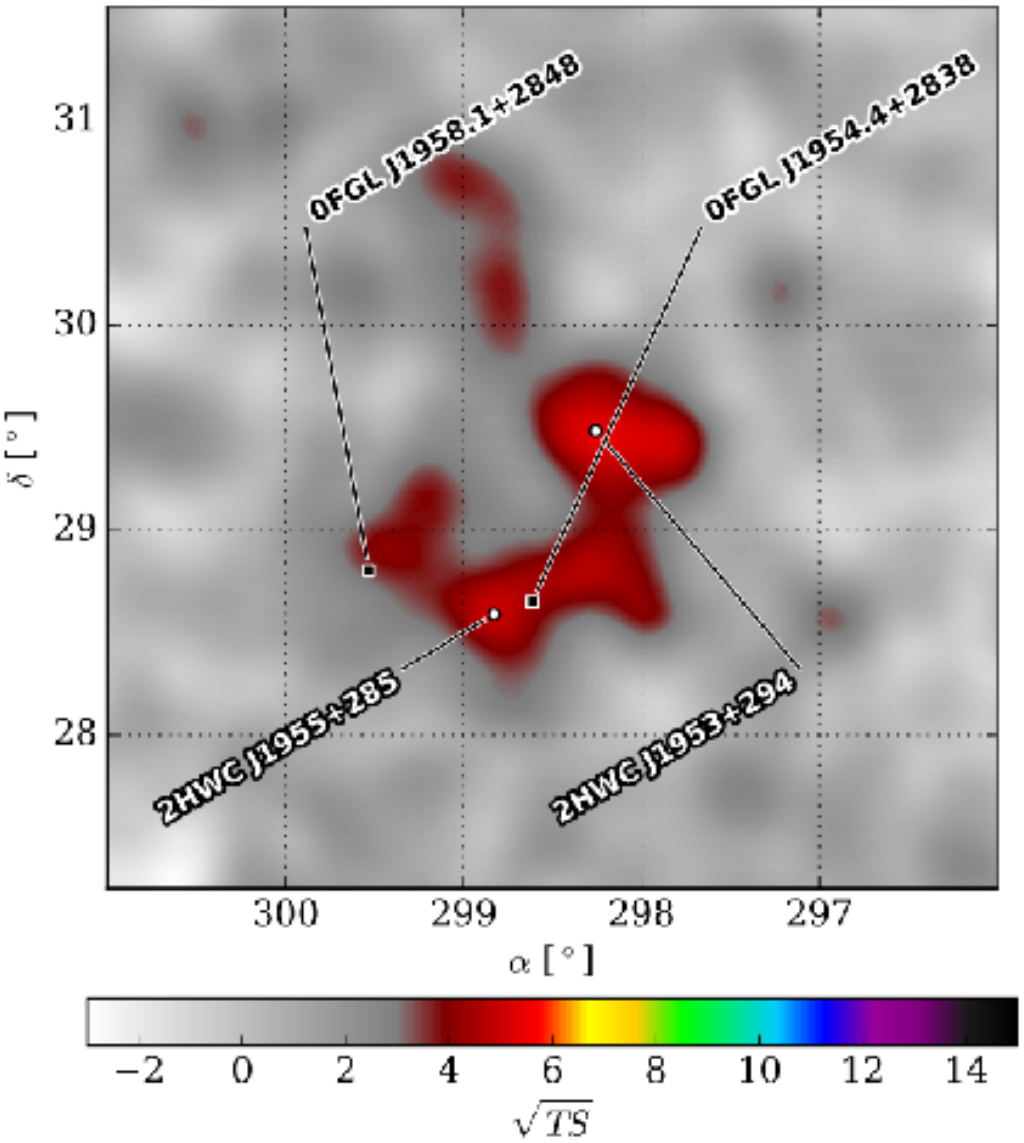


Figure 5.1 HAWC significance skymap of the region containing DA 495 as in Abeysekara et al. (2017b). The image was obtained from the 2HWC online data catalog.

### 5.1.2 VERITAS Analysis

After cutting the runs for bad weather or instrument issues, there is about 72 hrs of usable data from VERITAS (including about 10 hours usable from near by PSR J1958+2846). An extended source analysis was used ($\theta < 0.3^\circ$). Gamma-hadron separation was made using boosted decision trees with hard cuts (Krause, Pueschel, and Maier, 2017). Regions of $0.3^\circ$ radius around both of the *Fermi* pulsars and 2HWC J1955+285 were excluded from background estimation. A $0.34^\circ$ radius region was excluded around 2HWC J1953+294 to account for the size of the radio nebula. We found 953 ON counts and 11120 OFF counts ($\alpha = 0.069$) within $0.3^\circ$of the position of maximum significance (using a search radius around the HAWC position of $0.4^\circ$). This resulted in 188.3 excess counts and maximum significance of $6.3\sigma$ pretrials. Since we had to test multiple positions, a trials factor had to be accounted for. A $0.4^\circ$ radius search region with $0.04^\circ \times 0.04^\circ$ tiles is 315 trials. The source was detected at a post-trials significance of $5.2\sigma$ (Abeysekara et al., 2018b). The VERITAS significance skymap of the region is shown in Figure 5.2 with the associated 1D significance distribution shown in Figure 5.3. The 1D distribution is acceptable. An annotated excess map with radio and X-ray contours is shown as part of the paper included in this chapter in Figure 5.4.

Morphology and localization were determined using a 2D Gaussian. The centroid was found to be $\alpha,\ \delta\ (\mathrm{J2000}) = 298.06^\circ \pm 0.04^\circ{}_{\mathrm{stat}} \pm 0.01^\circ{}_{\mathrm{sys}},\ 29.39^\circ \pm 0.02^\circ{}_{\mathrm{stat}} \pm 0.01^\circ{}_{\mathrm{sys}}$ with a $1\sigma$ extension of $0.14^\circ \pm 0.02^\circ$. Thus, the gamma-ray source detected by VERITAS is named VER J1952+294.

The spectrum measured by VERITAS is well described by a power-law distribution ($\frac{\mathrm{dN}}{\mathrm{dE}} = \mathrm{A} * (\mathrm{E}/1\ \mathrm{TeV})^{\ -\Gamma}$) with an index of $\Gamma = 2.65 \pm 0.45_{\mathrm{stat}} \pm 0.2_{\mathrm{sys}}$ and a flux normalization at 1 TeV of $(2.84 \pm 0.54_{\mathrm{stat}} \pm 0.56_{\mathrm{sys}}) \times 10^{-13}\ \mathrm{cm}^{-2}\ \mathrm{s}^{-1}\ \mathrm{TeV}^{-1}$. Extrapolating the HAWC measurement for the region to 1 TeV gives a normal-

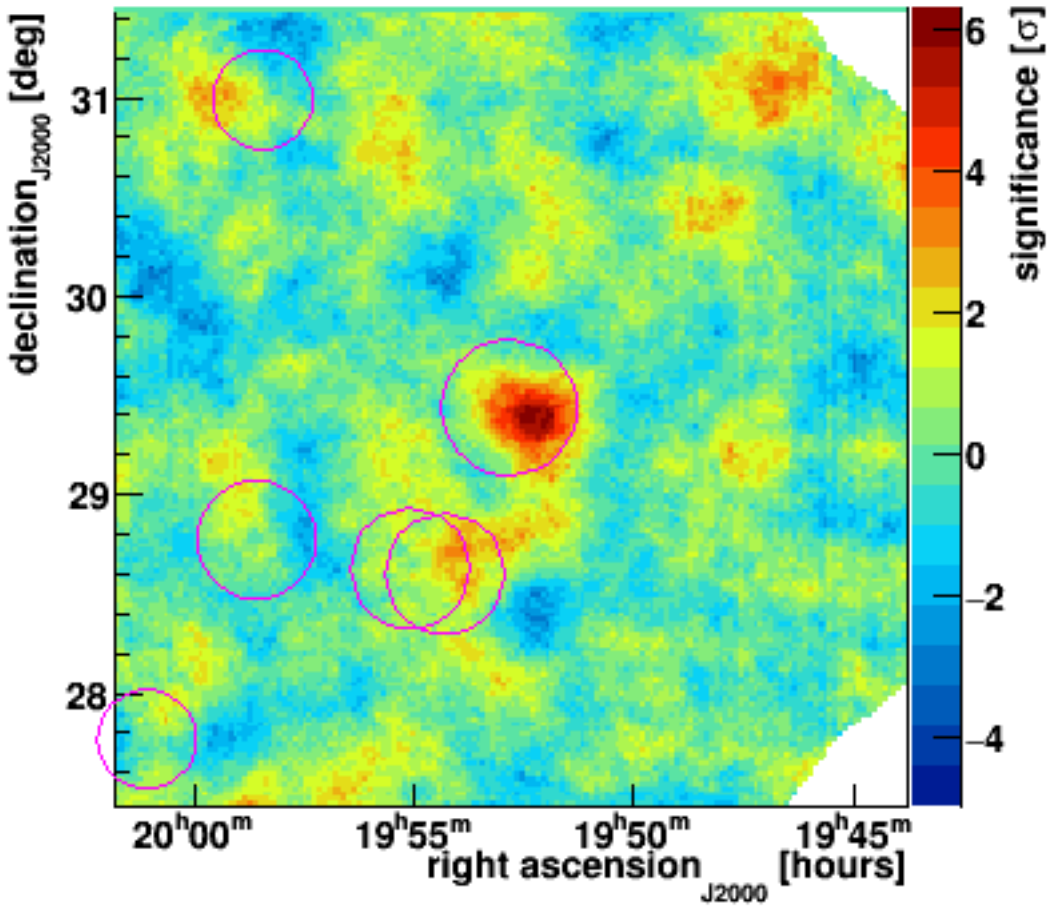


Figure 5.2 VERITAS significance map of DA 495 region. The 1D significance distribution for this region is shown in Figure 5.3.

ization of $1.86 \times 10^{-13}$ cm$^{-2}$ s$^{-1}$ TeV$^{-1}$ and is about 7x the flux of the VERITAS measurement. This discrepancy may be due to source confusion in the region and future HAWC analysis with multiple source fitting should help. The VERITAS analysis is a pointed observation, and less likely to suffer from the contamination of nearby sources, so the VERITAS spectrum is adopted for the multiwavelength analysis in the following sections.

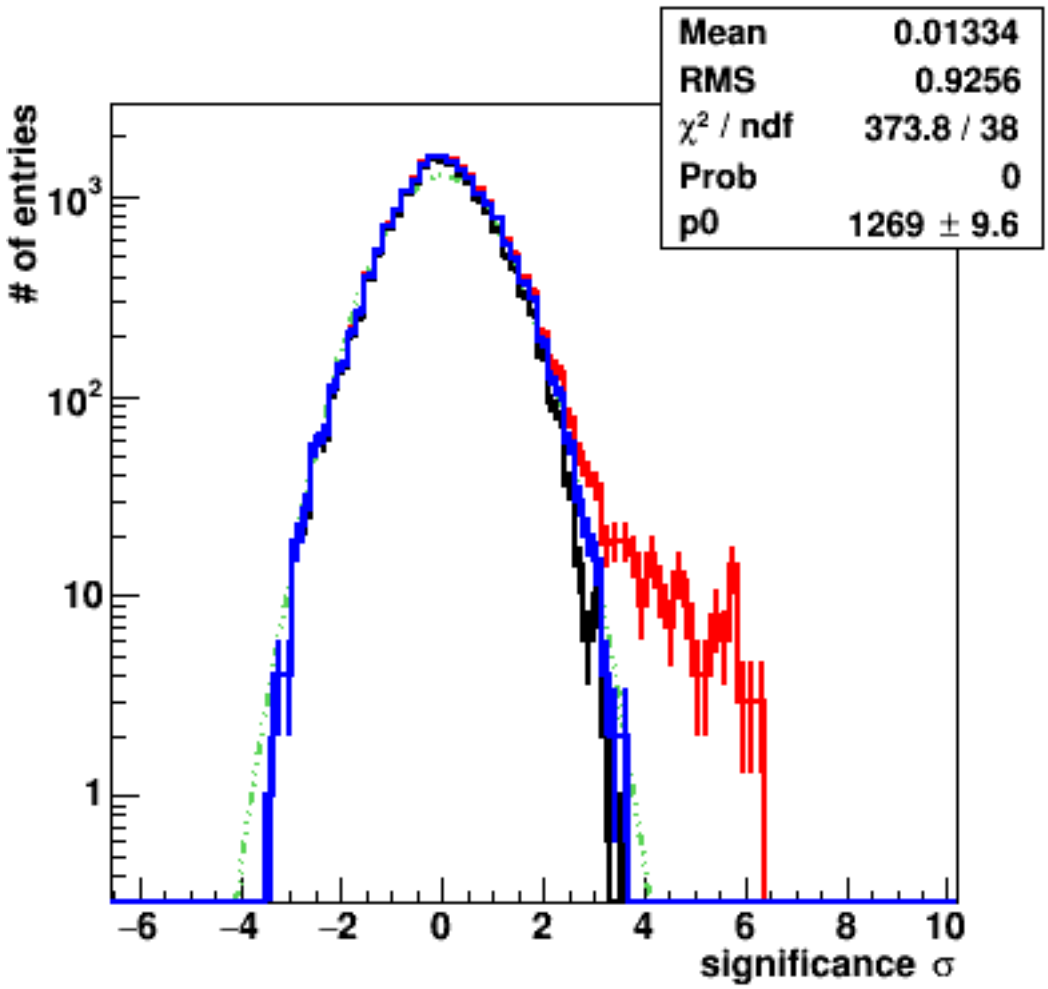


Figure 5.3 Significance distributions of the VERITAS skymap shown in Figure 5.2. Each color line indicates a different significance distribution: red is from the entire map, blue excludes the central source exclusion region only, black is all background regions, and green is a Gaussian distribution with the mean and rms in the legend (ideally, mean = 0 and rms = 1). The difference between the red and black lines indicate the signal from the source.

## 5.2 Introduction

When a massive star ($> 8\ M_{\odot}$) explodes in a core collapse supernova, much of its angular momentum remains with the newly created neutron star (pulsar). This pulsar can produce an expanding bubble of highly relativistic wind, called the pulsar wind nebula (PWN), and forms a termination shock. The observation of

synchrotron and inverse Compton emission within the PWN suggest the acceleration of nonthermal particles. The pulsar may continue to feed the PWN with its rotational energy and expand the boundary of the nebula. For a review of PWNe see Gaensler and Slane (2006).

The most well studied (and thought to be representative) PWNe are the young Crab and older Vela-X nebulae with ages of about 1,000 years and 20,000 years, respectively (Hester, 2008; Kargaltsev et al., 2015). Vela-X is notably more evolved with its very extended filamentary structure within the PWN and apparent expanding supernova remnant (SNR) shell seen to interact with the local interstellar medium (ISM). This shell, evidence of an advancing shock formed by the progenitor supernova, is thus far absent from observations of the Crab Nebula (Yang and Chevalier, 2015). Both the Crab and Vela-X PWNe have well studied pulsars (PSR B0531+21 and PSR B0833-45, respectively) which allow the broadband emission to be modeled and measured within the context of the pulsar-nebula system (Seward and Wang, 1988; Bühler and Giomi, 2016). Studies of the Crab have indicated Lorentz factors of electrons reaching $\gamma \approx 10^6$ (Fraschetti and Pohl, 2017), emphasizing the importance of PWNe as astrophysical laboratories for relativistic processes. This is particularly important when considering the contribution of nearby PWNe to the cosmic ray positron population (Archer et al., 2018; Grasso et al., 2009).

Much of our knowledge about PWN evolution comes from comparing these two objects, however more detail about evolutionary processes is clearly necessary, as environmental and progenitor characteristics play key roles in the development of PWNe. Since not all PWN have age and pulsar characteristics available or as much environmental context as the Vela-X nebula, we must rely on spectral modeling and analysis of energy-dependent morphology to explain the conditions of these astrophysical laboratories and try to place them within an evolutionary context of other well-studied PWN.

In this study we present results from multiwavelength modeling of PWN DA 495 and evaluate its energy dependent morphology using new observations from *NuSTAR*. It is thought that DA 495 is in an evolutionary state somewhere between the Crab and Vela-X PWNe (Kothes et al., 2008), making it a good candidate for investigation of PWNe life cycles. In section 5.3 we discuss the observational history of DA 495, including: radio observations, X-ray observations, and recent very high energy gamma-ray observations not used in past modeling studies. Section 5.4 details the new *NuSTAR* observations that are analyzed and reported on in Section 5.5. Section 5.6 describes models and derived parameters used to evaluate the nebula, and Section 5.7 discusses implications of the modeling results.

## 5.3 Background/Previous Observations

### 5.3.1 Discovery and identification

DA 495 (G65.7+1.2) was discovered by the Dominion Astrophysical (DA) survey (Galt and Kennedy, 1968). It was identified as a point source in the DA survey due to the coarse angular resolution but there was insufficient signal to determine any spectral information at the time. Follow up as part of a supernova remnant search, performed with the National Radio Astronomy Observatory (NRAO) and the Vermilion River observatory, found that DA 495 had an extended structure and a non-thermal spectrum suggestive of a Crab-like SNR (Willis, 1973, and erratum). Further confirmation of the center-filled SNR hypothesis came with additional Dominion Radio Astrophysical Observatory (DRAO) observations (Landecker and Caswell, 1983). We now know these center-filled SNRs to be PWNe, and DA 495 has been studied as such since then, however an associated pulsation has not been

found. More recent results from observations in radio and other wavelengths are detailed in the next sections.

### 5.3.2 Radio

The most recent radio analysis of DA 495 is reported in Kothes et al. (2008), hereafter referred to as K08. The maps generated by K08 from observations done with the Canadian Galactic Plane Survey in 408 MHz and 1420 MHz (Taylor et al., 2003) and the Effelsberg Radio Telescope in 4850 MHz and 10550 MHz show an approximately circular diffuse source of about 25′ in diameter. That size is fairly consistent across the radio spectrum reported in K08 and is consistent with earlier observations, but the nebula is not present in IRAS 60 ¯m observations. Fractional polarization is about 25% at higher frequencies (2695 MHz, 4850 MHz and 10550 MHz) and is ordered in a way that indicates a central dipole magnetic field with a superimposed toroidal component. The magnetic field of the nebula, measured from a synchrotron cooling break at 1.3 Ghz, was determined to be extremely high at $B = 1.3$ mG. Using HI absorption and kinematic measurements relating to galactic rotation, K08 also estimated a distance to the source of $d = 1.0 \pm 0.4$ kpc. We adopt the radio fluxes reported in K08, which have compact sources and the foreground H II region removed for use with our combied spectrum described in Section 5.6. A map of radio emission at 1.4 GHz from the Canadian Galactic Plane Survey (CGPS) is shown as contours in Figure 5.4.

### 5.3.3 X-ray

DA 495 was first detected in the X-ray band in March 2004 using archival *ROSAT* and *ASCA* data (Arzoumanian et al., 2004). *ROSAT* source 1WGA J1952.2+2925, a faint, compact X-ray source, was assumed to be associated with the surrounding

radio nebula. The X-ray flux was found to be non-variable, non-thermal, and extended, leading to its identification as emission from a wind nebula. DA 495 was followed up with *Chandra* in 2007 (Arzoumanian et al., 2008), which was able to resolve a central point source inside the ~40" diameter (0.2 parsec at a distance of 1 kpc) X-ray nebula. *Chandra* spectral analysis of the extended emission resulted in a photon index of $\Gamma = 1.6 \pm 0.3$, allowing for confirmation of the extended region as a wind nebula. The central point source was found to have a purely thermal spectrum, a result confirmed by Karpova et al., 2015 (hereafter K15). K15 jointly fit the archival *XMM-Newton* and *Chandra* data with an absorbed powerlaw plus blackbody model and an absorbed powerlaw plus neutron star atmosphere model (NSMAX) (Mori and Ho, 2007; Ho, Potekhin, and Chabrier, 2008) to characterize the point source emission. The blackbody fit, likely modeling emission from a polar cap, resulted in a temperature of $T \approx 0.22$ keV, a radius of $R \approx 0.6$ km, and a neutral hydrogen column density of $N_H \approx 2.6 \times 10^{21}$ cm$^{-2}$. The NSMAX fit, modeling emission from the entire neutron star surface, resulted in a temperature of $T \approx 0.08$ keV, a radius of $R \approx 10$ km, and a neutral hydrogen column density of $N_H \approx 3.5 \times 10^{21}$ cm$^{-2}$. Neither model was ruled out. No pulsations were detected in the *Chandra* data, but the pure thermal spectrum of the point source implies its likely identification as the neutron star powering the wind nebula. K15 further constrained the pulsation non-detection through timing analysis of the *XMM-Newton* data, setting the upper limit for a pulsed fraction of 40 percent in a range of $\geq 12.5$ ms. K15 estimated the distance to the putative neutron star to be ~2.4 - 3.3 kpc (depending on which spectral models were applied to the point source spectrum) using the $N_H - D$ relation.

### 5.3.4 Gamma ray

The first TeV gamma-ray detection in the region of DA 495 was reported by the High Altitude Water Cherenkov Telescope (HAWC), which detected the source 2HWC J1953+294 within 0.2° of the radio center reported by K08 (Abeysekara et al., 2017b). Given the 25′ diameter radio size of DA 495 and HAWC's localization uncertainty of 0.1° it is certainly plausible that DA 495 is associated with 2HWC J1953+294 by position alone. Additional evidence that 2HWC J1953+294 is associated with DA 495 is the photon index at 7 TeV of $\Gamma = 2.78 \pm 0.15$, which is consistent with other PWNe in this energy range (such as the Crab). The TeV gamma-ray detection of DA 495 was confirmed by follow-up observations with the Very Energetic Radiation Imaging Telescope Array System (VERITAS), which detected VER J1952+293 (Abeysekara et al., 2018b). VER J1952+293 is centered within 0.05° of the radio center and has a extension defined by a 2D Gaussian with $\sigma = 0.14^\circ \pm 0.02^\circ$, which is consistent with the size of the radio nebula. The extent and position of the emission detected by VERITAS provides compelling evidence that the TeV and radio nebula are associated. The photon index measured by VERITAS at 1 TeV, $\Gamma = 2.65 \pm 0.49$, also agrees well with the TeV PWN interpretation.

There is significant disagreement between the VERITAS and HAWC flux measurements of their respective sources. At 1 TeV, HAWC has a flux that is about 7× higher than that of VERITAS (Abeysekara et al., 2018b) and is probably attributed to a nearby extended source and/or diffuse emission that contaminate the flux reported for 2HWC J1953+294. For this study, we adopt the VERITAS flux points and accept the HAWC measurement as an upper limit.

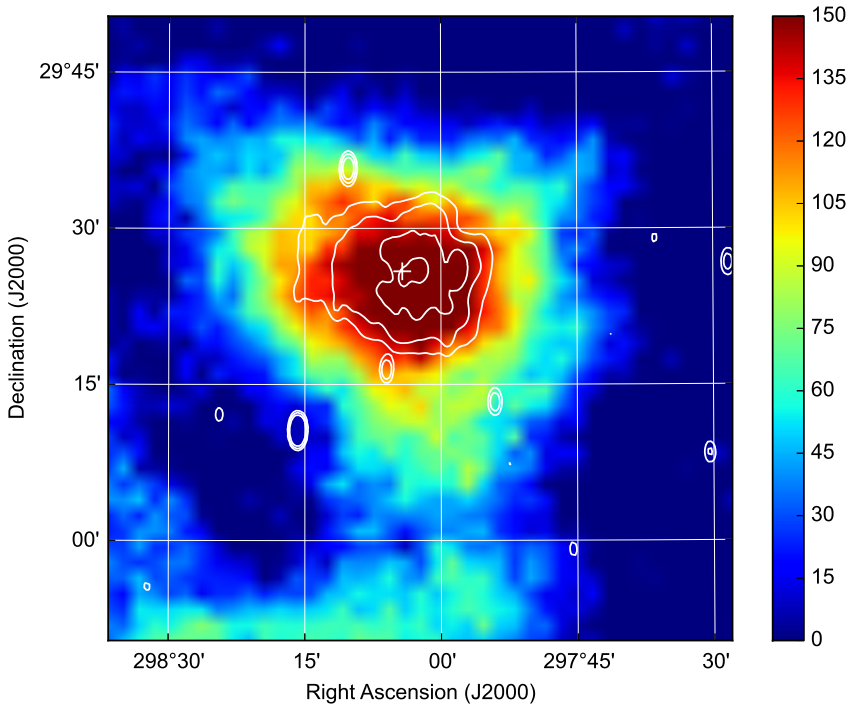


Figure 5.4 The color image is VERITAS excess $> 200$ GeV from Abeysekara et al. (2018b) and is in units of counts/0.09 deg$^2$. Contours are $T_b = (8,9,11)$ K from 1420 Mhz Canadian Galactic Plane Survey (Taylor et al., 2003). The cross marks the PWN center in X-rays from this work. Note that the radio contours of the nebula from outer to inner are increasing then decreasing: 8,9,11,9 K, indicating the radio hole in the center. The VERITAS excess map is integrated with $\theta < 0.3$ deg, so the $2'$ radio hole, if present, would not be apparent in the gamma-ray map.

## 5.4 Observations

### 5.4.1 X-ray Observations

Observations of DA 495 were performed by *NuSTAR* (ObsID 30362003002) on 2017 June 9 for a total exposure of 60 ks. *NuSTAR* pointed at the X-ray centroid of the PWN at R.A.(J2000) = $19^h\ 52^m\ 17.04^s$, decl.(J2000) = 29° 25′ 52.5" (Arzoumanian et al., 2008). The *NuSTAR* data was processed with `nupipeline 0.4.6`. DA 495 was observed by *Chandra*/ACIS-I on 2002 December 9 (ObsID 3900) for a total of 25 ks.

Observations also took place with *XMM-Newton* EPIC/MOS (Full Frame Mode, medium filter setting) on 2007 April 21 for a total of about 50 ks. *XMM-Newton* data was processed using `XMM SAS 1.2`.

The *NuSTAR*, *Chandra*, and *XMM-Newton* datasets were used for both image analysis and spectroscopy. All three datasets underwent spectral extraction and joint fitting in `XSPEC` (v12.9.0), providing a more complete picture of the DA 495 X-ray emission.

## 5.5 Results

### 5.5.1 Data Analysis

#### 5.5.1.1 *NuSTAR* Data Reduction

The *NuSTAR* data was processed and analyzed using the `HEASOFT V6.21` software package, including `NUSTARDAS 06December16 V1.7.1`, with 2017 June 14 dated Calibration Database (CALDB) files for *NuSTAR*.

*NuSTAR* background-subtracted images were obtained using the `nuskybgd` software (Wik et al., 2014). `Nuskybgd` maps and generates images for the entire background, allowing for specific background spectrum extraction given a source region. It takes into account stray light leaking through the aperture stop, focused cosmic X-ray background, instrumental background, and soft environmental neutrons from cosmic rays. When modeling the background with `nuskybgd`, three source-free regions were selected from each module, each region on a different detector chip. Although stray light contamination mainly manifested below 3 keV, the affected region, the top third of module A, was avoided when choosing background regions for modeling.

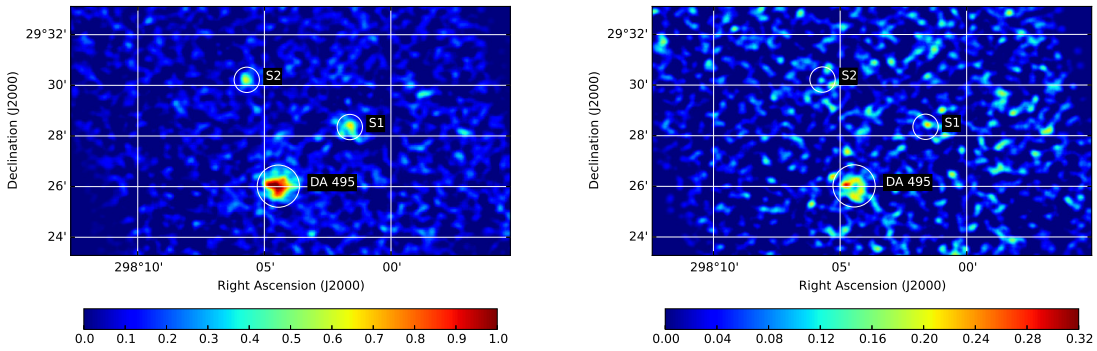


(a) (b)

Figure 5.5 (a) *NuSTAR* modules A and B from 3 to 20 keV, summed and background subtracted. (b) *NuSTAR* modules A and B from 10 to 20 keV, summed and background subtracted. The images were smoothed with a Gaussian kernel to $5\sigma$ significance.

After background subtraction three X-ray sources were visible in the *NuSTAR* field of view (Fig. 5.5a). `CIAO wavdetect` detected the two point sources, S1 and S2, in the *NuSTAR* data from 3 to 10 keV, but did not detect them in the 10 to 20 keV band. DA 495 appears up to 20 keV. The archival *Chandra* data revealed counterpart point sources to S1 and S2: CXO J195205.6+292808 (S1) and CXO J195222.6+293005 (S2). These nonvariable low-energy point sources are extremely unlikely counterparts to the TeV gamma-ray emission and are excluded from further analysis.

### 5.5.2 X-ray Spectral Analysis

We extracted spectra from both the *NuSTAR* data and archival *Chandra* and *XMM-Newton* data and jointly fit the low- and high-energy spectra.

#### 5.5.2.1 *NuSTAR*

For *NuSTAR* spectral extraction with `nuproducts 0.3.0`, a region of r < 50" was used, centered at the PWN centroid in the full band. The extraction region was

increased beyond the X-ray extent of r ~ 20", as the larger *NuSTAR* PSF can cause counts to spill beyond the *Chandra*-measured source extent. A 50" region, determined to be optimal through image analysis and trial-and-error spectral extraction, was large enough to include all or nearly all source counts while preserving a high signal-to-noise ratio. Using `nuproducts` we generated the *NuSTAR* response matrix (RMF) and effective area (ARF) files for an extended source. Extracted spectra from module A and B were found to have consistent fluxes and were combined using `addspec` from `FTOOLS 6.9`. The spectrum was subsequently binned to $2\sigma$ significance over background counts in each bin.

*NuSTAR* background spectra were generated by jointly modeling module A and B with `nuskybgd`. Background spectrum generation with `nuproducts` was also attempted. `Nuproducts` uses only one source-free rectangular background region file per module, which we selected to be on the same detector chip as the source region. Although fitting the source spectra with both `nuskybgd` and `nuproducts` background spectra yielded largely consistent results, `nuskybgd` produced a slightly better match between the A and B spectra and was used for final fitting. Like the source spectra, `addspec` was used to combine the module A and B background spectra generated with `nuskybgd`.

#### 5.5.2.2 *Chandra*

*Chandra* spectral extraction was performed using `CIAO 4.10` procedures for extended emission. An extraction radius of r < 20", the *Chandra*-measured source extent (Karpova et al., 2015), was used. A background spectrum was extracted from a circular, 70" radius, point-source-free region on the same detector chip as DA 495. The extracted source spectrum was variably binned to $2\sigma$ significance.

#### 5.5.2.3 *XMM-Newton*

`XMM SAS 17.0.0` procedures were used for *XMM-Newton* spectral extraction. A region of r < 40" was used for spectral extraction. As *XMM-Newton* has a larger PSF than *Chandra*, a larger region was required to capture all source counts. The background spectrum was extracted from a 70" circle covering a nearby region that was determined to be point-source-free by `XMM SAS edetect_chain`. The extracted source spectrum was variably binned to $2\sigma$ significance.

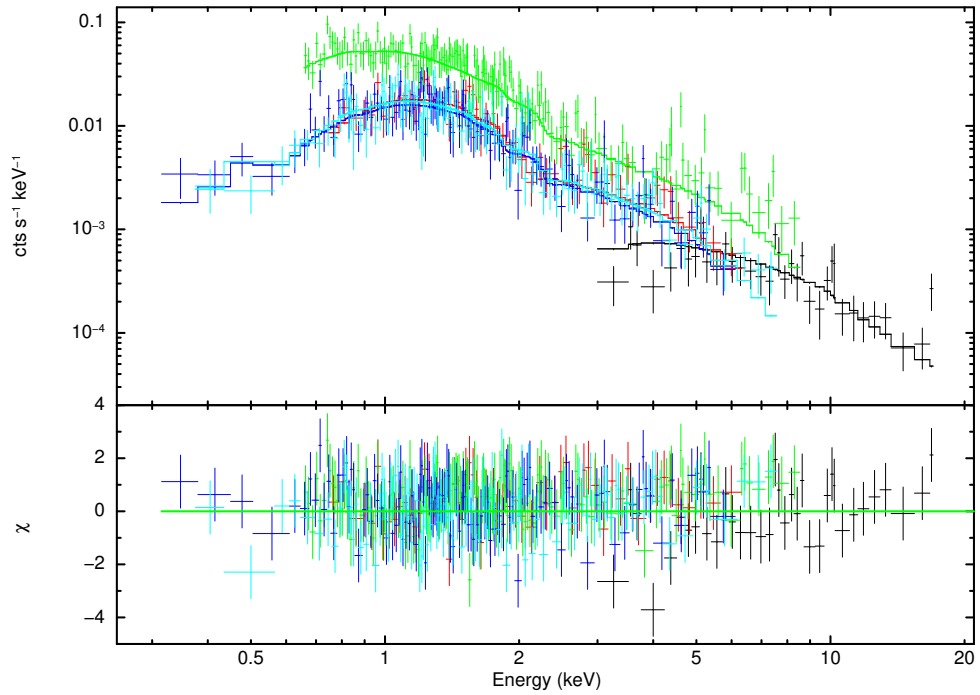


Figure 5.6 *Chandra*, *XMM-Newton*, and *NuSTAR* spectra jointly fit with an absorbed powerlaw plus blackbody model. Black: *NuSTAR*; Red: *Chandra*; Green, Turquoise, and Purple: *XMM-Newton* EPIC PN, MOS 1, and MOS 2, respectively.

| Model | $N_H$, $10^{21}$cm$^2$ | T, eV | R, km | $\Gamma$ | powerlaw norm, $10^{-5}$ | $\chi^2_v$ | dof |
|---|---|---|---|---|---|---|---|
| BB | $3.3^{+1.2}_{-0.8}$ | $180^{+50}_{-40}$ | $0.5^{-0.3}_{+0.8}$ | $2.0 \pm 0.1$ | $6.7^{+1.4}_{-1.3}$ | 1.0 | 482 |
| NSMAX ($B = 10^{12}$ G) | $4.0^{+0.2}_{-0.8}$ | $28^{+6}$ | $10^{+3}_{-9}$ | $1.9 \pm 0.1$ | $5.8^{+0.5}_{-0.7}$ | 1.0 | 482 |

Table 5.2 X-ray joint fit spectral parameters. All errors are given with $1\sigma$ confidence.

#### 5.5.2.4 Fitting Results

When fitting, the *NuSTAR* spectrum was cut off above 20 keV where the background began to dominate. Thus we used a range of 3 to 20 keV for the *NuSTAR* spectrum, a range of 0.5 to 10 keV for *Chandra* and a range of 0.2 to 10 keV for *XMM-Newton* EPIC PN, MOS 1, and MOS 2. All error bars were calculated to $1\sigma$ significance. We fit the *NuSTAR*, *Chandra* and *XMM-Newton* data jointly with an absorbed power-law model plus a blackbody component (`tbabs*(bbodyrad +powerlaw)`) to account for the central pulsar (abundances from Wilms, Allen, and McCray, 2000). This fit (Fig. 5.6) produced a photon index of $\Gamma = 2.0 \pm 0.1$ (typical for a PWN), a neutral hydrogen absorption of $N_H = 3.3^{+1.2}_{-0.8} \times 10^{21}$ cm$^{-2}$, a blackbody temperature of $T = 0.18^{+0.05}_{-0.04}$ keV, and a blackbody radius of $R = 0.5^{+0.8}_{-0.3}$ km (Table 5.2). All results are consistent with Karpova et al., 2015, who theorized that this blackbody radius and temperature model emission from a hot polar cap. X-ray flux was $2.4 \pm 0.1 \times 10^{-13}$ erg s$^{-1}$ cm$^{-2}$ in the 2 to 20 keV band and $2.4^{+0}_{-0.2} \times 10^{-13}$ erg s$^{-1}$ cm$^{-2}$ in the 0.5 to 8 keV band, with $L_{2-20} = 2.9^{+0.2}_{-0.3} \times 10^{31}$ erg s$^{-1}$ at a distance of 1 kpc. This fit resulted in a reduced chi-squared of 1.0 for 482 degrees of freedom, confirming that the spectrum is non-thermal and fits well to a single power-law model. There is no evidence of a spectral cutoff or break up to 20 keV.

The spectra were also fit with a neutron star atmosphere model as a replacement for the blackbody model (`tbabs*(NSMAX+powerlaw)`) with $B = 10^{12}$ G to model thermal emission from the entire neutron star surface. This fit resulted in a photon index of $\Gamma = 1.9 \pm 0.1$, a neutral hydrogen absorption of $N_H = 4.0^{+0.2}_{-0.8} \times 10^{21}$ cm$^{-2}$, an atmosphere temperature of $T = 28^{+6}$ eV, and a radius of $R = 10^{+3}_{-9}$ km (Table 5.2). No lower limit was derived for the temperature, as the temperature fit to the lower limit value of the model. The gravitational redshift was frozen to a

standard value of 0.3. The NSMAX fit is not shown in Fig. 5.6, as it resulted in similar residuals and goodness of fit as the blackbody model.

#### 5.5.2.5 Spatially Resolved Spectral Analysis with Chandra

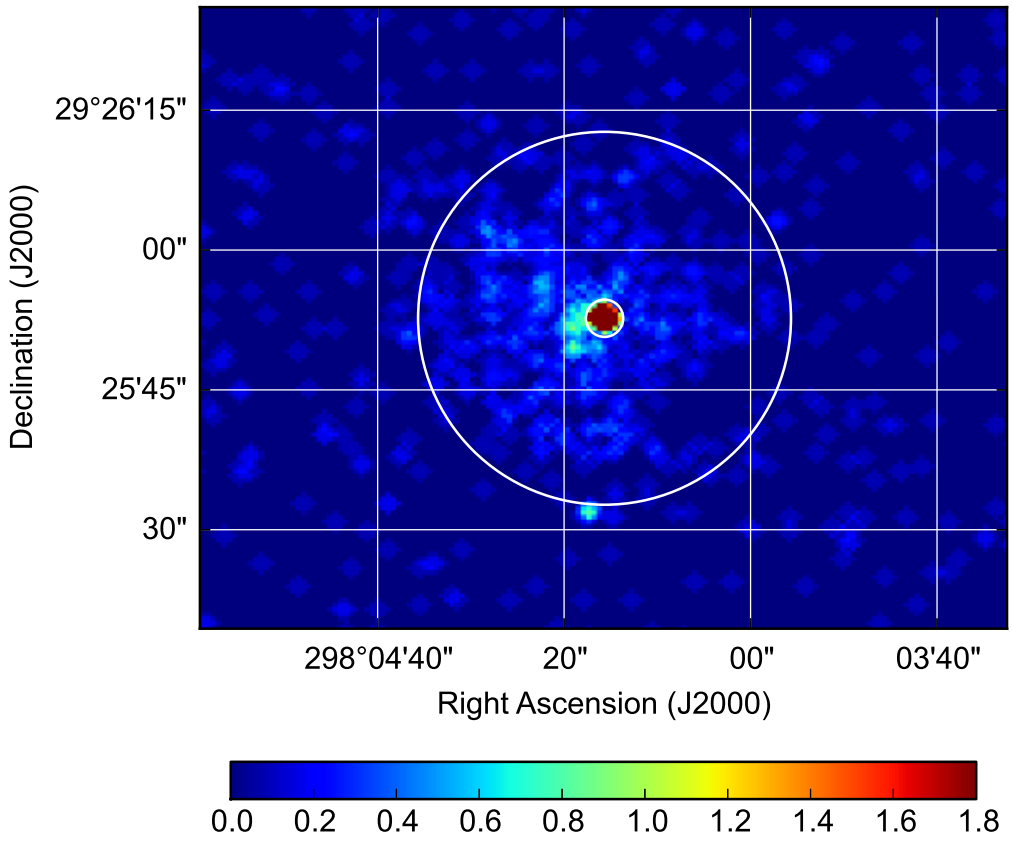


Figure 5.7 *Chandra* image of the DA 495 wind nebula, 0.5 - 8 keV, smoothed with a Gaussian kernel to $3\sigma$ significance. Inner green 2" circle denotes pulsar location, outer 40" green circle denotes wind nebula extent.

*Chandra*'s high angular resolution (~0.5") was used to investigate potential spectral softening at larger distances from the central pulsar due to synchrotron burnoff in the pulsar's leptonic wind. Spectra were extracted from two annuli: 2" $< r_1 <$ 10" and 10" $< r_2 <$ 20". The inner 2" of the nebula were ignored to avoid the contribution of blackbody emission from the putative central pulsar. Each annu-

lus spectrum was extracted using `CIAO 4.10` extended emission procedures and was fit in `XSPEC` from 0.5 to 8 keV with an absorbed power law model (again, using abundances from Wilms, Allen, and McCray, 2000). The fitting resulted in an $N_H$ of $4.8^{+2.6}_{-2.0} \times 10^{21}$ and a photon index of $1.9 \pm 0.2$ for $r_1$ ($\chi^2_v = 0.6, 13$ dof), while $r_2$ gave an $N_H$ of $4.8^{+3.7}_{-2.4} \times 10^{21}$ and a photon index of $1.9 \pm 0.3$ ($\chi^2_v = 0.9, 15$ dof). These $N_H$ and $\Gamma$ values are consistent with the full *Chandra* spectrum extracted from the region 2" < r < 20".

A radial profile of the *Chandra* data was generated using an inner radius of 2", an outer radius of 20", and 5 annuli. We plotted the brightness of the wind nebula as a function of distance from the central point source in the energy bands 0.5-1.0 keV, 1.0-3.0 keV, and 3.0-8.0 keV, normalizing the data points at r = 2" to 1.0 and subtracting the background. We saw no significant spectral hardening or softening between the three energy bands. In the annular fits, the photon index stays constant within error bars at larger distances from the central pulsar, consistent with the radial profile results. We report no evidence of quickening in the burnout of electrons at higher energies.

#### 5.5.2.6 X-ray Flux Upper Limit

An X-ray flux upper limit for SED fitting was extracted by analyzing the extended emission within the radio nebula region r < 12.5′ (Fig. 5.8b). In a single electron population leptonic emission scenario one would expect diffuse X-ray emission coincident with the large radio nebula. *XMM-Newton* was the only X-ray telescope with a large enough field of view to be used to attempt a diffuse nebula upper limit. EPIC-MOS 2 was the sole camera used for analysis, as two CCD chips in MOS 1 were compromised, and EPIC-PN was operated in the Small Window mode. `XMM SAS 17.0.0 ESAS` procedures were used for source and background

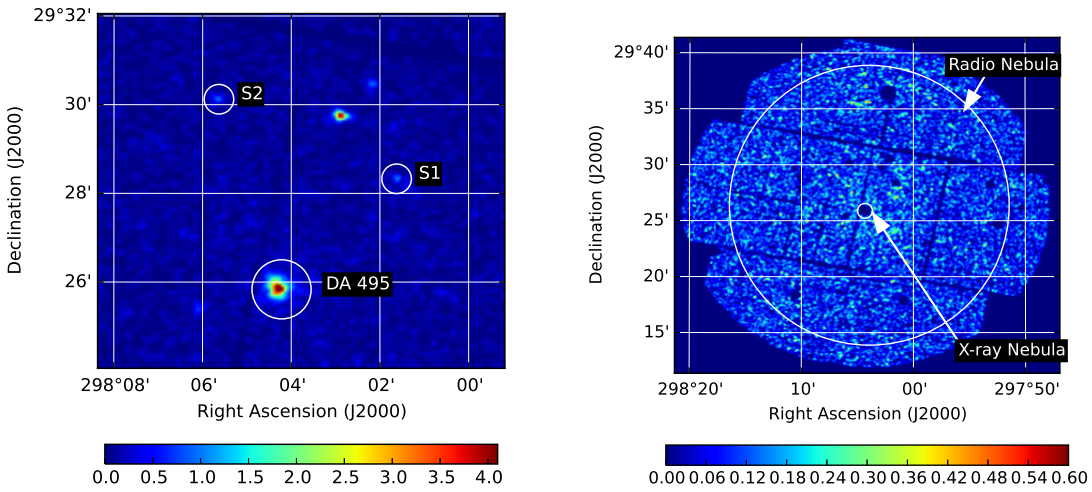


(a) (b)

Figure 5.8 (a) XMM-MOS 2 image of DA 495, 0.5-10 keV. (b) XMM-MOS 2 background subtracted and point-source masked image, 2-10 keV. Both images were smoothed with a Gaussian kernel to $3\sigma$ significance.

spectrum generation. ESAS background subtraction procedures account for the quiescent particle background (QPB), but do not account for CXB emission, solar wind charge exchange (SWCX) background, soft proton background, or instrumental lines. Because instrumental lines and SWCX effects manifest below 2 keV, all energies below 2 keV were ignored. The lightcurve of the region was examined and no flares were found. The CXB was accounted for by fitting a second power-law to the spectrum using the known photon index of $\Gamma = 1.46$ (Snowden, Collier, and Kuntz, 2004). It was not possible to directly subtract a local background spectrum, as the radio nebula covers the entire XMM field of view and therefore no region was guaranteed to be source-free. All point-like sources, including DA 495, were masked using the `XMM ESAS cheese` command, and the extended emission spectrum was fit separately from the compact nebula. Because of the sharp (factor of ~6) drop in flux between the compact X-ray nebula and surrounding background (Fig. 5.8), it is unlikely that much of the measured X-ray flux from the radio emission region is from DA 495.

When fitting the extended region, $N_H$ was frozen to the joint fit value of $3.3 \times 10^{21}$ cm$^{-2}$. Subtracting the relevant background components and ignoring the photons below 2 keV resulted in a flux (2-10 keV) of $3.6^{+0.7}_{-0.5} \times 10^{-12}$ erg s$^{-1}$ cm$^{-2}$ when the DA 495 photon index was allowed to fit freely (very soft at $\Gamma \approx 5.6$), and a flux of $\approx 4.7 \times 10^{-12}$ erg s$^{-1}$ cm$^{-2}$ when the photon index was frozen to the DA 495 best fit value of 2.0 (with the normalization of the CXB component frozen to the value found in the previous fit). The compact X-ray nebula upper limit flux was measured to be $\approx 1.6 \times 10^{-13}$ erg s$^{-1}$ cm$^{-2}$ in the 2-10 keV band. The extended region flux (with all point-like sources masked) was added to the DA 495 compact flux value to gain a diffuse X-ray nebula upper limit of $(3.3 - 4.9) \times 10^{-12}$ erg s$^{-1}$ cm$^{-2}$.

## 5.6 DA 495 PWN Spectral Modeling

The multi-wavelength spectra and spatial extents of DA 495 PWN provide strong constraints on the underlying radiation processes. In particular, since the X-ray nebula has significantly smaller extent than the radio and TeV nebulae, it naturally argues for a two-zone model, where the inner X-ray nebula originates from recent acceleration of primary electrons in the neighborhood of the central pulsar with a probably higher magnetic field, while the more extended radio and TeV nebulae are the consequence of older particles that have diffused away from the central pulsar. Given the very high flux of the extended TeV nebula, there could be a hadronic contribution to the high-energy spectral component. In this section, we discuss the fitting models for the broadband spectrum of the extended radio and TeV nebulae as well as the compact X-ray nebula. We use both the spectrum and spatial extent to constrain the model parameters. Fitting results are shown in Figures 5.10 and 5.9 with model parameters listed in Table 5.3.

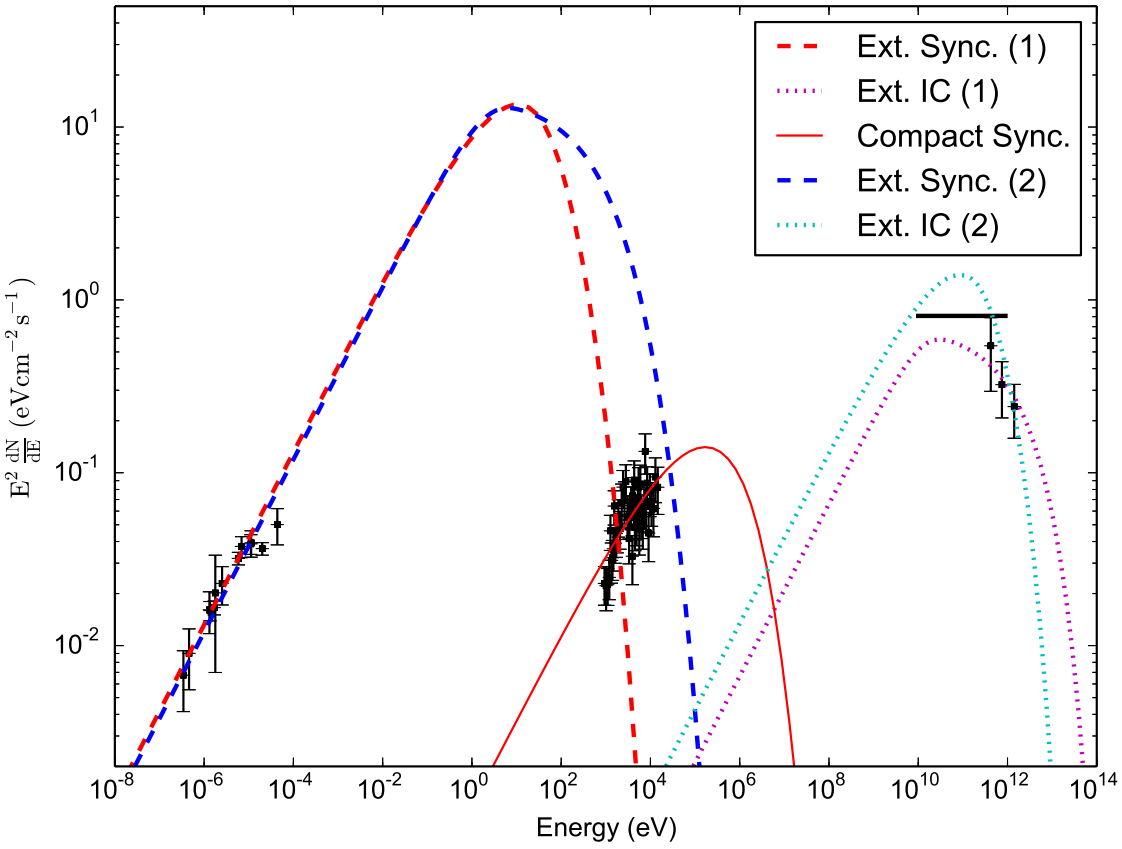


Figure 5.9 Leptonic model 1 and 2. The extended radio and TeV nebulae are fit with inverse Compton scattering by primary electrons (magneta dot for model 1 and cyan dot for model 2) and primary electron synchrotron (red dash for model 1 and blue dash for model 2). The compact X-ray nebula is fit with another primary electron synchrotron (red solid). Parameters are listed in Table 5.3. Black points are the radio Kothes et al. (2008), X-ray (this work) and VERITAS data points (Abeysekara et al., 2018b). Black solid line is the *Fermi* upper limits (Abeysekara et al., 2018b).

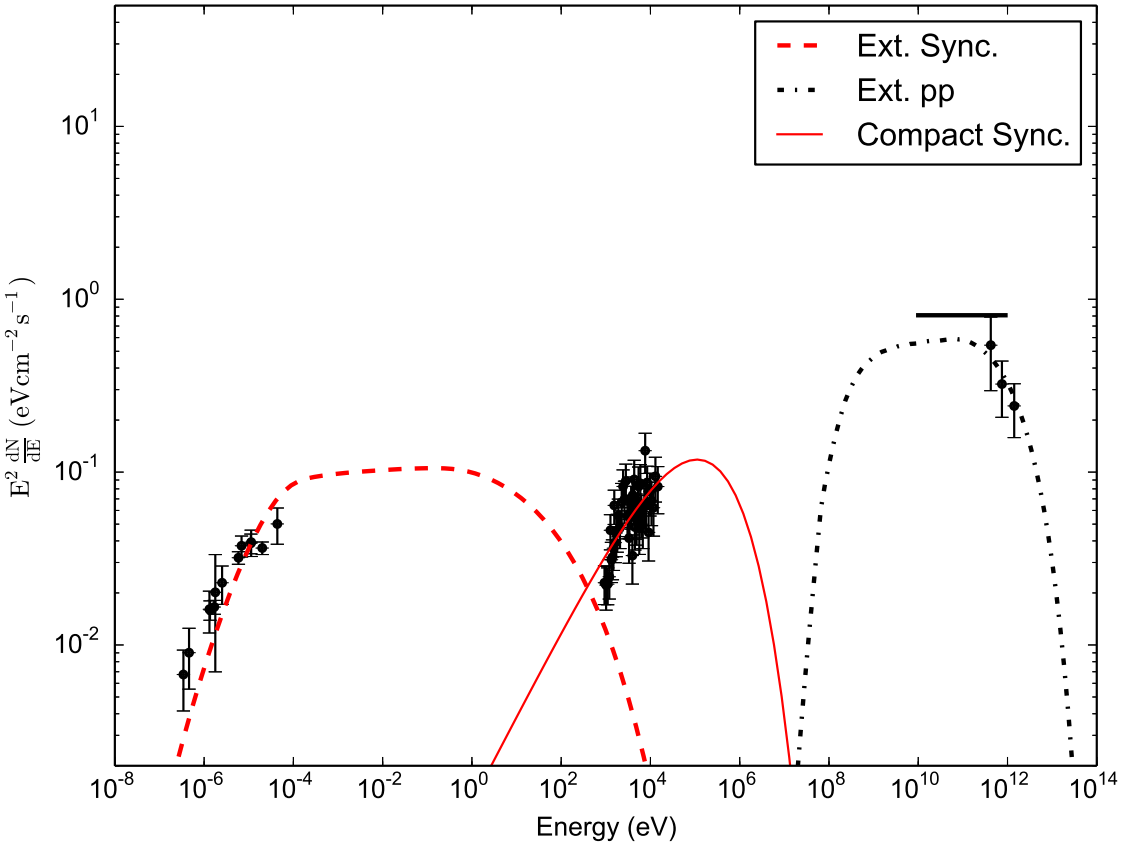


Figure 5.10 Hadronic fit of the broadband SED. The extended radio and TeV nebulae are fit with pp collisions of primary protons (black dash dot) and secondary pair synchrotron (red dash). The compact X-ray nebula is fit with the primary electron synchrotron (red solid). Parameters are listed in Table 5.3. Black points are the radio Kothes et al. (2008), X-ray (this work) and VERITAS data points (Abeysekara et al., 2018b). Black solid line is the *Fermi* upper limits (Abeysekara et al., 2018b).

| Extended radio and TeV nebulae parameters | Leptonic Model 1 | Leptonic Model 2 | Hadronic Model |
|---|---|---|---|
| Distance | 1 kpc | | |
| Magnetic field | 10 $\mu$G | 15 $\mu$G | 0.8 mG |
| Electron minimal Lorentz factor | 1 | | – |
| Electron maximal Lorentz factor | $10^7$ | $5 \times 10^7$ | – |
| Electron power-law index | 2.0 | 2.0 | – |
| Electron total kinetic energy | $2 \times 10^{47}$ erg | $10^{47}$ erg | – |
| Proton minimal Lorentz factor | – | – | 1.0 |
| Proton maximal Lorentz factor | – | – | $2 \times 10^4$ |
| Proton power-law index | – | – | 2.0 |
| Proton total kinetic energy | – | – | $7 \times 10^{48}$ erg |
| Target proton density | – | – | 1 cm$^{-3}$ |
| Diffusion coefficient | $4 \times 10^{25}$ cm$^2$s$^{-1}$ | | $1.5 \times 10^{25}$ cm$^2$ s$^{-1}$ |
| Compact X-ray nebula parameters | | | |
| Magnetic field | 50 $\mu$G | | 0.8 mG |
| Electron minimal Lorentz factor | 1 | | |
| Electron maximal Lorentz factor | $5 \times 10^8$ | | $10^8$ |
| Electron power-law index | 2.0 | | |
| Electron total kinetic energy | $2 \times 10^{42}$ erg | | $3 \times 10^{40}$ erg |

Table 5.3 Fitting parameters of leptonic and hadronic models. Notice that our radiation code considers radiation cooling, which may introduce a cooling break in the power-law spectrum.

### 5.6.1 Pure Leptonic model

In a pure leptonic model, the radio to TeV emission generally consists of two components, namely, a low-energy component from synchrotron emission from primary electrons and a high-energy component from inverse Compton scattering of CMB photons by the same electrons. Given the large extents of the radio and TeV nebulae, the primary electron synchrotron photon density is much lower than the CMB. Thus we do not expect a significant synchrotron-self Compton contribution. The compact X-ray nebula originates from the neighborhood of the central pulsar, where the higher magnetic field and freshly accelerated electrons trigger an additional synchrotron component.

We can estimate the average magnetic field strength within the radio and TeV nebulae based on the spectral shapes. In a pure leptonic model, the radio and TeV emission should come from the same electron population. Since the radio spectrum is rising in a power-law shape while the TeV spectrum appears like a cutoff, we expect that the underlying electron spectrum has a spectral break at some maximal energy. To upscatter CMB photons to TeV energies, the primary electron cutoff should be $\sim 20$ TeV. Generally speaking, this spectral break can have two origins, either the synchrotron cooling break or the intrinsic spectral cutoff. If the electron cutoff at $\sim 20$ TeV results from synchrotron cooling, the synchrotron cooling time scale should be comparable to the source age,

$$t_{cool} = \frac{m_e c^2}{4/3 c \sigma_T \gamma (u_B + u_{CMB})} = 0.976 \text{ yr } \gamma^{-1} (u_B + u_{CMB})^{-1} \sim t_{age} = 20 \text{ kyr} \ . \quad (5.1)$$

Therefore, we can find that $B \sim 8$ $\mu$G, consistent with the ISM magnetic field. This implies that the synchrotron component should peak at

$$h\nu_c = h \frac{3eB}{4\pi m_e c} \gamma^2 \sim 1.74 \times 10^{-8} \text{ eV } B\gamma^2 \sim 50 \text{ eV} \ , \quad (5.2)$$

which is in the ultraviolet.

The extent of the TeV nebula is likely determined by the diffusion of TeV electrons. The typical interstellar diffusion coefficient of $\sim 10$ TeV electrons is $\sim 10^{29}$ cm$^2$s$^{-1}$. Considering the radiative cooling of these TeV electrons in the ISM, the diffusion radius is given by

$$d_{dif} = 2\sqrt{D t_{cool}} \sim 100 \text{ pc}. \tag{5.3}$$

Apparently, the extent should be much larger than the observed angular extent assuming a distance of 1 kpc. To trap the high-energy electrons within the observed $\sim 2$ pc region, the diffusion coefficient should be $D \sim 4 \times 10^{25}$ cm$^2$s$^{-1}$, much smaller than the ISM diffusion coefficient. Comparing to the Bohm diffusion coefficient, which is given by

$$D_{Bohm} = \frac{1}{3}\frac{\gamma m c^2}{eB} c \sim 6.67 \times 10^{25} \text{ cm}^2\text{s}^{-1} \left(\frac{B}{5\ \mu\text{G}}\right)^{-1}, \tag{5.4}$$

the observed slow diffusion then sets a lower limit on the average magnetic field, $B \gtrsim 10$ ¯G. Recent HAWC observation of the Geminga PWN suggested a similarly small diffusion coefficient within the Geminga nebular diffusion comparable to the local Bohm diffusion coefficient (Abeysekara et al., 2017a; López-Coto et al., 2018), which is consistent with our DA 495 fitting parameters.

Since the same electrons produce the radio emission through synchrotron and the TeV emission through inverse Compton scattering, their flux levels can be used to derive the ratio between the magnetic energy density and the target photon energy density, namely, $u_B/u_{CMB}$. Figure 5.9 shows our leptonic fitting results. We find that the magnetic field cannot be too high, or else there should exist a very bright X-ray nebula of similar size to the radio and TeV nebulae, which cannot be confirmed in our observations. Notice that our spectral fitting considers cooling effects, thus we observe a cooling break in the $B = 15\ \mu$G case.

The sharp cutoff at the edge of the central compact X-ray nebula implies a stronger magnetic field and newly accelerated electrons. Figure 5.9 shows a sam-

ple fitting with 50 ¯G magnetic field, although with merely X-ray data we cannot constrain both the magnetic field strength and the electron spectrum. The higher magnetic field strength should infer brighter radio emission within the compact X-ray nebula. Instead, K08 suggests an apparent radio hole in that region. This casts doubt on simple leptonic models.

### 5.6.2 Pure Hadronic Model

In a pure hadronic model, the broadband emission of the extended nebula originates from proton-proton (pp) collisions, where the neutral pion decay makes the high-energy spectral component while the charged pion decay results in secondary electron-positron pairs, which then give rise to the low-energy spectral component through synchrotron radiation. The compact X-ray nebula is likely the primary electron synchrotron radiation, and its small extent is due to the fast cooling time of these electrons in a high magnetic field.

The observed radio and TeV spectra can put strong constraints on the underlying proton spectral distribution and magnetic field strength. The soft TeV spectral shape indicates the neutral pion decay spectral cutoff. This corresponds to a proton cutoff energy at (Kelner, Aharonian, and Bugayov, 2006)

$$E_{p,cut} = 10 \times E_{\gamma,cut} \sim 10 \text{ TeV} \ . \tag{5.5}$$

Meanwhile, the rising radio spectrum marks the low-energy cutoff of the secondary electrons. These electrons, which come from the charged pion decay, should have a low-energy cutoff at $\sim 500$ MeV (Kelner, Aharonian, and Bugayov, 2006). This is because the cross section of the pp collisions cuts off when the nonthermal protons become nonrelativistic. Therefore, we can quickly derive from Equation 5.2 that the magnetic field strength should be

$$B \sim 0.5 \text{ mG } \frac{E_{radio}}{10^{-5} \text{ eV}} \left( \frac{\gamma}{10^3} \right)^{-2}. \tag{5.6}$$

Since the cross section for charged pions is about half of the neutral pion cross-section, and part of the charged pion energy goes into neutrinos, the total electron power from pp collisions is typically about one third of the total $\gamma$-ray power. We can see from the DA 495 spectrum that the TeV flux is $\sim$5 times higher than the radio flux, indicating that the secondary synchrotron emission is very efficient (Figure 5.10). Indeed, we can quickly estimate from Equation 5.1 that the cooling time of the secondary electrons in a $\sim 0.5$ mG magnetic field should be $\sim 90$ kyr for the low-energy cutoff electrons at $\sim 500$ MeV, on the same order of the source age.

Given the extent of the TeV nebula, we can estimate the diffusion coefficient inside. Since the protons that produce the TeV emission do not cool in the nebula, the diffusion coefficient is

$$D = \left(\frac{R}{2}\right)^2 / t_{age} \sim 1.5 \times 10^{25}\ \mathrm{cm^2\,s^{-1}}\ , \tag{5.7}$$

a little smaller than that in the leptonic scenario. But here the magnetic field is two orders of magnitude higher than the typical ISM value, thus the diffusion coefficient is well above the Bohm limit.

While the radio and TeV nebulae are produced by pp collisions, the compact X-ray nebula near the central pulsar comes from the primary electrons co-accelerated with the protons. Due to the high magnetic field, these electrons will cool in a short time, which naturally explains the small spatial extent of the X-ray nebula. From Equation 5.2, the X-ray spectral shape implies that the primary electrons should be accelerated to $\sim 20$ TeV, consistent with the maximal proton energy.

## 5.7 Discussion

With the detection of high-energy X-ray and TeV emission, we have modeled several different scenarios that explain the nature of the broadband emission from DA 495. K08 and Arzoumanian et al. (2008) describe DA 495 as a PWN possibly unconstrained by the presence of a reverberation supernova reverse shock, allowing for the ∼20 kyr PWN to expand with an $R_{radio}/R_{X-ray} \sim 10\times$ that of PWN of similar age (∼ 20 kyr). It is also understood that the radio region is highly magnetized with a strong dipole field and that the dipole axis aligns with asymmetries in the X-ray observations likely due to a jet from the pulsar.

Even before the hard X-ray and TeV detection, DA 495 was an enigmatic PWN, and our modeling with the newest observations continues to support this idea - as well as opens up some new questions. There now exists tension between the current understanding and the SED modeling scenarios that we presented in the previous section, particularly once we include the TeV emission. In this section we will discuss some of these conflicts and explain future studies that could shed light on the emission processes.

### 5.7.1 Estimated Age

Certainly, without a detected pulsar the age estimation becomes more challenging. There are several relationships for PWN that can place rough age constraints on the undetected pulsar based on observational parameters alone.

A study on the X-ray and $\gamma$-ray luminosity of PWN (Mattana et al., 2009) describes a relationship between $L_{1-30\ TeV}/L_{2-10\ keV}$ that can be used to find $\tau_c$ of the pulsar and $\dot{E}$. This is a characteristic relationship due to the different electron populations that generate the X-ray synchrotron and TeV inverse-Compton emissions. Using the 1kpc luminosity from the VERITAS spectral fit and the joint

X-ray fit in this work: $L_{1-30\ TeV} = (1.3 \pm 0.2) \times 10^{31}$ erg s$^{-1}$ and $L_{2-10\ keV} = (2.6 \pm 0.2) \times 10^{31}$ erg s$^{-1}$ for a ratio of $L_{1-30\ TeV}/L_{2-10\ keV} = 0.50 \pm 0.05$. This results in a derived $\dot{E} = (2.6 \pm 0.2) \times 10^{37}$ erg s$^{-1}$ and $\tau_c = 3.5 \pm 0.5$ kyr – dramatically different than the K08 estimated values of $\dot{E} \sim 10^{35}$ erg s$^{-1}$ and $\tau_c \sim 20$ kyr. The authors in Mattana et al. (2009) note that DA 495 is expected to be an exception with respect to their fits due to the strong magnetic field inferred from radio observations. Now that we have included the TeV emission, we can confirm their suspicions that DA 495 does not line up with the rest of the PWN population from an observational perspective.

Another population study of PWNe was performed by HESS (H.E.S.S. Collaboration et al., 2018), where we get yet another story about the age. For this study, TeV luminosity ($L_{1-10\ TeV}$) was used to find estimate the age, spindown luminosity, and size. Using the K08 age for DA 495, the expected $L_{1-10\ TeV}$ (@20 kyr and 1 kpc) is $\sim 7 \times 10^{33}$ erg s$^{-1}$. The measured $L_{1-10\ TeV}$ (@1 kpc) $= (1.3 \pm 0.2) \times 10^{31}$ erg s$^{-1}$ would put the age at $>$1 Myr when using the HESS flux. So, while the enhanced TeV emission is causing issues with understanding the SED models with a strong magnetic field, by these estimates the TeV emission is very low for the expected age as the TeV luminosity is expected to decrease with the PWN age. There is some suggestion in K08 that DA 495 is at a larger distance ($D \sim 5$ kpc). The measured luminosity, $L_{1-10\ TeV}$ (@1 kpc) $= (3.3 \pm 0.4) \times 10^{31}$ erg s$^{-1}$, still has significant disagreement with any assumed age. Without any other age estimates, the luminosity at 5 kpc would still put the age of DA 495 at $>$1 Myr. We are not suggesting that DA 495 is a remnant that old, but that it is an outlier from an observational standpoint and that standard evolutionary scenarios do not apply.

These conflicting results on the age of DA 495 reinforce our conclusions that it has not followed a typical evolutionary path. Time-dependent modeling of atyp-

ical evolutionary scenarios of the PWN would be the most likely way to help resolve some of the questions regarding possible age.

### 5.7.2 PWN or Shell-SNR?

The magnetic field strength estimated from the radio observations and the SED may be reconciled using a model including hadronic-based emission from $\pi^0$-decay. This requires hadronic target material and the presence of a SNR shell. This is contrary to the K08 claim about the lack of a shell, though earlier interpretation of the radio emission from Velusamy et al. (1989) argued that DA 495 is a composite remnant with a thick shell due to slow supernova ejecta interacting with the reverse shock. The thick shell claim may still be considered a possibility if there is a superimposed toroidal magnetic field as K08 suggests. The magnetic field strength of the hadronic scenario may be possible with there only being a shock interacting with ejecta in a ring around the source. This, in part, could also explain the very low surface brightness of the nebula, since the radio and TeV emission would be coming only from the equatorial ring. However, the physical reason how the toroidal magnetic field was entrapped is not clear. This interpretation still has issues within the context of other observations as there is not an obvious, cooler, dense, target region as expected with most shock interactions.

A way to further investigate the existence of a shell-type remnant would be to examine the TeV morphology more closely. The radio hole is about $2'$ in diameter, and if the radio and TeV emission both share this feature, then this could indicate that the emission is from a shocked region where the magnetic field was compressed. The putative hadronic targets in this possible scenario being slower ejecta from the supernova. If the TeV emission is smooth through the middle of the region, then that would indicate that the electrons from the central pulsar are

likely responsible for the TeV emission. This argues against the hadronic scenario, since the radio and TeV emissions are no longer spatially linked. Currently, none of the gamma-ray instruments are sensitive enough to definitively make this distinction, but the Cherenkov Telescope Array (CTA), due to come online in the next few years, may have the enhanced angular resolution necessary (CTA Consortium, 2019).

### 5.7.3 Radiation Mechanism and Magnetic Field

While both leptonic and hadronic scenarios can reasonably reproduce the multi-wavelength observation (Figures 5.10 and 5.9), we can quickly notice several key predictions from the spectral modeling. For a pure leptonic model, we expect a straight power-law in the low-energy spectral component, from radio to optical. K08, however, suggested a spectral break in the radio component. Future observations at higher radio frequencies to far infrared may help to diagnose the significance of this spectral break. Additionally, the pure leptonic model predicts rather high optical to ultraviolet flux. Most interestingly, it implies that there exists a diffusive X-ray nebula that is of similar size as the radio and TeV nebulae. The total flux is comparable to the central compact X-ray nebula, but since it spreads out $\sim 2$ pc, its surface brightness can be much lower than the central compact X-ray nebula, which is very hard to detect. The leptonic model requires an average magnetic field that is slightly higher than the typical ISM value, probably due to the interaction between pulsar wind and the ISM, or maybe the remnant magnetic field from the supernova. The total energy budget for the leptonic model is $\sim 10^{48}$ erg, typical for PWNe.

The hadronic models lead to very different predictions. In a pure hadronic model, the radio spectral break is a natural result of the secondary pair synchrotron.

Both the infrared to optical and *Fermi* $\gamma$-ray spectra should appear flat, assuming an underlying proton energy spectral index of $\sim 2.0$. The purely hadronic model also suggests that there is no diffusive X-ray nebula, which is consistent with our observations. However, the hadronic model requires a very strong magnetic field pervading the radio and TeV nebulae, which is likely powered by the central pulsar, consistent with K08. Nonetheless, protons are generally unlikely to be accelerated at typical particle acceleration sites near the pulsar, such as the polar cap. Instead, they should be accelerated due to the interaction between the pulsar wind and the ISM, or magnetic reconnection in the highly magnetized nebula. These features require that DA 495 is a very unusual PWN, one which has extremely high power and can extend its magnetic field to $\sim 2$ pc into the ISM. Interestingly, the latter is supported by the radio polarization map by K08, where they find a dipole shape magnetic field morphology in the radio nebula.

## 5.8 Conclusion

In this paper we presented new observations from *NuSTAR*. We combined this new analysis with recent TeV gamma-ray observations and the current radio analysis to create a broadband spectral energy distribution for DA 495. Using analytical modeling we described several scenarios for the particle population within the PWN, and put the modeling in context with previous discussion about DA 495's nature described in (*eg*) Kothes et al. (2008).

DA 495 is a unique PWN, still with many unknowns. We find some evidence for a non-PWN scenario that could interpret the radio and TeV emission as a thick shell containing relativistic hadrons – possibly accelerated from the supernova shock that is interacting with some slow supernova ejecta. This challenges the current interpretation and requires further investigation by future TeV gamma-

ray observations. With better angular sensitivity, comparisons between radio and TeV morphology could provide evidence regarding this conclusion.

## 5.9 Acknowledgements

The authors would like to thank S. Reynolds and M. Pohl for their insightful discussions. This work used data from the *NuSTAR* mission, a project led by the California Institute of Technology, managed by the Jet Propulsion Laboratory, and funded by NASA. We made use of the *NuSTAR* Data Analysis Software (NuSTARDAS) jointly developed by the ASI Science Data Center (ASDC, Italy) and the California Institute of Technology (USA). HZ acknowledges the support from Fermi Guest Investigator program, Cycle 11, grant number 80NSSC18K1723. TBH acknowledges the generous support of the National Science Foundation under cooperative agreement PHY-1352567. HL acknowledges the support by the LANL/LDRD program.

# CHAPTER 6

# CONCLUSION

Pulsar wind nebulae and shell-type supernova remnants make significant contributions to the cosmic rays that are emitted within our galaxy and detected on Earth. Observations of the very high energy (VHE) gamma rays emitted in the vicinity of supernova remnants can help to pin point where these particles are accelerated and give us a better understanding of the processes that are at work since we cannot determine the origin of cosmic rays after they have been deflected by intervening magnetic fields. Imaging air Cherenkov telescopes play a key role in producing sky maps and spectra which can be used, with the other broad band observations, to locate the regions of particle acceleration. In this thesis, there are three sources in which the detection of VHE gamma rays has added a unique and significant perspective to the object of interest.

First, I used VERITAS to confirm the detection of two VHE gamma-ray sources which were observed in the same field of view using 8 hours of observations. The observations were targeted at the high mass X-ray binary LS 5039. It was detected with a statistical significance of $8.8\sigma$ and the known orbital phase ephemeris allowed for a time-based spectral study. The measured flux above 1 TeV is $(2.5 \pm 0.4) \times 10^{-12}\,\mathrm{cm}^{-2}\,\mathrm{s}^{-1}$ near inferior conjunction and $(7.8 \pm 2.8) \times 10^{-13}\,\mathrm{cm}^{-2}\,\mathrm{s}^{-1}$ near superior conjunction. Prior to the VHE gamma ray observations made by HESS, LS 5039 was thought to be a microquasar with emission due to accretion of mass from the donor star to a compact object. Careful study of the X-ray, MeV gamma ray, and TeV gamma ray light curves has cast doubt on the microquasar interpretation where the modulation is due to a change of accretion based on a

variable mass transfer (due to distance). Instead, differences in the light curves indicates that the modulation of emission based on the orbital phase is a line-of-sight effect due to Doppler beaming (Takata et al., 2014). This scenario favors a pulsar wind nebula being present around the compact object, and thus a neutron star is injecting particles constantly into the system. Without the TeV light curve, the nature of the compact object would likely still be elusive.

The pulsar wind nebula HESS J1825-137, in the same field of view as LS 5039, was detected with a statistical significance of $6.7\sigma$ and a measured flux above 1 TeV of $(3.9 \pm 0.8) \times 10^{-12}\,\mathrm{cm}^{-2}\,\mathrm{s}^{-1}$. The PWN was first detected in TeV gamma rays, and is a useful prototype given the detail allowed by its extension to help evaluate other PWN. Detailed morphological studies of HESS J1825-137, in particular, has allowed for the particle transport within PWN to be studied in more detail (H. E. S. S. Collaboration et al., 2019). The analysis of VERITAS observations have confirmed the spectrum and morphology.

Finally, the PWN DA 495, known as a radio source for over 50 years, was recently detected to be a source of TeV gamma rays by HAWC and VERITAS. The work described here has cast some doubt on its nature as an isolated PWN. The TeV emission is unexpected given the strong magnetic-field (1mG) that is apparent from the most recent radio analysis (Kothes et al., 2008). Hadrons being accelerated in the shock of a shell-type supernova remnant that presents as a thick shell could explain the TeV emission, and still allows for 1mG magnetic field. This is counter to the "pure PWN" interpretation where the reverse shock of the SN has not compacted the PWN. X-ray emission is not apparent in the extension of DA 495 (though, it cannot be ruled out) and the tested leptonic scenarios presume a X-ray nebula of similar size. Unfortunately, DA 495 remains enigmatic, but future observations by CTA could provide additional detail about the VHE morphology of DA 495 and give additional evidence as to the nature of the particles that are ac-

celerated in the region. The study of TeV gamma rays has added significantly to the understanding of DA 495.

## BIBLIOGRAPHY


Aab, A. et al. (2018). "An Indication of Anisotropy in Arrival Directions of Ultra-high-energy Cosmic Rays through Comparison to the Flux Pattern of Extra-galactic Gamma-Ray Sources". In: *Astrophysical Journal, Letters* 853, L29, p. L29. DOI: 10.3847/2041-8213/aaa66d. arXiv: 1801.06160.

Abdo, A. A. et al. (2010). "Observation of Supernova Remnant IC 443 with the Fermi Large Area Telescope". In: *Astrophysical Journal* 712, pp. 459–468. DOI: 10.1088/0004-637X/712/1/459. arXiv: 1002.2198.

Abdo, A. A. et al. (2011). "Observations of the Young Supernova Remnant RX J1713.7-3946 with the Fermi Large Area Telescope". In: *Astrophysical Journal* 734, 28, p. 28. DOI: 10.1088/0004-637X/734/1/28. arXiv: 1103.5727.

Abeysekara, A. U. et al. (2017a). "Extended gamma-ray sources around pulsars constrain the origin of the positron flux at Earth". In: *Science* 358, pp. 911–914. DOI: 10.1126/science.aan4880. arXiv: 1711.06223.

Abeysekara, A. U. et al. (2017b). "The 2HWC HAWC Observatory Gamma-Ray Catalog". In: *Astrophysical Journal* 843, 40, p. 40. DOI: 10.3847/1538-4357/aa7556. arXiv: 1702.02992.

Abeysekara, A. U. et al. (2018a). "Periastron Observations of TeV Gamma-Ray Emission from a Binary System with a 50-year Period". In: *Astrophysical Journal, Letters* 867, L19, p. L19. DOI: 10.3847/2041-8213/aae70e. arXiv: 1810.05271.

Abeysekara, A. U. et al. (2018b). "VERITAS and Fermi-LAT Observations of TeV Gamma-Ray Sources Discovered by HAWC in the 2HWC Catalog". In: *Astrophysical Journal* 866, 24, p. 24. DOI: 10.3847/1538-4357/aade4e. arXiv: 1808.10423.

Acciari, V. A. et al. (2010). "Observations of the Shell-type Supernova Remnant Cassiopeia A at TeV Energies with VERITAS". In: *Astrophysical Journal* 714, pp. 163–169. DOI: 10.1088/0004-637X/714/1/163. arXiv: 1002.2974.

Ackermann, M. et al. (2013). "Detection of the Characteristic Pion-Decay Signature in Supernova Remnants". In: *Science* 339, pp. 807–811. DOI: 10.1126/science.1231160. arXiv: 1302.3307.

Aharonian, F. et al. (2005a). "Discovery of Very High Energy Gamma Rays Associated with an X-ray Binary". In: *Science* 309, pp. 746–749. DOI: 10.1126/science.1113764. eprint: astro-ph/0508298.

Aharonian, F. et al. (2006a). "3.9 day orbital modulation in the TeV $\gamma$-ray flux and spectrum from the X-ray binary LS 5039". In: *Astronomy & Astrophysics* 460, pp. 743–749. DOI: 10.1051/0004-6361:20065940. eprint: astro-ph/0607192.

Aharonian, F. et al. (2006b). "Energy dependent $\gamma$-ray morphology in the pulsar wind nebula HESS J1825-137". In: *Astronomy & Astrophysics* 460, pp. 365–374. DOI: 10.1051/0004-6361:20065546. eprint: astro-ph/0607548.

Aharonian, F. A. et al. (2005b). "A possible association of the new VHE $\gamma$-ray source HESS J1825-137 with the pulsar wind nebula G18.0-0.7". In: *Astronomy & Astrophysics* 442, pp. L25–L29. DOI: 10.1051/0004-6361:200500180. eprint: astro-ph/0510394.

Antoni, T. et al. (2005). "KASCADE measurements of energy spectra for elemental groups of cosmic rays: Results and open problems". In: *Astroparticle Physics* 24, pp. 1–25. DOI: 10.1016/j.astropartphys.2005.04.001. eprint: astro-ph/0505413.

Archer, A. et al. (2018). "Measurement of cosmic-ray electrons at TeV energies by VERITAS". In: *Physical Review D* 98.6, 062004, p. 062004. DOI: 10.1103/PhysRevD.98.062004. arXiv: 1808.10028.

Arons, J. (2002). "Theory of Pulsar Winds". In: *Neutron Stars in Supernova Remnants*. Ed. by P. O. Slane and B. M. Gaensler. Vol. 271. Astronomical Society of the Pacific Conference Series, p. 71.

Arzoumanian, Z. et al. (2004). "A Central X-Ray Source in the Nonthermal Radio Nebula DA 495". In: *Astrophysical Journal, Letters* 610, pp. L101–L104. DOI: 10.1086/423338.

Arzoumanian, Z. et al. (2008). "Chandra Confirmation of a Pulsar Wind Nebula in DA 495". In: *Astrophysical Journal* 687, pp. 505–515. DOI: 10.1086/591654. arXiv: 0806.3766.

Atoyan, A. M. and F. A. Aharonian (1996). "On the fluxes of inverse Compton gamma-rays expected from the Crab Nebula." In: *Astronomy & Astrophysicss* 120, pp. 453–456.

Atwood, W. B. et al. (2007). "Design and initial tests of the Tracker-converter of the Gamma-ray Large Area Space Telescope". In: *Astroparticle Physics* 28, pp. 422–434. DOI: 10.1016/j.astropartphys.2007.08.010.

Atwood, W. B. et al. (2009). "The Large Area Telescope on the Fermi Gamma-Ray Space Telescope Mission". In: *Astrophysical Journal* 697, pp. 1071–1102. DOI: 10.1088/0004-637X/697/2/1071. arXiv: 0902.1089 [astro-ph.IM].

Baade, W. and F. Zwicky (1934). "Cosmic Rays from Super-novae". In: *Contributions from the Mount Wilson Observatory, vol. 3, pp.79-83* 3, pp. 79–83.

Bednarek, W., P. Banasiński, and J. Sitarek (2018). "Gamma-rays from the binary system containing PSR J2032+4127 during its periastron passage". In: *Journal of Physics G Nuclear Physics* 45.1, p. 015201. DOI: 10.1088/1361-6471/aa97ee. arXiv: 1711.01753.

Bednarek, W. and J. Sitarek (2013). "Gamma-rays from nebulae around binary systems containing energetic rotation-powered pulsars". In: *Monthly Notices of the Royal Astronomical Society* 430, pp. 2951–2959. DOI: 10.1093/mnras/stt098.

Bell, A. R. (1978). "The acceleration of cosmic rays in shock fronts. I". In: *Monthly Notices of the Royal Astronomical Society* 182, pp. 147–156. DOI: 10.1093/mnras/182.2.147.

— (2013). "Cosmic ray acceleration". In: *Astroparticle Physics* 43, pp. 56–70. DOI: 10.1016/j.astropartphys.2012.05.022.

Bühler, R. and M. Giomi (2016). "The imprint of pulsar parameters on the morphology of Pulsar Wind Nebulae". In: *Monthly Notices of the Royal Astronomical Society* 462, pp. 2762–2776. DOI: 10.1093/mnras/stw1773. arXiv: 1607.04277.

Camattari, R. (2016). "Laue lens for astrophysics: Extensive comparison between mosaic, curved, and quasi-mosaic crystals". In: *Astronomy & Astrophysics* 587, A21, A21. DOI: 10.1051/0004-6361/201526745.

Chen, A. M. et al. (2019). "Modelling the multi-wavelength emissions from PSR B1259-63/LS 2883: the effects of the stellar disc on shock radiations". In: *arXiv e-prints*. arXiv: 1904.07527.

Clark, J. S. et al. (2001). "On the radio emitting high mass X-ray binary <ASTROBJ>LS 5039</ASTROBJ>". In: *Astronomy & Astrophysics* 376, pp. 476–483. DOI: 10.1051/0004-6361:20010919.

Coerver, A. et al. (2019). "Multiwavelength Study of Pulsar Wind Nebula DA 495 with *NuSTAR*, *VERITAS* and *HAWC*". In: *accepted for publication in the Astrophysical Journal*.

CTA Consortium (2019). *Science with the Cherenkov Telescope Array*. World Scientific Publishing Co. DOI: 10.1142/10986.

Daniel, M. K. (2008). "The VERITAS standard data analysis". In: *International Cosmic Ray Conference* 3, pp. 1325–1328. arXiv: 0709.4006.

Dubus, G., B. Cerutti, and G. Henri (2010). "Relativistic Doppler-boosted emission in gamma-ray binaries". In: *Astronomy and Astrophysics* 516, A18, A18. DOI: 10.1051/0004-6361/201014023. arXiv: 1004.0511.

Fegan, D. J. (1997). "TOPICAL REVIEW: ?/hadron separation at TeV energies". In: *Journal of Physics G Nuclear Physics* 23, pp. 1013–1060. DOI: 10.1088/0954-3899/23/9/004.

Fermi, E. (1949). "On the Origin of the Cosmic Radiation". In: *Physical Review* 75, pp. 1169–1174. DOI: 10.1103/PhysRev.75.1169.

Filippenko, A. V. (1997). "Optical Spectra of Supernovae". In: *Annual Review of Astronomy and Astrophysics* 35, pp. 309–355. DOI: 10.1146/annurev.astro.35.1.309.

Finley, J. P., R. Srinivasan, and S. Park (1996). "The Morphology of Young Neutron Stars: PSR B1823-13, Its Compact Nebula, and Its Interstellar Neighborhood". In: *Astrophysical Journal* 466, p. 938. DOI: 10.1086/177564.

Fraschetti, F. and M. Pohl (2017). "Particle acceleration model for the broad-band baseline spectrum of the Crab nebula". In: *Monthly Notices of the Royal Astronomical Society* 471, pp. 4856–4864. DOI: 10.1093/mnras/stx1833. arXiv: 1702.00816.

Gaensler, B. M. and P. O. Slane (2006). "The Evolution and Structure of Pulsar Wind Nebulae". In: *Annual Review of Astronomy and Astrophysics* 44, pp. 17–47. DOI: 10.1146/annurev.astro.44.051905.092528. eprint: astro-ph/0601081.

Gaia Collaboration et al. (2018). "Gaia Data Release 2. Summary of the contents and survey properties". In: *Astronomy & Astrophysics* 616, A1, A1. DOI: 10.1051/0004-6361/201833051. arXiv: 1804.09365.

Galt, J. A. and J. E. D. Kennedy (1968). "Survey of radio sources observed in the continuum near 1420 MHz, declinations -5 to +70." In: *Astronomical Journal* 73, pp. 135–151. DOI: 10.1086/110609.

Goldreich, P. and W. H. Julian (1969). "Pulsar Electrodynamics". In: *Astrophysical Journal* 157, p. 869. DOI: 10.1086/150119.

Grasso, D. et al. (2009). "On possible interpretations of the high energy electron-positron spectrum measured by the Fermi Large Area Telescope". In: *Astroparticle Physics* 32, pp. 140–151. DOI: 10.1016/j.astropartphys.2009.07.003. arXiv: 0905.0636.

H. E. S. S. Collaboration et al. (2019). "Particle transport within the pulsar wind nebula HESS J1825-137". In: *Astronomy & Astrophysics* 621, A116, A116. DOI: 10.1051/0004-6361/201834335. arXiv: 1810.12676.

Hess, V. F. (1931). "Evidence for a Stellar Origin of the Cosmic Ultra-penetrating Radiation." In: *Nature* 127, pp. 10–11. DOI: 10.1038/127010b0.

H.E.S.S. Collaboration et al. (2018). "The population of TeV pulsar wind nebulae in the H.E.S.S. Galactic Plane Survey". In: *Astronomy & Astrophysics* 612, A2, A2. DOI: 10.1051/0004-6361/201629377. arXiv: 1702.08280.

Hessels, J. W. T. et al. (2006). "A Radio Pulsar Spinning at 716 Hz". In: *Science* 311, pp. 1901–1904. DOI: 10.1126/science.1123430. eprint: astro-ph/0601337.

Hester, J. J. (2008). "The Crab Nebula: An Astrophysical Chimera". In: *Annual Review of Astronomy and Astrophysics* 46, pp. 127–155. DOI: 10.1146/annurev.astro.45.051806.110608.

Hillas, A. M. (1985). "Cerenkov light images of EAS produced by primary gamma". In: *International Cosmic Ray Conference* 3.

— (1996). "Differences between Gamma-Ray and Hadronic Showers". In: *Space Science Reviews* 75, pp. 17–30. DOI: 10.1007/BF00195021.

— (2005). "TOPICAL REVIEW: Can diffusive shock acceleration in supernova remnants account for high-energy galactic cosmic rays?" In: *Journal of Physics G Nuclear Physics* 31, R95–R131. DOI: 10.1088/0954-3899/31/5/R02.

Ho, W. C. G., A. Y. Potekhin, and G. Chabrier (2008). "Model X-Ray Spectra of Magnetic Neutron Stars with Hydrogen Atmospheres". In: *Astrophysical Journal, Supplement* 178, pp. 102–109. DOI: 10.1086/589238. arXiv: 0802.2957.

Holder, J. (2015). "Atmospheric Cherenkov Gamma-ray Telescopes". In: *arXiv e-prints*. arXiv: 1510.05675 [astro-ph.IM].

— (2017). "Latest results from VERITAS: Gamma 2016". In: *6th International Symposium on High Energy Gamma-Ray Astronomy*. Vol. 1792. American Institute of Physics Conference Series, p. 020013. DOI: 10.1063/1.4968898. arXiv: 1609.02881.

Hubbell, J. H. (2006). "Electron positron pair production by photons: A historical overview". In: *Radiation Physics and Chemistry* 75, pp. 614–623. DOI: 10.1016/j.radphyschem.2005.10.008.

Johnston, S. and A. Karastergiou (2017). "Pulsar braking and the P-dot{P} diagram". In: *Monthly Notices of the Royal Astronomical Society* 467, pp. 3493–3499. DOI: 10.1093/mnras/stx377. arXiv: 1702.03616.

Kargaltsev, O. et al. (2015). "Pulsar-Wind Nebulae. Recent Progress in Observations and Theory". In: *Space Science Reviews* 191, pp. 391–439. DOI: 10.1007/s11214-015-0171-x. arXiv: 1507.03662.

Karpova, A. et al. (2015). "Constraining the parameters of the pulsar wind nebula DA 495 and its pulsar with Chandra and XMM-Newton". In: *Monthly Notices of the Royal Astronomical Society* 453, pp. 2241–2249. DOI: 10.1093/mnras/stv1765. arXiv: 1508.00002.

Kelner, S. R., F. A. Aharonian, and V. V. Bugayov (2006). "Energy spectra of gamma rays, electrons, and neutrinos produced at proton-proton interactions in the very high energy regime". In: *Physical Review D* 74.3, 034018, p. 034018. DOI: 10.1103/PhysRevD.74.034018. eprint: astro-ph/0606058.

Kennel, C. F. and F. V. Coroniti (1984). "Magnetohydrodynamic model of Crab nebula radiation". In: *Astrophysical Journal* 283, pp. 710–730. DOI: 10.1086/162357.

Kothes, R. et al. (2008). "DA 495: An Aging Pulsar Wind Nebula". In: *Astrophysical Journal* 687, pp. 516–531. DOI: 10.1086/591653. arXiv: 0807.0811.

Krause, M., E. Pueschel, and G. Maier (2017). "Improved $\gamma$/hadron separation for the detection of faint $\gamma$-ray sources using boosted decision trees". In: *Astroparticle Physics* 89, pp. 1–9. DOI: 10.1016/j.astropartphys.2017.01.004. arXiv: 1701.06928 [astro-ph.IM].

Landecker, T. L. and J. L. Caswell (1983). "DA 495 - an unusual supernova remnant with resemblances to the Crab nebula". In: *Astronomical Journal* 88, pp. 1810–1815. DOI: 10.1086/113472.

Lattimer, J. M. (2012). "The Nuclear Equation of State and Neutron Star Masses". In: *Annual Review of Nuclear and Particle Science* 62, pp. 485–515. DOI: 10.1146/annurev-nucl-102711-095018. arXiv: 1305.3510 [nucl-th].

Lattimer, J. M. and M. Prakash (2004). "The Physics of Neutron Stars". In: *Science* 304, pp. 536–542. DOI: 10.1126/science.1090720. eprint: astro-ph/0405262.

Li, T.-P. and Y.-Q. Ma (1983). "Analysis methods for results in gamma-ray astronomy". In: *Astrophysical Journal* 272, pp. 317–324. DOI: 10.1086/161295.

Longair, M. S. (2011). *High Energy Astrophysics*.

López-Coto, R. et al. (2018). "Effect of the diffusion parameters on the observed $\gamma$-ray spectrum of sources and their contribution to the local all-electron spectrum: The EDGE code". In: *Astroparticle Physics* 102, pp. 1–11. DOI: 10.1016/j.astropartphys.2018.04.003. arXiv: 1709.07653.

Lorimer, D. R. and M. Kramer (2012). *Handbook of Pulsar Astronomy*.

Lyne, A. G., R. S. Pritchard, and F. Graham-Smith (1993). "Twenty-Three Years of Crab Pulsar Rotational History". In: *Monthly Notices of the Royal Astronomical Society* 265, p. 1003. DOI: 10.1093/mnras/265.4.1003.

Manchester, R. N. et al. (2005). "The Australia Telescope National Facility Pulsar Catalogue". In: *Astronomical Journal* 129, pp. 1993–2006. DOI: 10.1086/428488. eprint: astro-ph/0412641.

Marti, J., J. M. Paredes, and M. Ribo (1998). "The system LS 5039: a new massive radio emitting X-ray binary". In: *Astronomy & Astrophysics* 338, pp. L71–L74.

Mattana, F. et al. (2009). "The Evolution of the $\gamma$- and X-Ray Luminosities of Pulsar Wind Nebulae". In: *Astrophysical Journal* 694, pp. 12–17. DOI: 10.1088/0004-637X/694/1/12. arXiv: 0811.0327.

Moiseev, A. A. et al. (2007). "The anti-coincidence detector for the GLAST large area telescope". In: *Astroparticle Physics* 27, pp. 339–358. DOI: 10.1016/j.astropartphys.2006.12.003. eprint: astro-ph/0702581.

Mori, K. and W. C. G. Ho (2007). "Modelling mid-Z element atmospheres for strongly magnetized neutron stars". In: *Monthly Notices of the Royal Astronomical Society* 377, pp. 905–919. DOI: 10.1111/j.1365-2966.2007.11663.x. eprint: astro-ph/0611145.

Motch, C. et al. (1997). "New massive X-ray binary candidates from the ROSAT Galactic Plane Survey. I. Results from a cross-correlation with OB star catalogues." In: *Astronomy & Astrophysics* 323, pp. 853–875. eprint: astro-ph/9611122.

Nicholl, M. et al. (2015). "On the diversity of superluminous supernovae: ejected mass as the dominant factor". In: *Monthly Notices of the Royal Astronomical Society* 452, pp. 3869–3893. DOI: 10.1093/mnras/stv1522. arXiv: 1503.03310 [astro-ph.SR].

Paredes, J. M. et al. (2000). "Discovery of a High-Energy Gamma-Ray-Emitting Persistent Microquasar". In: *Science* 288, pp. 2340–2342. DOI: 10.1126/science.288.5475.2340. eprint: astro-ph/0102235.

Park, N. and VERITAS Collaboration (2015). "Performance of the VERITAS experiment". In: *34th International Cosmic Ray Conference (ICRC2015)*. Vol. 34. International Cosmic Ray Conference, p. 771. arXiv: 1508.07070 [astro-ph.IM].

Pierre Auger Collaboration et al. (2017). "Observation of a large-scale anisotropy in the arrival directions of cosmic rays above $8 \times 10^{18}$ eV". In: *Science* 357, pp. 1266–1270. DOI: 10.1126/science.aan4338. arXiv: 1709.07321.

Reynolds, S. P. (2008). "Supernova Remnants at High Energy". In: *Annual Review of Astronomy and Astrophysics* 46, pp. 89–126. DOI: 10.1146/annurev.astro.46.060407.145237.

Seward, F. D. and Z.-R. Wang (1988). "Pulsars, X-ray synchrotron nebulae, and guest stars". In: *Astrophysical Journal* 332, pp. 199–205. DOI: 10.1086/166646.

Sinnis, G. (2009). "Air shower detectors in gamma-ray astronomy". In: *New Journal of Physics* 11.5, 055007, p. 055007. DOI: 10.1088/1367-2630/11/5/055007.

Smartt, S. J. (2015). "Observational Constraints on the Progenitors of Core-Collapse Supernovae: The Case for Missing High-Mass Stars". In: *Publications of the Astronomical Society of Australia* 32, e016, e016. DOI: 10.1017/pasa.2015.17. arXiv: 1504.02635 [astro-ph.SR].

Snowden, S. L., M. R. Collier, and K. D. Kuntz (2004). "XMM-Newton Observation of Solar Wind Charge Exchange Emission". In: *Astrophysical Journal* 610, pp. 1182–1190. DOI: 10.1086/421841. eprint: astro-ph/0404354.

Steiner, A. W., M. Hempel, and T. Fischer (2013). "Core-collapse Supernova Equations of State Based on Neutron Star Observations". In: *Astrophysical Journal* 774, 17, p. 17. DOI: 10.1088/0004-637X/774/1/17. arXiv: 1207.2184 [astro-ph.SR].

Sukhbold, T. et al. (2016). "Core-collapse Supernovae from 9 to 120 Solar Masses Based on Neutrino-powered Explosions". In: *Astrophysical Journal* 821, 38, p. 38. DOI: 10.3847/0004-637X/821/1/38. arXiv: 1510.04643.

Takata, J. et al. (2014). "High-energy Emissions from the Gamma-Ray Binary LS 5039". In: *Astrophysical Journal* 790, 18, p. 18. DOI: 10.1088/0004-637X/790/1/18. arXiv: 1406.6179.

Taylor, A. R. et al. (2003). "The Canadian Galactic Plane Survey". In: *Astronomical Journal* 125, pp. 3145–3164. DOI: 10.1086/375301.

The Fermi-LAT collaboration (2019). "Fermi Large Area Telescope Fourth Source Catalog". In: *arXiv e-prints*. arXiv: 1902.10045.

Torres, D. F. et al. (2014). "Time-dependent modeling of TeV-detected, young pulsar wind nebulae". In: *Journal of High Energy Astrophysics* 1, pp. 31–62. DOI: 10.1016/j.jheap.2014.02.001. arXiv: 1402.5485.

Čerenkov, P. A. (1937). "Visible Radiation Produced by Electrons Moving in a Medium with Velocities Exceeding that of Light". In: *Physical Review* 52, pp. 378–379. DOI: 10.1103/PhysRev.52.378.

Velusamy, T. et al. (1989). "Thick radio shell in supernova remnant DA 495 (G65.7+1.2)?" In: *Journal of Astrophysics and Astronomy* 10, pp. 161–172. DOI: 10.1007/BF02719313.

Voisin, F. et al. (2016). "ISM gas studies towards the TeV PWN HESS J1825-137 and northern region". In: *Monthly Notices of the Royal Astronomical Society* 458, pp. 2813–2835. DOI: 10.1093/mnras/stw473. arXiv: 1604.00090.

Wakely, S. P. and D. Horan (2008). "TeVCat: An online catalog for Very High Energy Gamma-Ray Astronomy". In: *International Cosmic Ray Conference* 3, pp. 1341–1344.

Weekes, T. C. et al. (1989). "Observation of TeV gamma rays from the Crab nebula using the atmospheric Cerenkov imaging technique". In: *Astrophysical Journal* 342, pp. 379–395. DOI: 10.1086/167599.

Weiler, K. W. and N. Panagia (1978). "Are Crab-type Supernova Remnants (Plerions) Short-lived?" In: *Astronomy & Astrophysics* 70, p. 419.

Wik, D. R. et al. (2014). "NuSTAR Observations of the Bullet Cluster: Constraints on Inverse Compton Emission". In: *Astrophysical Journal* 792, 48, p. 48. DOI: 10.1088/0004-637X/792/1/48. arXiv: 1403.2722.

Willis, A. G. (1973). "Observations of galactic supernova remnants at 1.7 and 2.7 GHz." In: *Astronomy & Astrophysics* 26, pp. 237–255.

Wilms, J., A. Allen, and R. McCray (2000). "On the Absorption of X-Rays in the Interstellar Medium". In: *Astrophysical Journal* 542, pp. 914–924. DOI: 10.1086/317016. eprint: astro-ph/0008425.

Woosley, S. E. and T. A. Weaver (1995). "The Evolution and Explosion of Massive Stars. II. Explosive Hydrodynamics and Nucleosynthesis". In: *Astrophysical Journal, Supplement* 101, p. 181. DOI: 10.1086/192237.

Yamaguchi, M. S., T. Yano, and N. Gouda (2018). "Uncovering the identities of compact objects in high-mass X-ray binaries and gamma-ray binaries by astrometric measurements". In: *Monthly Notices of the Royal Astronomical Society* 474, pp. 4756–4765. DOI: 10.1093/mnras/stx2993. arXiv: 1711.07488.

Yang, H. and R. A. Chevalier (2015). "Evolution of the Crab Nebula in a Low Energy Supernova". In: *Astrophysical Journal* 806, 153, p. 153. DOI: 10.1088/0004-637X/806/2/153. arXiv: 1505.03211.

Zirakashvili, V. N. and F. A. Aharonian (2010). "Nonthermal Radiation of Young Supernova Remnants: The Case of RX J1713.7-3946". In: *Astrophysical Journal* 708, pp. 965–980. DOI: 10.1088/0004-637X/708/2/965. arXiv: 0909.2285.